Carbonate rock dissolution during CO_2 and brine injection – An experimental study applying in-situ imaging by PET and CT

Department of Physics and Technology

A Master Thesis in Reservoir Physics

By Torunn Veien

UNIVERSITY OF BERGEN

March 2021

Abstract

Carbon Capture and Storage (CCS); capture of CO_2 from point sources followed by permanent storage in subsurface geological formations; can contribute to mitigating anthropogenic CO_2 emissions, and to the ongoing energy transition, by reducing climate impacts from petroleum production.

CO_2 that is injected into subsurface reservoirs will interact with the reservoir fluids; unavoidably dissolving in already present water (injected or formation). The result is acidic conditions in the reservoir, which can promote the dissolution of rock matrix. Dissolution may especially be an issue in reactive carbonate rocks. Carbonate reservoirs contain approximately 60% of the remaining hydrocarbon resources globally, and significant volumes of CO_2 may be stored in saline aquifers within carbonate formations. Understanding geochemical interactions that occur when CO_2 is injected into subsurface formations for storage is important: dissolution may, depending on location and pattern, benefit injectivity and/or threaten well integrity, cause geo-mechanical weakening, or create preferential flow paths within the reservoir which decreases the overall sweep efficiency. Dissolved matrix particles may flow within the reservoir and cause clogging of pores and throats, which may increase CO_2 storage security by reducing CO_2 migration or be detrimental to the rock flow and storage capacity. Investigation of dissolution on the core scale forms the basis for predictions of reactive transport and its effects on larger scales. The main objectives of this thesis were to 1) investigate dissolution of carbonate core samples during co-injection of supercritical CO_2 and brine, and 2) utilize emerging *in-situ* imaging techniques to quantify reactive fluid flow, dissolution patterns, and changes in local rock structure.

Co-injection was performed at reservoir conditions (40°C and 90bar), into five Edwards Yellow limestone core samples. The cores were fractured before co-injection, to localize the reactive fluid flow and promote dissolution and the formation of preferential pathways (wormholes) in and around the fracture. Two different fracture networks were utilized: a tight fracture network with a pre-existing longitudinal flow-channel along one side (A) and a closed fracture network with a tight longitudinal fracture (B). Global measurements of pressure and volumetric flow rates, and dynamic measurements of effluent pH were used to describe dynamic dissolution during co-injection of CO_2 and brine.

Computed Tomography (CT) imaging was used to gain insight into initial rock structure, and the dissolution pattern that had formed during co-injection. Micro-CT (µ-CT) provided high spatial resolutions (tens of µm scale) for detailed investigations of the fracture and matrix structure, while a preclinical CT module was used to characterize fracture and heterogeneities at mm-scale. CT combined with emerging imaging technique Positron Emission Tomography (PET) provided detailed insight into the relation between the evolving dissolution pattern (changes in pore structure) and local reactive flow regime.

Co-injection of CO_2 and brine into fractured carbonate core samples caused dissolution of the rock material in all five core samples. For fracture network (A) with a pre-existing high-conductivity channel, wormholes formed due to local dissolution within the conductive channel. Global measurements showed increased injectivity with time, but failed to predict the size and location of dissolution visualized by PET and CT. In tight fracture network (B) injectivity decreased during co-injection, estimated from global

measurements. Visual observations, however, showed significant dissolution at the injection side of the core samples. *In-situ* visualization revealed that reactive transport and dissolution also had occurred outside of the fracture area, indicating that the tight fracture network had been partially or fully blocked by particles, and fluids diverted into the pore network. *In-situ* imaging was necessary to determine changes in structure and flow during CO_2 injection, and revealed significant dissolution heterogeneities that could not be well captured with global measurements.

Acknowledgements

First of all, I would like to express my gratitude to my main supervisor Dr. Bergit Brattekås and co-supervisor Professor Martin Fernø at the Department of Physics and Technology at the University of Bergen, for giving me the opportunity to work on an interesting research project that is nowadays a very current topic. Thank you Bergit for excellent guidance, valuable discussions, motivation, and support.

A special thanks to PhD candidate Aleksandra Soyke, and Dr. Marianne Steinsbø for help and guidance in the lab. In addition, I would like to express my appreciation of PhD candidate Malin Haugen for willingly sharing knowledge about the topic, former master student Martine Folgerø Sandnes for lab guidance during aging and PhD candidate Benyamine Benali for technical support. Thanks to Heidi Espedal for help during PET-scanning and to Jan Magne Cederstrøm and Eivind Wilhelm Nagle Støren for helping with micro-CT imaging of my core samples.

I would also like to express my gratitude to my fellow students for contribution to five memorable years at the University of Bergen. Thank you for many interesting discussions, daily lunch breaks, social events, and memorable trips together. I wish you all the best in the future!

Finally, I would like to thank my family and friends for support and motivation.

Bergen, March 2021

Torunn Veien

Table of Content

Abstract i
Acknowledgements iii
Table of Content iv
Nomenclature vii
1 Fundamental principles 1
1.1 Porosity 1
1.2 Fluid saturation 1
1.3 Absolute and relative permeability 1
1.4 Interfacial tension, molecular diffusion, and dispersion 2
1.4.1 Capillary pressure, drainage, and imbibition 4
2 CCS; a key technology for handling climate change 6
2.1 Physical properties of CO_2 7
2.2 CO_2 storage 9
2.2.1 Trapping mechanisms in subsurface porous media for secure CO_2 storage 10
2.2.2 CO_2 storage in carbonate reservoirs 12
2.2.3 Geochemical interactions between CO_2, water, and carbonate rock 12
2.2.4 Dissolution patterns on the field scale by Damkohler and Peclet number 15
2.2.5 Dissolution patterns on the core scale 16
2.3 In-situ imaging techniques 18
2.3.1 Computed Tomography (CT) 18
2.3.2 Positron Emission Tomography (PET) 20
2.3.3 Voxel size and spatial resolution 21
2.4 Wormhole and fracture characterization obtained from global data and PET/CT 21
3 Methods and materials 24
3.1 Core material 24
3.2 Fluid properties 25
3.3 Core sample preparations 26
3.3.1 Saturation of core samples and porosity measurements 26
3.3.2 Absolute permeability measurements 27
3.3.3 Fracturing procedure 28
3.3.4 Micro-CT imaging 29
3.4 Dissolution during co-injection of CO_2 and brine 30

3.4.1 Core sample and system preparations before dissolution experiment 31
3.4.2 Co-injection of CO_2 and brine 32
3.4.3 Injection of traceable brine during PET/CT-imaging 33
4 Results and discussion 35
4.1 Basic core properties 35
4.2 Core quantification with micro-CT imaging 37
4.3 Characterization of fracture networks 39
4.4 Dynamic dissolution from global data 40
4.4.1 Dynamic dissolution in tight fractures with pre-existing wormhole 41
4.4.2 Dynamic dissolution in tight fractures 45
4.4.3 Apparent viscosity of co-injected brine and CO_2 during dissolution 48
4.4.4 Wormhole/fracture characterization from global measurements 49
4.4.5 Brine pH during dissolution 52
4.4.6 Important observations during dissolution 54
4.5 In-situ quantification of dissolution after co-injection 55
4.5.1 Visual characterization of dissolution patterns by micro-CT images 55
4.5.2 Quantification of dissolution by micro-CT images 57
4.5.3 Quantification of fracture aperture by micro-CT 62
4.5.4 Quantification of preferential flow paths by PET and CT images combined 63
4.5.5 Quantifying localization of reactive fluid saturation by preclinical PET images 72
4.5.6 Evaluation of best fitted imaging techniques and modalities for pore/fracture network and reactive fluid flow quantification at the core-scale 75
4.5.7 Important observations of dissolution found by application of in-situ imaging techniques 77
5 Conclusions and future work 79
5.1 Conclusions 79
5.2 Future work 80
Appendix 81
A Theory, experimental procedure, wettability measurements by Amott-Harvey wettability index, . and analysis of wettability alteration 81
A.1 Wettability 81
A.2 Fluid preparations 82
A.3 Wettability alteration by dynamic aging method 83
A.4 Wettability measurements by Amott-Harvey relative displacement Index 83

A.5 Wettability alteration results and analysis 85
B Filtration of produced effluents after dissolution and XRD-analysis of filtered particles 88
C Micro-CT images of homogenous Rørdal chalk core samples 91
D Setup for dissolution experiment by co-injection of CO_2 during high pressure PET-scan 92
E Plots from streamtube analysis 93
F Differential pressure of injection by FDG-brine during PET-scan 95
G Uncertainties 96
References 98

Nomenclature

Abbreviations:

2DS	2°C scenario
BPR	Back pressure regulator
C	Rørdal chalk
CCS	Carbon Capture and Storage
CCUS	Carbon Capture, Utilization and Storage
CS	Cross section
CT	Computed Tomography
D	Silurian dolomite
EOR	Enhanced oil recovery
FOV	Field of View
FW	Fractional wettability
GHG	Greenhouse gas
HC	Hydrocarbon
IEA	International Energy Agency
IFT	Interfacial tension
IPCC	Intergovernmental Panel on Climate Change
L	Edwards yellow limestone
LOR	Line of response
PET	Positron Emission Tomography
PV	Pore volume
ROI	Region of interest
RTS	Reference technology scenario
SNR	Signal to noise ratio
ST	Streamtube
WH	Wormhole

XRD	X-Ray diffraction

Terms:

$\emptyset_{abs}$	Absolute porosity
I_{AH}	Amott-Harvey wettability index
I_O	Wettability index of oil
I_W	Wettability index of water
K_{CL}	Fracture permeability from cubic law
K_i	Effective permeability of fluid i
K_{ri}	Relative permeability of fluid i
P_C	Capillary pressure
P_{nw}	Pressure of non-wetting phase
P_w	Pressure of wetting phase
$R_1 \; and \; R_2$	Principal radii of interfacial curvature
R_{WH}	Wormhole radius from Poiseuille's law
S_i	Saturation of respective fluid i
S_{or}	Residual oil saturation
S_{wi}	Irreducible water saturation
$T_{1/2}$	Half-life
V_b	Bulk volume
V_i	Volume of respective fluid i
$V_{o,forced}$	Volume of oil by forced displacement
$V_{o,sp}$	Volume of oil spontaneously displaced
$V_{o,tot}$	Total volume of oil displaced
V_p	Pore volume of interconnected pores
$V_{w,sp}$	Volume of water spontaneously displaced
$V_{w,forced}$	Volume of water by forced displacement
$V_{w,tot}$	Total volume of water displaced

e^+	Positron
m_{dry}	Mass of dry core sample
$m_{saturated}$	Mass of saturated core sample
v_e	Neutrino
μ_{app}	Apparent viscosity
μ_i	Viscosity of respective fluid
ρ_i	Density of respective fluid i
$\emptyset$	Effective porosity
A	Cross sectional area
D	Diameter/Diffusion coefficient/Fracture diameter
Da	Damkohler number
J	Diffusion flux
K	Absolute permeability
L	Length
Pe	Peclet number
Q	Volumetric flow rate
$Reactive\ fluid$	Carbonic acid
$Two-phase\ reactive\ transport\ (RT)$	Co-injection/Injection of CO_2 with brine
c	Concentration
dP	Differential pressure
e	Aperture
k	Reaction rate
l	Pore diameter
r	Core sample radius/pore radius/pore throat radius
u	Fluid velocity
x	Position
θ	Contact angle
σ	Interfacial tension

1 Fundamental principles

This chapter explains briefly fundamental principles that is important for understanding fluid flow in porous media. Fundamental principles like porosity, fluid saturation, permeability, interfacial tension, molecular diffusion, fluid dispersion and capillary pressure is described.

1.1 Porosity

Porosity is defined as a rock's fluid storage capacity, i.e., the void space of a rock's total volume, unoccupied by the rock's mineral grain and cement. *Effective porosity* (Ø) is the relation between the total pore volume of interconnected pores (V_p) and bulk volume (V_b) (Jenkins, 1966):

$$\emptyset = \frac{V_p}{V_b} \tag{1.1}$$

1.2 Fluid saturation

A porous medium is usually saturated with *n* fluids, and the pore volume typically contains water, oil or gas and can be written as:

$$V_p = \sum_i^n V_i \tag{1.2}$$

Saturation is the relative amount of oil, gas, or water in the porous medium. From equation 1.2, saturation (S_i) for phase i, is defined as the ratio between occupied pore volume by phase i (V_i) and total pore volume:

$$S_i = \frac{V_i}{V_p} \tag{1.3}$$

The relative saturation of each fluid in a multiphase system such as a hydrocarbon reservoir ranges between 0 and 1. The sum of the fluid saturations will always be equal to 1. Fluid saturation is a dynamic parameter that may change with time and location. During fluid injection in porous media, fluid saturation can be monitored by *material balance* where one immiscible fluid displaces another. Porous medium saturation can hence be found by monitoring the produced effluents versus time.

1.3 Absolute and relative permeability

Absolute permeability (K) is the fluid conductivity of a rock and describes the ability the rock has to transmit a single fluid through its network of interconnected pores. It is a constant property of a porous medium and defined by Darcy's law:

$$Q = \frac{K \cdot A}{\mu} \frac{dP}{dx} \tag{1.4}$$

Where A is the cross-section area of the porous medium, μ is the fluid viscosity and dP/dx is the differential pressure over a unit length. Darcy's law for measuring absolute permeability assumes; single phase flow, steady state flow, no rock-fluid interactions, incompressible fluid, and laminar fluid flow. Permeability is an intrinsic macroscopic property of the rock that results from a combination of several

parameters including the geometry of the pores and throats, and the connectivity of the voids (Mavko & Nur, 1997; Pape, Clauser, & Iffland, 1999).

Relative permeability is a dimensionless term that describes the flow of one phase in the presence of other immiscible phases. Relative permeability (K_{ri}) is the ratio of the effective permeability (K_i) of a particular phase i to absolute permeability (K):

$$K_{ri} = \frac{K_i}{K} \tag{1.5}$$

The presence of more than one phase inhibits the flow of each phase, which leaves the relative permeability of one phase to be less than 1. Relative permeability is often represented as a function of fluid saturation, usually water saturation. Overall, relative permeability of a phase increases with the saturation of the respective phase (figure 1.1).

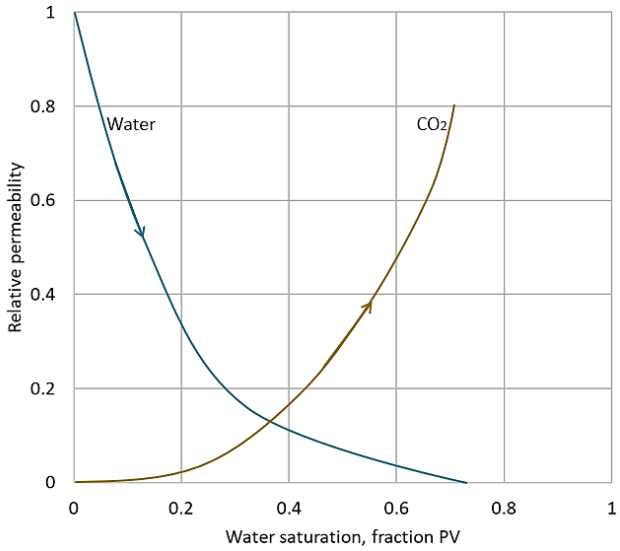

Figure 1.1 – Typical relative permeability curve of CO_2 and water during CO_2 injection into a porous medium that is initially fully saturated with water. Figure is modified from Jeong and Srinivasan (2017).

1.4 Interfacial tension, molecular diffusion, and dispersion

Interfacial tension (IFT) is the force of attraction between molecules at the interface of two fluids. IFT determines the mixing potential between two fluids. IFT in a CO_2-water-mineral system changes noticeability with fluid pressure, where IFT between CO_2 and water decreases significantly as pressure increases, which further causes mixing of the fluids by molecular diffusion. Molecular diffusion and dispersion are the main mechanisms responsible for mixing and spreading of fluids. *Molecular diffusion* is the tendency molecules have, to spontaneously move through a sharp interface due to the concentration differences between two phases. Diffusion is associated to a concentration gradient, where molecules move from high to low concentration due to random molecular motion (Brownian motions) until equilibrium between two phases occurs. At equilibrium, the sharp interface disappears and turns into a

diffuse mixing zone grading from one pure fluid to the other (Perkins & Johnston, 1963). Molecular diffusion is defined by *Fick's first law*:

$$J = -D\frac{dc}{dx} \tag{1.6}$$

Where J is the diffusion flux, D is the diffusion coefficient, c is the concentration, and x is the postion in the direction of the concentration gradient. Molecular diffusion depends on the concentration gradient, size of the molecule/particle, viscosity of the fluid, and temperature. Molecular diffusion *(microscopic dispersion)* happens when two or more phases forms a solution (e.g., carbonic acid) of a solute phase (e.g., CO_2) in a solvent (e.g., water), where the solute is the high concentration area that moves into the solvent which is the low concentration area (see figure 1.2). Solubility of the solute phase in the solvent is dependent on temperature, pressure, pH, selected solvent, adding of co-solvent, salt formation and micelle formation. Increased temperature increases the solubility of compound that is dissolved endothermically and decreases the solubility of compounds that are dissolved exothermally. Weak acids increase solubility with increasing pH, while weak bases increase solubility with decreasing pH. Adding surfactants may increase the solubility (Bear, 1988). Molecular diffusion can occur in gases, liquids, and more dense phases.

Dispersion (macroscopic diffusion) is facilitated by molecular diffusion and convection. Dispersion occurs due to a concentration gradient of introduced fluids throughout a porous medium. The concentration gradient drives the introduced fluid to move towards lower concentration areas, until the concentration is homogenously distributed. Concerning convection, variations in capillary pressure in a porous medium facilitate the distribution of the introduced fluid (Bear, 1988). Low capillary pressure areas are more easily occupied by dispersed fluid, than higher capillary pressure areas. Dispersion in a porous medium can be affected by variables such as heterogeneities of the medium and fluid viscosity (Perkins & Johnston, 1963). Dispersion can be differentiated from diffusion in that it is caused by non-ideal flow patterns and is a macroscopic phenomenon, whereas diffusion is caused by Brownian motions and is a microscopic phenomenon. Molecular diffusion and dispersion occur during injection of CO_2 and brine into a porous medium, where the fluids mix and spread into the available pore volume.

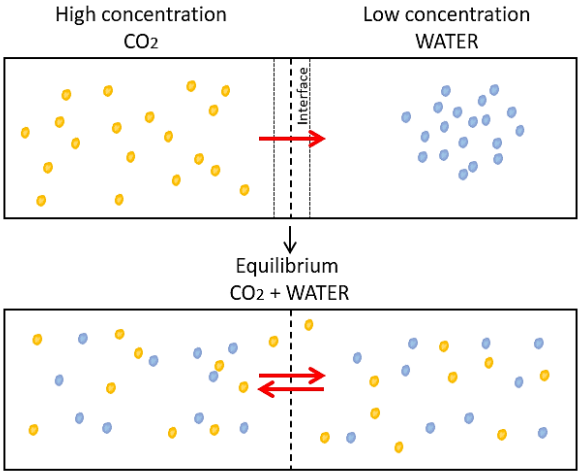

Figure 1.2 – Visualization of molecular diffusion and dispersion. Molecules move from high- to low-concentration areas through a sharp interface until equilibrium and mixing is achieved.

1.4.1 Capillary pressure, drainage, and imbibition

Capillary pressure (P_C) is the pressure between two immiscible fluids, which is a result from the interfacial tension between surfaces and immiscible fluids. Capillary pressure is defined as:

$$P_C = P_{nw} - P_w \tag{1.7}$$

Where, P_{nw} is the pressure in the non-wetting phase (e.g., CO_2) and P_w is the pressure in the wetting phase (e.g., water) (W. G. Anderson, 1987). Laplace combined a relation for capillary pressure of two immiscible fluids in a narrow cylindrical tube, with a curved interface in the form of meniscus between the two fluids as illustrated in figure 1.3. The pressure difference across the CO_2/water is given by Laplace's equation:

$$P_C = \sigma_{CO_2/water}\left(\frac{1}{R_1} + \frac{1}{R_2}\right) \tag{1.8}$$

Where R_1 and R_2 are the principal radii of the interface curvature and $\sigma_{CO_2/water}$ is the interfacial tension between CO_2 and fully CO_2 saturated water. Using standard trigonometric rules, if $R_1 = R_2 = R$, the expression for capillary pressure in a tube is:

$$P_C = \frac{2\sigma_{CO_2/water}\cdot\cos\theta_{CO_2/water}}{r} \tag{1.9}$$

Where $\theta_{CO_2/water}$ is the wetting angle and r is the radius of the capillary. The radius r can be compared to the radius of a pore throat, and equation 1.9 can be used to describe the capillary pressure of a bundle of tubes with varying pore throat radii, i.e., a simplified porous medium.

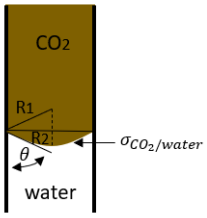

Figure 1.3 – Illustration of CO_2/water interface in capillary tube where water is the wetting phase and CO_2 is the non-wetting phase.

Capillary pressure can provide both an opposing or driving force for fluid transport and displacement of other fluids. Processes where capillary pressure is crucial, is drainage and imbibition. *Drainage* is when a wetting fluid will be displaced by a non-wetting fluid (e.g., injection of CO_2 in a fully water saturated and water wet (contact angle=0-90°) porous medium), and *imbibition* is where the wetting fluid returns and displaces the non-wetting fluid. In a drainage process the CO_2 will first enter pores or areas with the lowest capillary pressure (i.e., largest pores) and CO_2 will then successively invade smaller pores, and the capillary pressure increases. During drainage, some residual water will be left in the pore volume when CO_2 is at maximum saturation. For imbibition it is vice versa, some of the CO_2 becomes residual in the pore volume as the water imbibe into the smallest pores and displace CO_2 until P_C=0. The effect of drainage and imbibition by causing different immobile saturations is called *hysteresis*. It is referred to path dependence of capillary pressure and relative permeability of the saturation history and path. When CO_2 is injected into a reservoir containing water, the saturation of CO_2 increases in a drainage process (figure 1.1). When

injected and after injection is stopped, CO_2 migrates lateral and vertical, due to buoyancy forces and diffusion, where CO_2 displaces water. In the leading edge of the porous media CO_2 migrates and displaces water, but in the trailing edge the water displaces CO_2 in an imbibition process. Hysteresis during CO_2 injection causes a fraction of immobile CO_2 saturation. Immobile saturations of CO_2 are beneficial for trapping CO_2 in porous media, which is more thoroughly explained in section 2.2.1 below.

2 CCS; a key technology for handling climate change

The Intergovernmental Panel on Climate Change (IPCC) states in their Synthesis Report on Climate Change (IPCC, 2015) that recent anthropogenic greenhouse gas (GHG) emissions is higher than ever and that the human influence on the climate system is clear. The concentration of CO_2 in the atmosphere has increased noticeably since the pre-industrial era, largely driven by economy and population growth. CO_2 is emitted during human activities, e.g., by burning fossil fuels, producing cement, producing clothes, making food, indoor heating, and production of technology. The effect of man-made emissions of carbon dioxide, methane and nitrous oxide have been identified throughout the climate system as the cause of observed global warming since the mid-20th century. CO_2 emitted into the atmosphere delays heat radiation and causes a temperature rise on earth. The global average of combined land and ocean surface temperature shows a warming of 0.85°C during the period from 1880 - 2012. A warming of the atmosphere and ocean gives a negative impact on the climate and environment, by causing more extreme weather and a rise in the sea-level due to melting of glaciers and poles (IPCC, 2015). Anthropogenic CO_2 emissions have increased in the last 40 years. From 1970 - 2010, 78% of total GHG emissions is CO_2 emission from industrial processes and fossil fuel combustion (IPCC, 2015). Forecasts of CO_2 emission propose that the increase is and will continue to be exponential under the current energy-use pattern. Figure 2.1 shows the link between global temperature, atmospheric CO_2-concentration, and population. All of which have increased sharply during the last decades.

Figure 2.1 – Link between atmospheric CO_2 concentration, global surface temperature and human population (Onozaki, 2009).

If CO_2 emissions continue to increase, further warming and changes of components of the climate system, will advance in some cases irreversibly changes in ecosystems and impact people in a negative way. Reduction of GHG emissions will limit further global warming and reduce the risk of climate change (IPCC, 2015). Carbon Capture and Storage (CCS) is an important strategy to reduce GHG emissions and is necessary to achieve the climate goals set forward in the Paris Agreement, article 2. The agreement says that the global temperature must not rise more than 2°C before this century is over, to limit climate change (United Nations, 2015). CCS consists of three steps, where the first step is to capture CO_2 from energy-related and industrial sources. Second, transport of CO_2 to a storage location and third, a permanent storage isolating the CO_2 away from the atmosphere (Metz et al., 2013). Figure 2.2, illustrated

by IEA (2017) shows that CCS is an important CO_2 reduction technology, needed to reduce CO_2 emissions. IEA (2017) estimates that CCS will reduce CO_2 emissions by 14% within the next 40 years.

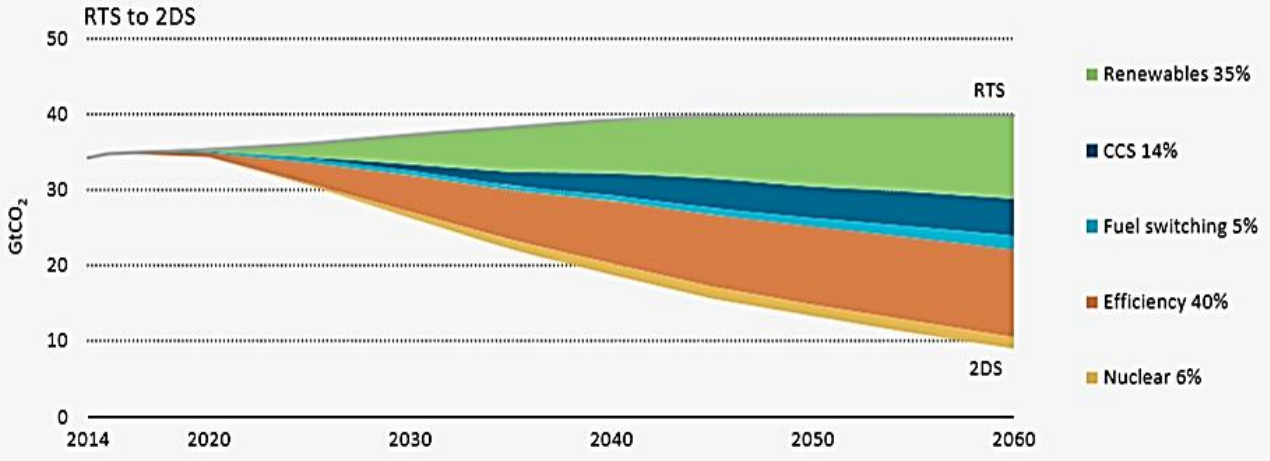

Figure 2.2 – Reduction of CO_2 emissions by technology area on a global scale from Reference Technology Scenario (RTS) to 2°C scenario (2DS), figure obtained from IEA (2017).

This thesis will focus on the third step of the CCS value chain, i.e., injection and subsurface storage of CO_2. Geological formations suitable for CO_2 storage include depleted oil and gas fields, saline aquifers, and unmineable coal beds with a combined worldwide storage capacity of 2000GtCO_2 (Metz et al., 2013).

Storage of CO_2 in deep saline aquifer is proven to be viable, by the Sleipner project in the North Sea. Since 1996, an approximate average daily injection rate has been 3000tCO_2 per day, ca. 1MtCO_2 per year. A total planned storage of its lifetime is 20MtCO_2 (Benson S., 2013). Most CCS projects worldwide include sandstone rock formations (Sleipner: sandstone saline aquifer). Porous rock holding oil, gas or brine has a great potential to store CO_2 and carbonate hydrocarbon (HC) reservoirs is estimated to cover 60% of global conventional and unconventional HC resources that are suitable for CO_2 sequestration (Burchette, 2012), in addition, suitable for CO_2 EOR (Enhanced Oil Recovery) as CCUS (Carbon Capture Utilization and Storage). Carbonate rock formations holds a great amount of CO_2 storage potential and is therefore needed to be understood before injection of CO_2, due to its very heterogenous pore structure and its highly reactive nature.

2.1 Physical properties of CO_2

In this thesis injection of CO_2 with brine is performed at in-situ conditions (high pressure and temperature). It is important to understand how CO_2 behaves as a function of temperature and pressure both for practical reasons during experiments and for understanding CO_2 storage in subsurface geological formations. CO_2 is the molecular formula of carbon dioxide, a chemical compound of two elements: carbon and oxygen. As shown in figure 2.3, a phase diagram of carbon dioxide, the physical state of CO_2 varies with pressure and temperature. The behavior of CO_2 at subsurface storage conditions differs from ambient conditions. In ambient conditions at 1 bar and 20°C, CO_2 is a gaseous phase. At temperatures higher than 31.1°C and pressure above 73.9 bars (beyond critical point) the CO_2 is a supercritical phase

with viscosity as a gas, and density like a liquid (see figure 2.4 for variations of density and viscosity as a function of pressure and temperature). For subsurface CO_2 storage, temperature and pressure regimes are such that CO_2 is of supercritical phase and sometimes liquid (Stefan Bachu, 2013).

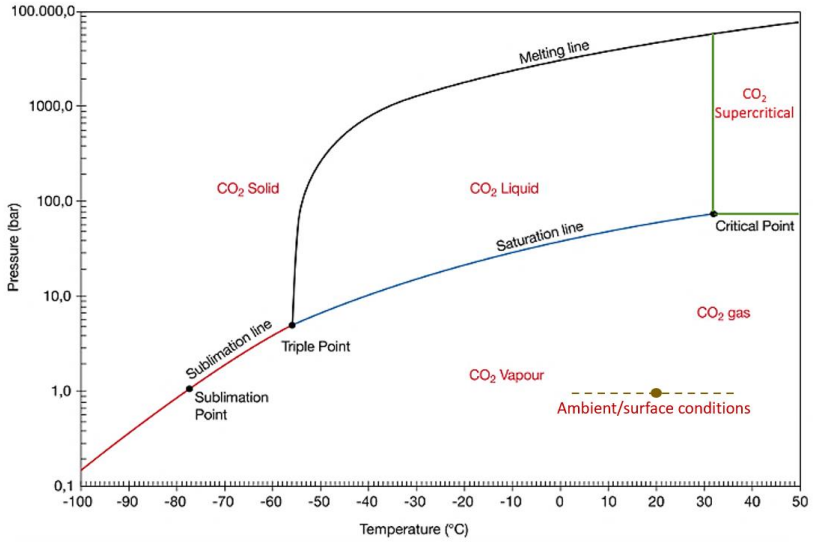

Figure 2.3 – Phase diagram for CO_2. Figure modified from Stefan Bachu (2013).

Pressure conditions influence CO_2 density (figure 2.4). CO_2 density when injected subsurface increases rapidly from a subsurface depth of approximately 800m (critical depth) and further. The volume of CO_2 decreases drastically with depth in a subsurface rock formation due to an increase in overburden pressure. From a depth at 1.5km and below, the volume and density are more or less constant (Wilson, Mordensky, Verba, & Colwell, 2016). The change in density and volume of CO_2 with depth (i.e., pressure and temperature increase) is positive for the subsurface storage potential, allowing storage of a greater volume of CO_2. CO_2 storage in hydrocarbon reservoirs or deep saline formations is generally expected to take place at depth below 800m.

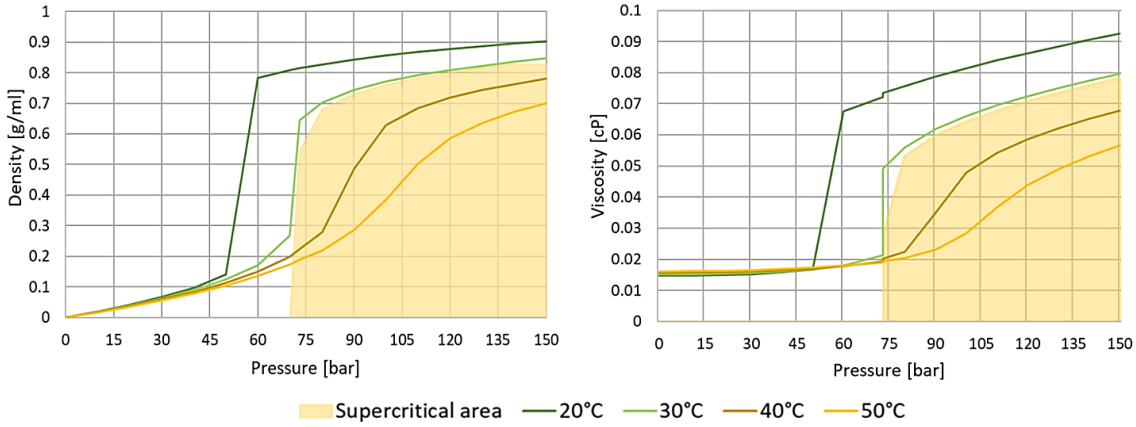

Figure 2.4 – Variations of density and viscosity for CO_2 as a function of pressure and temperature. The supercritical area of CO_2 is represented as the yellow shade in the plots. Data point's obtained from Lemmon, McLinden, and Friend (2020).

2.2 CO_2 storage

Subsurface geological formations must include the following characteristics to be suitable for CO_2 storage:

1. Storage capacity; room for the anticipated volumes of CO_2.
2. Injectivity; capacity to take the amount of CO_2 at a rate that is delivered from the CO_2 emitters. i.e., sufficient permeability.
3. Confinement (e.g., a cap rock); for a secure CO_2 sequestration by preventing leakage and migration of the mobile CO_2 from the storage formations and up to the surface or into other formations, shallow groundwater, or the ocean.

Different types of geological formations that can be used for CO_2 sequestration is illustrated in figure 2.5. These options can be split into two economic parts, (a) CO_2 injection purely for storage and (b) CO_2 injection for enhanced oil recovery (EOR) or coal-bed methane production (Baines & Worden, 2004). For each case illustrated, CO_2 storage can be accomplished by injecting CO_2 as a compressed fluid into the geological formation.

Depleted or existing oil and gas reservoirs are of practical reasons the most considered options for CO_2 storage. The geological understanding of depleted oil and gas reservoirs is greater than for example saline aquifers and there is potential for using the already existing infrastructure and technology (recycling) (Baines & Worden, 2004). CO_2 injection in existing oil and gas reservoirs can be used for both storage and EOR purposes, where CO_2 injection into oil reservoirs can expand the reservoir lifetime by improving the rate of recovery. In gas reservoirs, CO_2 can be used as pressure support. Estimated storage capacity in oil and gas fields are from 675-900$GtCO_2$ (Benson S., 2013). The number will increase by 25% if "undiscovered" oil and gas fields are included. In hydrocarbon reservoirs there is always a cap rock (impermeable rock above the reservoir that traps hydrocarbons) present that have shown a good storage and sealing capacity over geological time.

Deep saline formations has the biggest storage potential, from 1000 - $10^4$$GtCO_2$ (Benson S., 2013) and injection of CO_2 involves many of the same technologies that have been developed in the oil and gas industry. CO_2 sequestration in saline aquifers is however less economically viable in most of the world.

Unmineable coal beds has an economic interest because it has a big amount of methane-rich gas that is absorbed onto the surface of the coal. Depressurization by pumping water out of the reservoir allows the gas to be extracted. Around twice as much CO_2 can be adsorbed on coal than methane. Therefore does CO_2 have the potential to displace methane and remain stored in the coal bed (Reeves, 2003). Estimated storage capacity in unmineable coal beds are much lower than for saline aquifers and oil and gas reservoirs. It ranges from 3-200 $GtCO_2$ (Benson S., 2013).

In this thesis injection of CO_2 was investigated in porous media with conditions that mimic depleted or existing oil and gas reservoirs and deep saline aquifers. In porous media with in-situ conditions will cause an increasingly immobilization of CO_2 by different trapping mechanisms. To secure a long and safe sequestration of CO_2 in porous media it is important that the storage site include the three points mentioned above, including geological stability, and effective trapping mechanisms such as physical and geochemical trapping (Stefan Bachu, 2008).

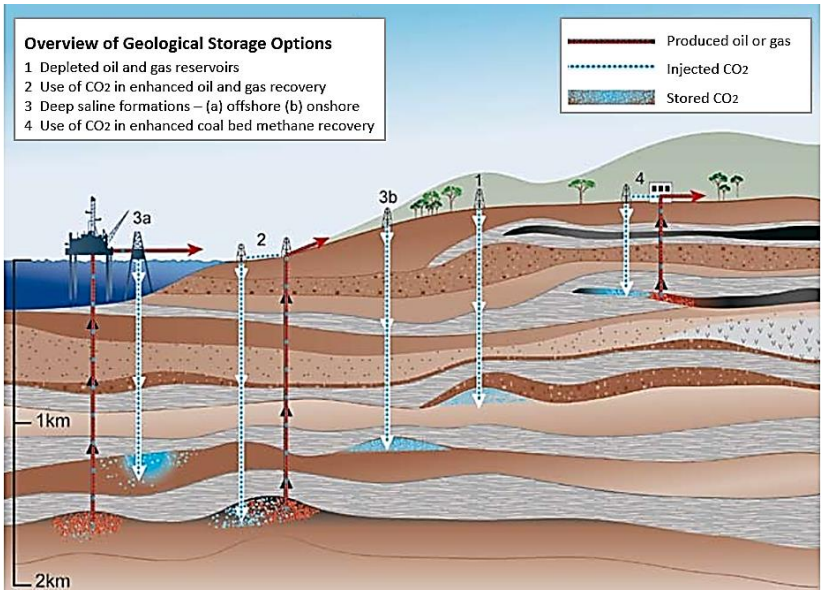

Figure 2.5 - Different types of reservoir and geological formations that can be used for CO_2 storage. Figure modified from (CO2CRC, 2020).

2.2.1 Trapping mechanisms in subsurface porous media for secure CO_2 storage

The third criteria of CO_2 site selection is confinement. Deep saline formations or HC reservoirs will often have temperature and pressure regimes where CO_2 exist in liquid or supercritical state. Supercritical CO_2 density is 50–80% of the density of water, close to several crude oils, and therefore buoyancy forces will drive the CO_2 upwards. A non-permeable caprock (defined as fluid flow capacity < 10^{-3}mD) is essential for keeping the CO_2 trapped in saline formations or HC reservoirs. Other leakage pathways for example through poorly plugged abandoned wells, faults etc. is a risk. However, a combination of geochemical and physical trapping mechanism are in place for securing a safe long-term storage of CO_2 in porous media (Stefan Bachu et al., 2007). Physical trapping is divided into three different mechanisms: static (structural and stratigraphic), residual gas trapping and hydrodynamic trapping. Geochemical trapping consists of solubility and mineral trapping (Steel, Mackay, & Maroto-Valer, 2018). The trapping mechanisms increase the CO_2 storage security with time as demonstrated in figure 2.6.

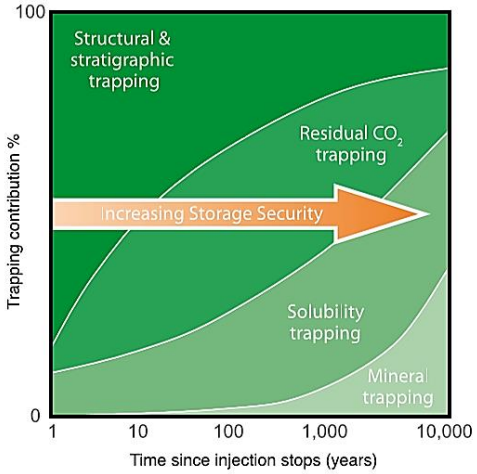

Figure 2.6 – Different CO_2 storage mechanisms in geological formations, where the contribution of each trapping mechanism is plotted as a function of time since CO_2 injection stopped (Metz et al., 2013).

Static trapping of CO_2 occurs where a stratigraphic or structural trap (e.g., cap rock) is non-permeable and has a shape that prevents the lateral and upwards flow of CO_2. Stratigraphic traps is a result of diagenetic and/or depositional processes, while structural traps (folds and faults) are a result of movement in the crust (Stefan Bachu, 2008). *Residual gas trapping* occurs when CO_2 is immobilized by the interfacial tension (capillary forces) between CO_2 and formation water. The residual trapping happens at irreducible gas saturation and a migration of CO_2 is no longer possible. Injection of CO_2 into a porous medium will increase CO_2 saturation by a drainage process during and after injection, CO_2 migrates lateral and vertical (due to buoyancy forces) where it continues to displace the wetting phase. In the trailing edge the wetting phase, however, displaces CO_2 in an imbibition process. Trapping of residual CO_2 continues to happen after injection has stopped (Stefan Bachu, 2008), where residual CO_2 is present as disconnected bubbles as displayed in figure 2.7.

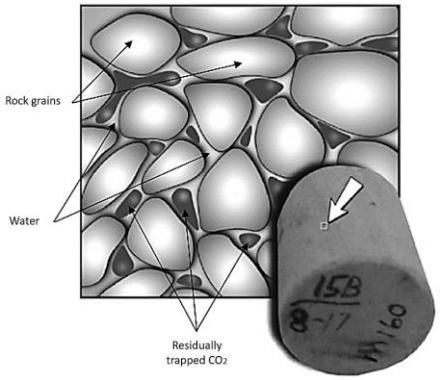

Figure 2.7 – Illustration of residual gas trapping. Disconnected snap-offs of non-wetting CO_2 in a water-wet porous medium. Figure modified from Stefan Bachu (2008).

Hydrodynamic trapping occurs when injected CO_2 migrates in a slow pase laterally and/or upwards due to buoancy forces. A migration up to the surface would take some time on a geological scale (tens of thousands to million of years) and under favourable conditions the CO_2 will be trapped as residual CO_2 saturation or in local structural and startigraphic traps before it reaches the surface. Potentially, a large mass of CO_2 can be stored in this way. (Stefan Bachu et al., 2007; S. Bachu, Gunter, & Perkins, 1994; Metz et al., 2013).

Geochemical trapping mechanisms is when CO_2, after injection, does not exist as a free phase because it will either dissolve in the formation fluids or precipitate as a carbonate mineral (Benson S., 2013). *Solubility trapping* happens when CO_2 dissolves in the in-situ fluids in a porous medium. The amount of CO_2 that dissolves in water, is dependent on several factors like salinity of water, temperature, and pressure. CO_2 dissolved in water makes the water denser and hence heavier. The CO_2 saturated water will therefore sink in the formation and prevent further migration by buoyancy (Benson S., 2013). *Mineral trapping* is the safest trapping mechanism for long term CO_2 storage and is due to a chemical reaction between CO_2 saturated water and minerals of the formation rock, where precipitation of minerals over time due to ionic species occurs (Benson S., 2013). Mineral precipitation is expected to be very slow because it depends on dissolution of silicate minerals. Mineral trapping could take up to tens to hundreds of years (Benson & Cole, 2008). Carbonate reservoir are especially sensitive towards a chemical reaction caused by CO_2 saturated water, since carbonates mainly consist of calcite minerals which is a highly reactive mineral.

2.2.2 CO_2 storage in carbonate reservoirs

Carbonate reservoirs are estimated to contain 60% of total conventional and unconventional HC resources globally (Burchette, 2012), and may be considered as potential CO_2 storage sites. Carbonate reservoirs is of heterogeneous origin and are therefore hard to exploit. Heterogenic properties are a result from complex diagenetic, reactive, depositional, and deformational processes. Heterogenic properties like vugs, and natural/induced fractures are an important aspect in carbonate rocks (Moore & Wade, 2013). Fractures is a macroscopic discontinuity in a reservoir, where orientation, density and aperture are the main features. Natural fracture networks can occur as secondary porosity in carbonate reservoirs on a multiscale. Fractures contributes to complex flow paths and increases communications within different reservoir zones with high permeability (Toublanc et al., 2005). High permeability zones sometimes lead to channeling of CO_2 injection, meaning that the area where CO_2 interacts with the carbonate reservoir is decreased (Luhmann et al., 2014). At a given porosity in carbonate reservoirs, permeability may range over three to four orders of magnitude. Pore systems in the reservoir has varied shape and are complex. The pore-size distribution can range from micro porosity to vugs (pores larger than 1/16 mm in diameter). The pore systems often contain dual permeability, e.g., connected vugs. Fractures, connected vugs, and pore systems with a matrix that has dual porosity and permeability will result in a discrimination of permeability distribution. Resulting in significant uncertainties in predicting CO_2 plume distribution and HC recovery in carbonate reservoir (Burchette, 2012). The large variations in fracture network connectivity and the matrix, with physical and chemical properties that influences the wettability of the carbonate rock, making the reservoir sensitive towards fluid properties, are the main reason for a complex flow behavior (Agada, Geiger, & Doster, 2016; Burchette, 2012).

Carbonate reservoirs have a distinctive stratigraphic construction that controls the distribution of all the heterogenic properties mentioned above. Diagenesis plays a vital role in the development of the pore system in carbonate reservoirs (Moore & Wade, 2013). Diagenesis is a change of physical, chemical, and biological properties, which sediments are exposed to after it has been deposited. Primary porosity in carbonate reservoirs is formed at the end of the depositional process, whereas secondary porosity develops after deposition. Secondary porosity develops due to a chemical reaction that occurs during diagenetic processes such as precipitation and dissolution of carbonate minerals (W. I. Anderson, 1998; Moore & Wade, 2013).

2.2.3 Geochemical interactions between CO_2, water, and carbonate rock

During CO_2 injection in a subsurface carbonate reservoir, CO_2 will react with formation water and promote dissolution of the rock. This section describes how CO_2 and water reacts, and the consequence on carbonate reservoirs.

CO_2 dissolved in formation water involves several chemical reactions which are represented as:

$$CO_2(g) + H_2O\ (aq) \leftrightarrow H_2CO_3(aq)\ \leftrightarrow HCO_3^-(aq) + H^+(aq)\ \leftrightarrow CO_3^{2-}(aq) + 2H^+(aq) \qquad (2.1)$$

Here, gaseous CO_2 reacts with water (H_2O) and forms carbonic acid (H_2CO_3). Carbonic acid separates and forms bicarbonate ions (HCO_3^-), which can further separate and form carbonate ions (CO_3^{2-}). The

release of H^+ ions due to the chemical reaction between carbon dioxide and water, lowers the pH in the carbonic acid, which makes it a week acid with a pH normally between 3-5. The pH in the carbonic acid is around 3 at typical storage conditions (Snippe, Berg, Ganga, Brussee, & Gdanski, 2020). The pH of the carbonic acid decreases at conditions where CO_2 is more soluble in water. Solubility of CO_2 in water depends on water salinity, pressure, and temperature. From figure 2.8 one can see that more CO_2 dissolves when the pressure is high, and temperatures are low. In this thesis supercritical CO_2 (40°C and 90bars) was used (marked as yellow dotted line in figure 2.8).

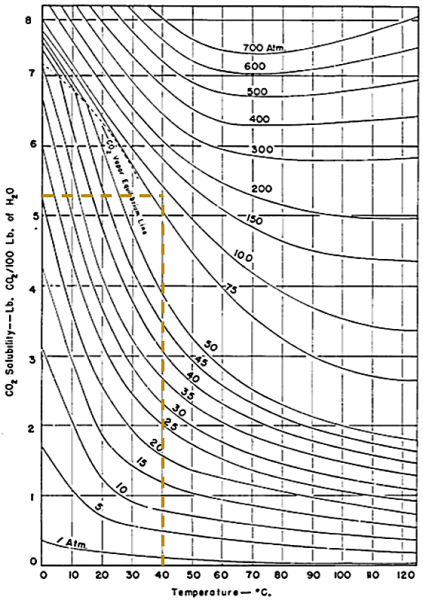

Figure 2.8 – CO_2 solubility in water as a function temperature and pressure (Dodds, Stutzman, & Sollami, 1956).

Calcium carbonate ($CaCO_3$), also called calcite is the main component in carbonate rocks and is a highly reactive mineral. Calcite is soluble in water and reacts with carbonic acid. The chemical equation for the reaction between calcium carbonate and carbonic acid is:

$$CaCO_3(s) + CO_2(g) + H_2O(l) \leftrightarrow Ca^{2+}(aq) + 2HCO_3^-(aq) \leftrightarrow CaCO_3 + H_2CO_3 \qquad (2.2)$$

When CO_2 is injected in a carbonate rock it will first dissolve in the formation water, and further cause dissolution and precipitation of calcite. Dissolution of calcite increase with increasing acidity (decreasing pH) of the formation water (Snippe et al., 2020). Where dissolution of calcite occurs, CO_2 is also produced, which further will increase the concentration of carbon dioxide in the solution. Calcite will buffer a decrease in pH near a chemical equilibrium, where calcite mixed in carbonic acid will promote an increase in pH in two ways: first, protons are consumed and will neutralize the carbonic acid. Second, it provides cations that can react with the dissolved CO_2, to form stable carbonate minerals (Snæbjörnsdóttir et al., 2020). Dissolution of calcite will happen if the chemical equilibrium is not present. Steel et al. (2018) studied the pH buffer effect when interactions between CO_2-saturated brine and calcite was present under reservoir conditions. Three experiments were conducted over a period of one, three and six months to assess the potential for calcite to buffer CO_2-saturated brine and promote mineral carbonation. The system in the study had yet to reach an equilibrium at six months. Addition of calcite to the brine resulted in a significant increase in brine pH. The disslution of calcite leaded to a production of HCO_3^-, and

the pH did not increase above 6. At pH <6, carbonic acid dominates (Stumm & Morgan, 1995). The study concluded that the buffer effect of calcite was not big enough to promote mineral carbonation, and that the dissolution continues.

The main reasons for a continuous dissolution when a reaction between CO_2-brine-carbonate rock is present, are, the anisotropic and crystallographic structures by the minerals, and transport of fluids along interfaces in the rock. In addition, what decides if the carbonate rock either changes its permeability/transport type drastically or contain the sealing capability is, structural heterogeneities, texture, composition, and crystal morphology. (Noiriel & Daval, 2017). Dissolution of calcite in carbonate rocks can cause changes in flow regimes and geometry which affects fluid velocity, permeability, diffusivity, and mass transport. Interfaces can be displaced, pore roughness, porosity and tortuosity can change, and clogging may occur. Dissolved particles can clog local pores, fractures, and areas of the pore network, leaving a reduction in local porosity and sometimes bulk permeability, which is not beneficial for the CO_2 storage potential and injectivity. Clogging will reduce storage potential and require a greater injection pressure to displace CO_2 into the carbonate reservoir (Czernichowski-Lauriol et al., 2006). However, clogging may affect the storage security positively by limiting the extent of CO_2 migration due to a reduced flow capacity. Nevertheless, dissolution in patterns along the flow direction have the tendency to increase the injectivity and permeability if the dissolved pattern extends over the whole unit length of the porous medium. Dissolution leading to a creation of a high permeability pathway are referred to as wormholes. Wormholes typically reduces the reactive surface area in a carbonate rock, since a discrimination of reactive fluid flow occurs, and therefore causes a porosity increase mainly in wormhole area. An increase in porosity caused by dissolution is dependent on little to no clogging, and that calcite particles is produced (Luhmann et al., 2014). A wormhole can cause geomechanically weakening of a carbonate reservoir due substantial local dissolution (porosity increase). The weakening depends on the extend and magnitude of dissolution through the reservoir. Several studies (Luhmann et al., 2014; Luquot & Gouze, 2009; Megan M. Smith, Sholokhova, Hao, & Carroll, 2013; Wang, Bernabé, Mok, & Evans, 2016) have previously shown that wormholes at breakthrough causes a permeability increase. Luhmann et al. (2014) injected CO_2-saturated brine into nine dolomite core samples at different flow rates. Experiments resulted in significant increase in measured bulk permeability. The rate of permeability increased as a function of porosity increase with time for experiments at high flow rates (≥ 6ml/h). Low flow rates (< 6ml/h), yielded a lower rate of permeability increase. In the early stages of experiments dissolution only occurred near inlet of the core samples, producing a relatively small increase in bulk permeability per increase in porosity. As wormholes developed, dissolution propagated further towards the outlet side of the core sample, resulting in a more substantial increase in permeability per increase in porosity. Note that the former studies where performed with whole carbonate core samples. Yang et al. (2020) examined porosity and permeability evolution (by applying X-ray computed tomography) in fractured limestone core sample during injection of CO_2 saturated brine. The discrimination of reactive fluid flow within the fracture caused a porosity increase in fracture area, whereas the surrounding area showed little change in porosity. The porosity increase was lower, where the initial porosity was low, and higher where initial porosity was high. The larger the initial porosity was, the easier a dissolution occurred. So, in fractured carbonate core sample, dissolution is not simply concentrated to the area at inlet but related to initial heterogeneities. However, dissolution occurred

mainly near the inlet side of the core sample. The permeability evolution in that study showed that an increase in permeability at early stages of the dissolution happened more rapid compared to later stages of dissolution. There are less geochemical interactions between CO_2 saturated brine and carbonate rock after a preferential flow channel (i.e., the fracture) is formed, which was shown as lower power law exponent compared to dissolution in whole core sample (Al-Khulaifi, Lin, Blunt, & Bijeljic, 2017; Luquot & Gouze, 2009; Menke, Bijeljic, Andrew, & Blunt, 2015; M. M. Smith, Hao, & Carroll, 2017). The distribution and shape of dissolution patterns, such as wormholes, compact dissolution, channeling, and other patterns caused by CO_2-brine-carbonate rock interactions is mainly controlled by initial heterogeneity of the pore structure and the initial permeability field.

2.2.4 Dissolution patterns on the field scale by Damkohler and Peclet number

On the field scale, shape of wormholes, channeling and other dissolution patterns can be described by the Damkohler and Peclet number. Due to CO_2-water-carbonate rock interactions, dissolution occurs and the geometry of the rock changes. Snippe et al. (2020) consider three different calcite dissolution systems in carbonate reservoirs: one is a compact cylindrical shaped cavity around the injection well; the second is a uniform dissolution throughout the injected water plume; and the third is wormholes or channeling, where the structure is long branched channels with a small diameter. Since carbonate rocks are of a highly heterogeneous character (from pore-scale to large-scale), uniform and homogenous dissolution will presumably not happen. Dissolution patterns are a function of key control parameters which can be described by Peclet and Damkohler number. Damkohler (Da) and Peclet (Pe) are dimensionless numbers, defined as (Golfier et al., 2002):

$$Da = \frac{kl}{u} = \frac{Reaction\ rate}{convection\ rate} \tag{2.3}$$

$$Pe = \frac{ul}{D} = \frac{convection\ rate}{diffusion\ rate} \tag{2.4}$$

where k is overall reaction rate, l is typical length scale, u is the interstitial velocity and D is the molecular diffusion coefficient. For well stimulation operations, Peclet and Damkohler numbers can be used to design and control the dissolution patterns for reaching a preferred injectivity gain within operational and economic limits, where Peclet and Damkohler primarily can be regulated by flow rate. Damkohler and Peclet numbers shows that CO_2 concentration, temperature, and core properties influence the reaction rate and diffusion rate, whereas fluid flow velocities influence the convection rate. At low convection rate (Da = intermediate to high, Pe = low) compact dissolution and conical wormholes forms. At intermediate to high rates (Da = intermediate to high, Pe = intermediate to high) dominant and ramified wormholes forms. Uniform dissolution takes place when Damkohler number is low. Figure 2.9 demonstrates the different dissolution propagations at near wellbore that are influenced by the injection regime.

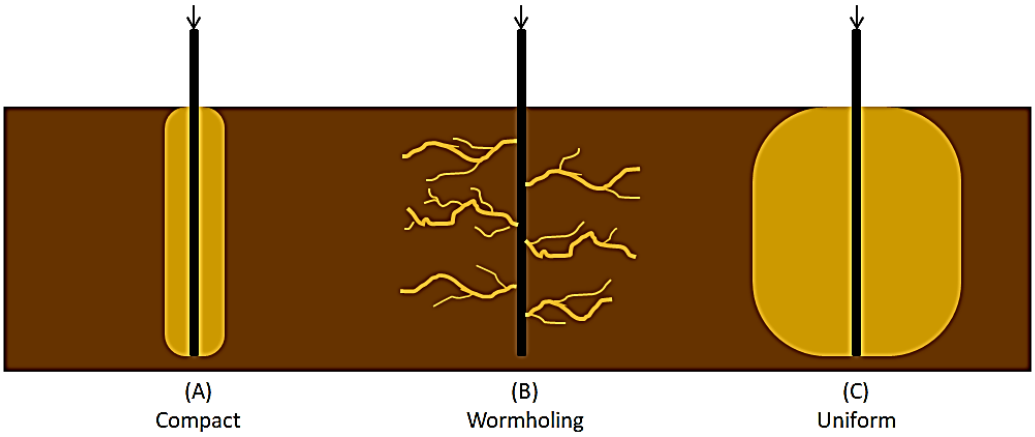

Figure 2.9 – Three idealized examples of how calcite dissolution could occur near wellbore, depending on the injection regime. Dissolution can occur as (A) compact dissolution, (B) wormholing, and (C) uniform dissolution. The figure is made with inspiration from Snippe et al. (2020).

Regarding CCS, the dissolution propagations at the injection side can influence the performance of an injection well; it can cause an unstable well bore. In addition, it can promote a change in migration pathways that either has a positively or negatively effect on storage security, it can both promote and prevent leakage of CO_2 to the surface. Dissolution and forming of wormholes represent a risk regarding estimates of mechanical and hydraulic properties of the rock but have the best benefits for injectivity. Whereas a compact dissolution shape is a threat against well integrity. The growth and dynamic behavior of the dissolution systems must be understood in a proper way, so one can account for both positive and negative effects.

2.2.5 Dissolution patterns on the core scale

Luquot and Gouze (2009) performed a set of four flow-through experiments using CO_2-saturated brine under in-situ conditions in limestone core samples. A constant rate was used during injection of CO_2-saturated brine at various partial pressure of CO_2. Experiments performed with a partial pressure of CO_2 (p_{CO_2}) close to the total system pressure (p_{tot}) revealed the formation of highly conductive channels and wormholes, that is associated with a transport-controlled dissolution, i.e., higher reaction kinetics (Sjöberg & Rickard, 1984). At low partial pressure of CO_2, uniform dissolution was obtained. In this thesis fraction of CO_2 during co-injection with brine was decided based on the result from Luquot and Gouze (2009) and for mimicking mass transfers near the injection well, where the fraction of CO_2 corresponds to a partial pressure close to the total in-situ pressure used. The fraction of CO_2 can be measured as concentration (C_{CO_2}) and the partial pressure of CO_2 is determined by using *Dalton's law*:

$$p_{CO_2} = p_{tot} \cdot C_{CO_2} \tag{2.5}$$

In this thesis a two-phase co-injection of high fraction CO_2 and brine was performed. Co-injection with high fraction of CO_2 includes the presence of a separate CO_2 phase in addition to CO_2 saturated brine (carbonic acid). Several studies have evaluated dissolution patterns during single-phase and two-phase reactive transport (RT) of CO_2 and brine into whole carbonate core samples. Single-phase RT involves injection of brine that is pre-saturated with CO_2 (CO_2 saturated brine), whilst two-phase RT is co-injection.

A two-phase RT may impact dissolution regimes as suggested by (Luhmann et al., 2014; Ott & Oedai, 2015; Snippe et al., 2020; Snippe, Gdanski, & Ott, 2017); Figure 2.10 shows a model of dissolution regime in single-phase RT, and co-injection of CO_2 with brine (two-phase RT) at similar pressure, temperature, and flow rate conditions. In a two-phase RT, a non-wetting CO_2 phase tends to occupy the volume with lowest capillary pressure, i.e., in wormholes initially formed by carbonic acid (seeds). A CO_2 phase present in the wormhole could suppress further growth of wormhole seeds because the CO_2 phase is nonreactive, which further leads to a compact dissolution. Whilst, in a single-phase RT the wormhole initially formed by carbonic acid, will discriminate fluid flow to happen in the wormhole and cause further growth, which is related to permeability.

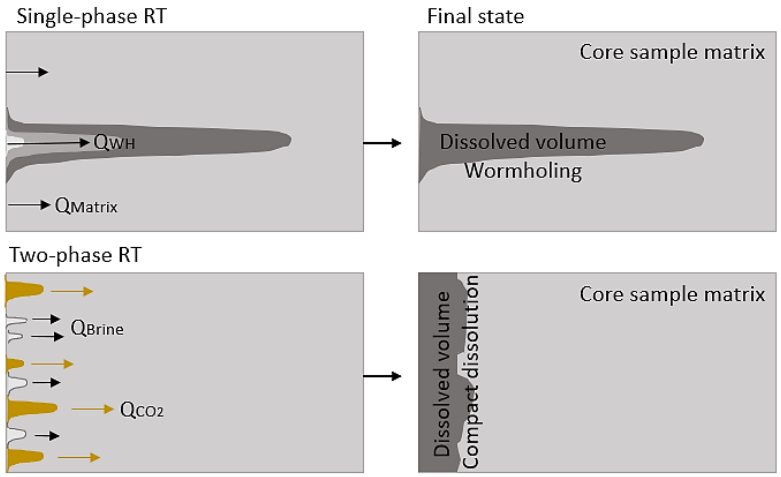

Figure 2.10 – Simplified model of dissolution regimes in single-phase RT (CO_2 saturated brine), and two-phase RT (co-injection of CO_2 and brine). Figure was modified from Ott and Oedai (2015).

The former studies have performed single phase and two-phase flow experiments on whole carbonate core samples for examine wormholing with and without the presence of a CO_2 phase. The dissolution patterns formed by the reactive fluid flow regimes were examined by using X-ray computed tomography. The pressure and temperature regimes where fixed at in-situ conditions, and several injection rates were performed during single- and two-phase RT. Ott and Oedai (2015) particularly studied single- and two-phase RT at an injection rate at 60ml/h in brine saturated limestone core sample, with temperature of 50°C and pressure of 100bars. The single-phase RT showed that initially, several seeds formed and grew to a certain length until they started to compete. With time, a single wormhole (WH) dominated the dissolution pattern and started forming branches. Whilst at a two-phase RT under the same conditions, resulted in compact dissolution. Luhmann et al. (2014) studied single-phase RT at different injection rates, where the injection rate of 60ml/h (characterized as high flow rate) resulted in branched wormhole, whilst rates close to 0.6ml/h (characterized as low flow rate) gave compact dissolution at inlet side. Flow rates close to 6ml/h (characterized as intermediate flow rate) produced thin WH channels. Snippe et al. (2020) studied both single- and two-phase RT, with several injection rates. Single-phase RT at Injection rate of 66ml/h produced branched wormhole, whereas two-phase RT at the same flow rate produced compact dissolution at inlet side. Simulations based on experimental data from this study was also performed, where dissolution at injection rate from ~20-30ml/h for single-phase RT showed dominant wormholes, whereas for a two-phase RT showed compact dissolution. For rates above approximately 70ml/h showed

a branching transitioning to homogenous for single-phase RT, and for two-phase RT small seeds and wormholes started to form. The studies from (Ott & Oedai, 2015; Snippe et al., 2020) showed that a dissolution regime by two-phase RT at in-situ conditions with injection rates in the higher region (> ∼20ml/h) changed from primarily wormholes to a cone shape and compact dissolution structure at inlet side. However, for flow rates higher than 70ml/h wormholes started to form during two-phase RT. Based on the former studies, two-phase RT with injection rates in the higher region were used in this thesis and performed on fractured carbonate core samples.

In fractured carbonate core samples dissolution is expected to occur within the fracture. A fracture is expected to have a lower capillary pressure than the surrounding pore space, which results in a discrimination of reactive fluid flow. Initial heterogeneities in the fracture aperture causes the reactive fluid flow to happen in already established and preferred flow channels. Development of wormhole within the already established flow channel occurs due to a further discrimination of reactive fluid flow, making the aperture of the established flow channel to grow. Yang et al. (2020) performed CO_2 saturated brine injection with a flow rate of 6ml/h into fractured limestone core sample. The system pressure and temperature were 100bars and 50°C, respectively. The study showed that dissolution occurred mainly at the fracture walls, resulting in fracture aperture growth. The inner wall of the fracture was also smoothed. Particles were observed to flow towards outlet, which further proved that a flow channel of the carbonic acid occurred in the fracture. The overall structure of the pore space outside of the fracture remained unchanged, due to the discrimination of reactive fluid flow within fracture. No specific dissolution pattern was found in the former study, however the original fracture aperture increased.

2.3 In-situ imaging techniques

Dissolution of carbonate rock material was qualitatively described by global measurements and quantified using in-situ imaging techniques in this thesis. Two different imaging techniques were used and are presented in this section: Computed Tomography (CT) and Positron Emission Tomography (PET). PET/CT-images used to capture reactive fluid flow (carbonic acid flow) in fractured carbonate rock material is for the first time obtained in this thesis. CT-imaging was performed for comparison and quantifications of the pore structure before and after dissolution. Different PET and CT modalities (micro-CT, preclinical PET/CT, and clinical PET/CT) was used to evaluate imaging technology for quantification of pore/fracture structure and flow regimes, caused by co-injection of CO_2 and brine in fractured limestone core samples.

2.3.1 Computed Tomography (CT)

CT-images can enable fracture, heterogeneities, dissolution patterns, pores, and vugs within a core sample. Therefore, are CT-images suited for quantification of pore size distribution, determination of heterogeneities and hence high permeability areas where reactive fluid flow would cause most dissolution, and estimation of dimensions and volume of dissolved area. In addition, with CT-images, segmentation of pores and fracture network is possible to obtain.

CT-imaging is originally developed for clinical use, but it is also commonly used by geoscientists (Mees, Swennen, Geet, & Jacobs, 2003). CT produces a time-averaged density distribution image of a medium (e.g. core sample) by measuring the damping of x-rays through a gradual loss of flux intensity through the scanned medium (Heindel, 2011). CT-scan is an X-ray procedure that creates cross sectional images with the help of computer processing. A CT-scanner uses a motorized X-ray source that project narrow beams of X-rays towards the porous medium. The X-ray source could be fixed where the porous medium is attached to a rotation device (micro-CT scanner used in this thesis), or the X-ray source rotates around the porous medium (preclinical and clinical CT scanner used in this thesis), dependent on the type of CT-scanner. A digital X-ray detector is located directly on the opposite side of the X-ray source, and as the X-ray passes through the porous medium, X-ray attenuation is picked up by the detectors and transmitted to a computer which further reconstructs image slices. Image slices can be displayed either individually in 2D or stacked together to 3D.

The interactions that are responsible for the attenuation of X-rays are mainly Compton scattering and photoelectric absorption where the CT-number will vary with the energy of the rays. At high energies, Compton scattering dominates and attenuation is mainly determined by density, at low energies attenuation is dominated by photoelectric absorption (Mees et al., 2003). The CT-number is a normalized value of calculated X-ray absorption coefficient of a pixel (2D element) in a CT. In other words, it is the density assigned to a voxel (3D element) on an arbitrary scale (Hounsfield unit (HU) on which air has a density of -1000, water 0, and compact matrix, 1000. For micro-CT, 8-bit images are used. An 8-bit image has minimum pixel value (CT-number) of 0 to a maximum at 255, where 0 represents pores, and 255 represents matrix/grains. On a grayscale, the 0 will be represented as black and 255 as white, with different tones of grey for values in between. In figure 2.11 an axial cross section of an 8-bit image is shown. Dark grey/black areas represent low densities where X-rays experience insignificant attenuation, whereas a lighter grey/white area represent high densities where X-rays experience a significant attenuation.

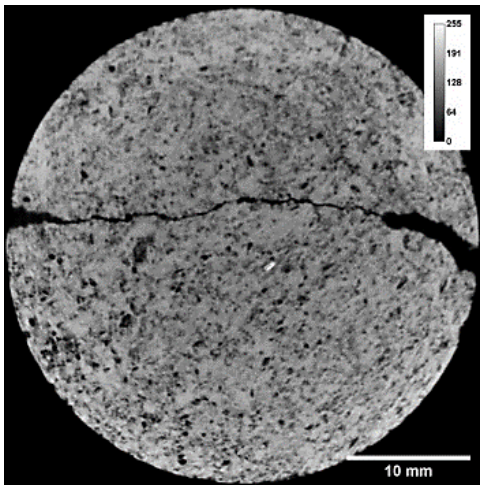

Figure 2.11 – A cross section with axial view of micro-CT scanned cylindrical core sample with 8-bit grayscale.

2.3.2 Positron Emission Tomography (PET)

PET provides information about the spatial variation and anisotropy of transport regimes and is therefore a suitable instrument for the validation of wormhole development. PET-images can quantify the localization of dynamic reactive fluid flow, and hence reveal where dissolution occurs in a core sample. In addition, heterogeneities and dissolution patterns can be enabled. PET qualitatively and quantitatively yields the spatiotemporal distribution of a tracer concentration. PET uses a positron-emitting isotope as radiotracer. The tracer is injected into a porous medium during PET-scan. When the radioactive tracer loses its radioactivity (decays) and slows down as it travel through the core sample it loses its energy, which result in emitting a subatomic particle called a positron (e^+). It also emits neutrino (ν_e). When the positron hits a surrounding electron in the core sample, it results in a complete annihilation of both particles. The energy (511keV) from the annihilation event release two photons that speed of in opposite directions (figure 2.12; ideal event). The detectors in the PET-scanner measures the count of events on a line of response (LOR) and gets mapped to a corresponding position in a sinogram. By detecting thousands of annihilation events every second and performing some computer processing, the tracer distribution in a core sample is visualized as 3D. The number of coincidences and frame length determines the quality of the images. With time the PET-signal decreases and the noise increases, which gives a poorer quality of the images. Low-activity values from PET-scan are more affected by background noise, than higher-activity values. (Johannes Kulenkampff, Gründig, Zakhnini, & Lippmann-Pipke, 2016; Zahasky & Benson, 2018). Background noise can be detected scatter events (photons from annihilation event) outside line of response or random counts caused by a false LOR during PET-scan. False LOR is caused by two separate annihilation events. Scatter event and random counts is illustrated in figure 2.12.

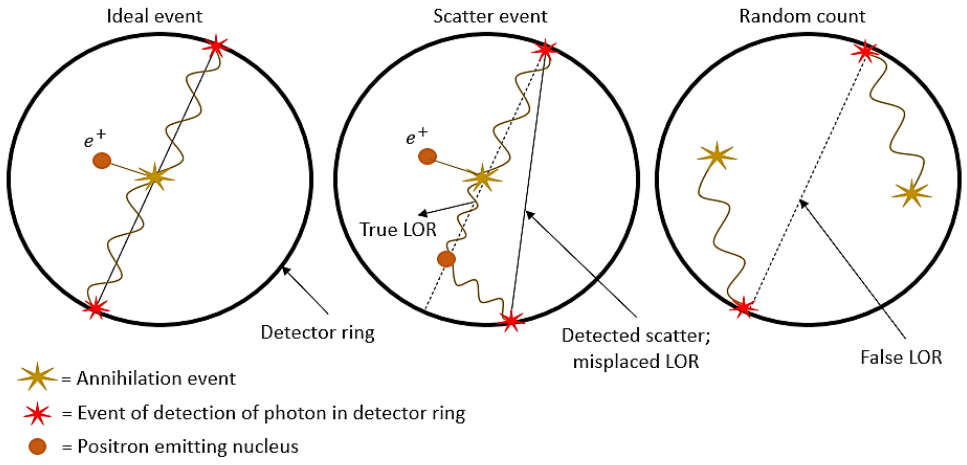

Figure 2.12 – Ideal, scatter and random detection of events. Two simultaneous (within 6.12ns time difference) events in the detector make a line of response (LOR). False LOR by random counts is caused by two separate annihilation events.

The tracer used in this thesis was ^{18}F produced by a cyclotron to ^{18}F-FDG (^{18}F-fluorodeoxyglucose). The tracer is a water-soluble fluorine radioisotope with half-life of $T_{1/2}$ = 109.77min, and is mixed with the injection fluid (i.e., brine). ^{18}F has earlier been used in studies where PET-scans was used to quantify water flow paths within polymer gel-filled fractures (Bergit Brattekås et al., 2017), in addition, for quantifying fractures (J. Kulenkampff, Gründig, Richter, & Enzmann, 2008; Johannes Kulenkampff et al., 2016) and fluid flow in porous media. Equation 2.10 shows the decay reaction of ^{18}F:

$$^{18}_{9}F \rightarrow \ ^{18}_{8}O + e^{+} + v_e + energy \tag{2.6}$$

Johannes Kulenkampff et al. (2016) used PET-scans to quantitatively derive the anisotropic diffusion coefficient and finding information of heterogenic properties of core samples, based on observed diffusion patterns of PET-signals. At high activity values from a PET-image, local structures may occur as a PET-signal. A deviation from simple anisotropic propagation of a PET-signal in a porous medium is an indication of structural heterogeneities, causing different diffusion pathways. In this thesis were dynamic PET-scans performed to quantify heterogeneities, preferable flow paths of reactive fluid flow and hence dissolution affected area. A dynamic PET-scan is where a static image is reconstructed from the dynamic scan at respective injection rates. In the static image the injected fluid flow is revealed as PET-signal.

2.3.3 Voxel size and spatial resolution

Voxel size and spatial resolution is an important factor in PET/CT images. A higher spatial resolution gives more precise information from a PET/CT-image. The voxel size is dependent on different imaging techniques and modalities. Different modalities have different voxel size regimes, which from high to low spatial resolution by; micro-CT, preclinical PET/CT and clinical PET/CT. A preclinical PET/CT-scanner has a smaller field of view (FOV) compared to a clinical PET/CT-scanner and therefore, low voxel size, and hence a higher spatial resolution (Cherry & Chatziioannou, 2004). A voxel is the smallest 3D element of a volume and is commonly characterized as a cube. Each voxel for CT represents a specific X-ray absorption. Voxel size is usually determined by FOV. A small FOV (e.g., core sample used in this thesis) may use a small voxel size, which enables visualization of small differences in pore structure. The smaller the voxel size the better resolution on the image. The voxel size is dependent of the imaging objective and the size of the detector. It is important to mention that pores and other structures smaller than the voxel size in a PET/CT-scanned core sample will not be enabled on the reconstructed images. Voxel size (i.e., spatial resolution) is mainly determined by; FOV, scan time (only for CT), number of basis images and type of detector. If the acquisition time is long during a CT-scan, the more basis images are produced. If a small voxel size is chosen, it will result in high spatial resolution and low signal to noise ratio (SNR). SNR is the ratio between true signal (i.e., reflecting actual scanned medium) and background noise, and preferred to be low.

2.4 Wormhole and fracture characterization obtained from global data and PET/CT

In this thesis wormhole and fracture characteristics is estimated from global measurements and quantified using sophisticated imaging techniques. Wormhole radius was calculated from global data such as differential pressure, volumetric flow rate and fluid viscosity, using *Poiseuille's law*. Applying Poiseuille's law to quantify wormholes has earlier been performed in several studies (Bergit Brattekås et al., 2017; Golfier et al., 2002; Wang et al., 2016). To describe wormhole using global data; Poiseuille's law assumes a pressure drop in an incompressible and Newtonian fluid in laminar flow through a cylindrical conduit with a constant cross section. The law describes the pressure drop due to viscosity of the fluid. Poiseuille's law is defined as:

$$R_{WH} = \left(\frac{Q \cdot \mu}{dP}\right)^{0.25} \tag{2.7}$$

where R_{WH} is the estimated wormhole radius, Q is the volumetric flow rate, μ is fluid viscosity and dP is the differential pressure. *Fluid viscosity* is a measure of a fluids resistance to flow and describes the internal friction of a flowing fluid. Viscosity was calculated by adapting Darcy's law, where permeability is a constant representing the complexity of the pore space alone. Due to heterogeneity of the internal flow velocities inside the pore space, shear rates vary inside the porous media. So, an *apparent viscosity* (μ_{app}) is introduced in Darcy's law, to account for non-linear effects, and can be found as:

$$\mu_{app} = \frac{K \cdot dP \cdot A}{L \cdot Q} \tag{2.8}$$

PET-images were used to visualize flow of radioactive water through wormholes, whereas CT-images were a supplement to PET, in addition used for rock quantification. PET/CT had the purpose to see if global measurements was sufficient to quantify wormhole and fracture characteristics. By using CT average fracture aperture was found in this work. Fractures can be characterized as tight, partially open, and open by its average aperture. A partially open and open fracture have a higher permeability than a tight fracture which results in more discrimination of fluid flow. In addition to characterizing the fracture network by CT-images, the hydraulic fracture aperture (e) was estimated from Buckingham's using the following equation:

$$e = \sqrt[3]{\frac{12 \cdot \mu \cdot Q \cdot L}{D \cdot dP}} \tag{2.9}$$

Where D is the fracture width equal to the core sample diameter. Hydraulic aperture can further be used to quantify fracture/wormhole permeability. Estimated fracture/wormhole permeability can be found by using aperture directly in the *cubic law*, which is an approximation and defined as:

$$K_{CL} = \frac{e^2}{12} \tag{2.10}$$

Where K_{CL} is the absolute fracture permeability and e is the hydraulic fracture aperture. The cubic law, and the equation from Buckingham's is approximated by using Poiseuille's law of the Navier-Stokes equation, and assumes laminar flow between two smooth, parallel plates, separated by a distance (aperture) (Snow, 1969; Witherspoon, Wang, Iwai, & Gale, 1980) (figure 2.13). Hydraulic aperture and fracture permeability in fractured core samples has former been studied by using the same method as described above (Bergit Brattekås et al., 2020; Chaojie, Sina, Harald, & Philipp, 2020). Several apertures can be found, as perpendicular aperture, segment aperture and vertical aperture (Konzuk & Kueper, 2004). In this thesis only vertical aperture was studied.

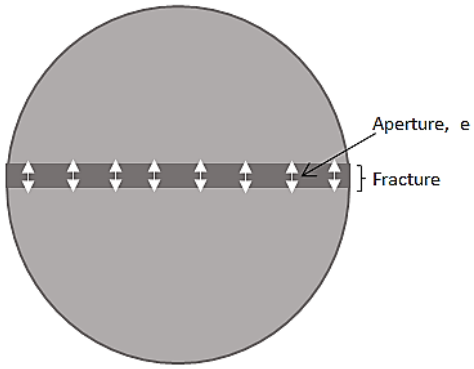

Figure 2.13 – Axial view of an idealized fractured cylindrical core sample, where the white arrows represent vertical aperture.

3 Methods and materials

This chapter presents the experimental procedure, and setups used to perform experimental work for this thesis. The main objective of this thesis was to investigate dissolution and dissolution patterns that forms in carbonate core samples during co-injection of CO_2 and brine (two-phase RT). In addition, to investigate reactive fluid flow. Dissolution patterns and fluid flow was examined by comparing global measurements to in-situ visualization. To visualize the pore network and structures, CT-scans were conducted, whereas investigation of fluid flow was examined by PET-scans. Baseline and dissolution experiments were conducted at the Department of Physics and Technology, University of Bergen, in Bergen, Norway. Preclinical and clinical CT/PET-scans were performed at Centre for Nuclear Medicine and PET, Department of Radiology, Haukeland University Hospital, also in Bergen. Micro-CT-scans before and after dissolution were performed at Earthlab, Department of Geosciences, University of Bergen.

3.1 Core material

Different outcrop carbonate core samples collected from Texas (USA) and Ålborg (Denmark) were evaluated in this thesis. Ten limestone core samples (denoted as L#) from West-Texas (Edwards Yellow), two dolomite core samples (denoted as D#) from the Silurian period, also collected from Texas and three chalk core samples (denoted as C#) from the Rørdal quarry at the cement factory in Ålborg. The core samples were cylindrical with a diameter close to 3.8 cm and length ranging from 6.1-7.6cm.

Edwards Yellow limestone is a rock from the geological period Early Cretaceous. The rock is composed by calcite minerals ($CaCO_3$) with pore space derived from dissolution of fossils. The pore space consists of mostly moldic pores and interparticle porosity. Original interparticle porosity reduction has happened by recrystallization of calcite and can be identified in the bulk of the rock matrix and at pore walls (Morrow & Buckley, 2006). Edwards Yellow has a high heterogeneity in pore geometry (pore size from 1 μm – 2mm) (Fernø et al., 2015). Former measurements from Skjelsvik (2018) and (Sandnes, 2020) shows a range of porosity from 22-28% and 20-29%, respectively with permeability from 14-68mD, and 14.53mD, respectively. *Silurian Dolomite* are mostly formed by dolomitization of limestone. Dolomitization means that magnesium bearing water reacts with calcium carbonate minerals and fossils in the limestone, and thereafter produces the calcium-magnesium carbonate mineral dolomite ($CaMg(CO_3)_2$). Dolomite refers to a rock that contains more than 50% of $CaMg(CO_3)_2$. The rock is highly heterogenous, where porosity may exist as intercrystallite porosity with small pores and vugs within the rock. (W. I. Anderson, 1998). Porosity ranges from 7-18%, and permeability from 11-558mD (Ruidiaz, Winter, & Trevisan, 2017). *Rørdal Chalk*, also called Portland Chalk is a rock from the geological age Maastrichtian (Period: Late Cretaceous) and deposits mainly from coccoliths. The rock is highly homogenous and consist of 99% calcite and 1% quartz. (Haugen, Fernø, Mason, & Morrow, 2015). Porosity ranges from 45-48%, and permeability from 2-7mD (Ferno, Torsvik, Haugland, & Graue, 2010).

3.2 Fluid properties

All fluids that have been used in this thesis are listed in table 3.1 with general properties as composition, density, and viscosity. Ekofisk brine have been used in limestone core samples, and chalk brine in dolomite and chalk core samples. Crude oil, decahydronaphthalene (decaline) and n-decane was utilized in the aging procedure (appendix A). CO_2 with brine was used while performing dissolution experiments.

Table 3.1 – Fluid properties.

FLUID	COMPOSITION	DENSITY [g/ml]	VISCOSITY [cP]
SYNTHETIC FORMATION BRINE (EKOFISK BRINE)	Distilled water with:	1.05 (20°C, 1 bar)[1]	1.09 (20°C, 1 bar)[1]
	NaCl: 4 wt%	1.05(40°C, 80 bar)	0.65 (40°C, 80 bar)
	$CaCl_2 \cdot 2H_2O$: 3.4 wt%	1.05 (40°C, 90 bar)	0.65 (40°C, 90 bar)
	$MgCl_2 \cdot 6H_2O$: 0.5 wt%	1.05(20°C, 80 bar)	1.09(20°C, 80 bar)
	NaN_3: 0.01 wt%	1.05 (20°C, 90 bar)	1.09 (20°C, 90 bar)
CHALK BRINE	Distilled water with:	1.05 (20°C, 1 bar)[2]	1.09 (20°C, 1 bar)[2]
	NaCl: 5 wt%	1.05(40°C, 80 bar)	0.65 (40°C, 80 bar)
	$CaCl_2 \cdot 2H_2O$: 5 wt%	1.05 (40°C, 90 bar)	0.65 (40°C, 90 bar)
	NaN_3: 0.01 wt%	1.05(20°C, 80 bar)	1.09(20°C, 80 bar)
		1.05 (20°C, 90 bar)	1.09 (20°C, 90 bar)
N-DECANE	Mineral oil, $C_{10}H_{22}$	0.73 (20°C, 1 bar)[3]	0.91 (20°C, 1 bar)[3]
		0.68 (80°C, 1 bar)[3]	0.44 (80°C, 1 bar)[3]
		0.72 (40°C, 90 bar)[3]	0.77 (40°C, 90 bar)[3]
		0.74(20°C, 90 bar)[3]	1.01(20°C, 90 bar)[3]
DECAHYDRONAPHTHALENE	Mineral oil, $C_{10}H_{18}$	0.89 (20°C, 1 bar)[4]	0.85 (20°C, 1 bar)[4]
NORTH SEA CRUDE OIL	Acid number: 0.09mgKOH/g Base number: 1.2mgKOH/g Saturates: 53 wt% Aromates: 35 wt% Resins: 12 wt% Asphaltenes: 0.9 wt%	0.85 (80°C, 1 bar)[1]	2.70 (80°C, 1 bar)[1]
CO_2	>99.99% CO_2	0.28 (40°C, 80 bar)[3]	0.02 (40°C, 80 bar)[3]
		0.49 (40°C, 90 bar)[3]	0.03 (40°C, 90 bar)[3]
		0.83(20°C, 80 bar)[3]	0.08(20°C, 80 bar)[3]
		0.84 (20°C, 90 bar)[3]	0.08 (20°C, 90 bar)[3]
		0.0018 (20°C, 1 bar)[3]	0.015 (20°C, 1 bar)[3]

[1]Values obtained from (Fernø et al., 2015) NaN_3 is added to prevent bacterial growth.
[2]Values obtained from (Arne Graue, Viksund, Eilertsen, & Moe, 1999)
[3]Values obtained from (Lemmon, McLinden, & Friend, 2012)
[4]Values obtained from (Ferno et al., 2010)

3.3 Core sample preparations

Core samples were rinsed with distilled water to remove impurities from the surface (debris from the coring process) and then dried in a heating cabinet for minimum two weeks with temperature of 60˚C. The weight of the dried core samples was measured (matrix weight) before saturation of core samples. Effective porosity and absolute permeability were measured on all the core samples.

3.3.1 Saturation of core samples and porosity measurements

Dry core samples were saturated with their respective brine using the setup shown in figure 3.1 and the experimental procedure described below. First, the dried core samples and brine were placed in their respective container and mounted in the experimental setup. The condensation trap was placed in a thermos with liquid nitrogen (N_2) for cooling the condensation trap during air evacuation. A vacuum pump was used to evacuate the air from the core samples and the brine container, respectively. The brine container was air evacuated for 10 minutes and the core samples for >1 hour, preferentially below 100 - 500mTorrent. The valve between brine and core sample containers were thereafter opened and core samples were completely covered with brine. Some brine was left in the brine container to avoid pressure increase in the core sample container. The core samples were kept under vacuum with brine for minimum 24 hours, to assure fully saturated core samples. The core samples were removed from the container and the surface of the samples were carefully dried with a tissue. Thereafter the weight of each brine saturated core sample was measured. Immediately after, core samples were stored in containers with brine to prevent evaporation.

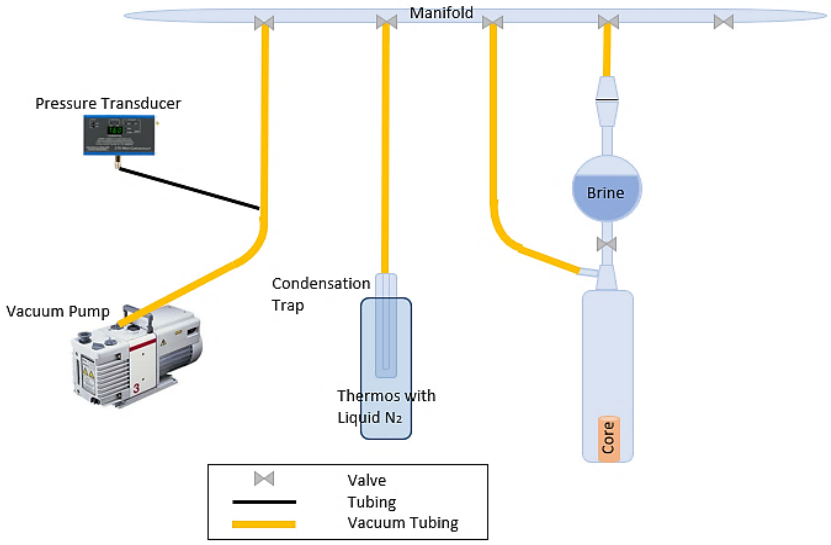

Figure 3.1 – Experimental setup used to saturate core samples with their respective brine. Thermos with liquid nitrogen was used to cool down the condensation trap.

Measurements of effective porosity of the core samples was conducted by the *saturation method*, where the weight of the dry core sample (m_{dry}) and the weight of the brine saturated core sample ($m_{saturated}$) is found. The differential mass of the core sample was used to find the fluid volume that is equivalent to

the pore volume, V_p, when the core sample is 100% saturated with brine (S_w = 1). The effective porosity was calculated by material balance:

$$\emptyset = \frac{V_p}{V_b} = \frac{m_{saturated} - m_{dry}}{\rho_{brine} \cdot L \cdot \pi r^2} \quad (3.1)$$

Where ρ_{brine} is the density of brine, L is the length of the core sample and r is the radius of the cross-section area.

3.3.2 Absolute permeability measurements

Absolute permeability of the core samples were measured by using a setup shown in figure 3.2. The core sample was placed inside a Hassler biaxial core holder. Confinement pressure to the core sample of 10-15bars above differential pressure was applied to assure fluid flow only through the cross section of the core sample (prevent fluid flow around the core sample). The core sample was connected to a Quizix pump by the end pieces in the core holder and brine was injected at four different volumetric flow rates (Q) between 20-500ml/h depending on the core sample. Lower flow rates (20-110ml/h) for Rørdal Chalk and higher flow rates for Edwards Yellow and Silurian Dolomite (50-500 ml/h). The steady state differential pressure (dP) across the unit length of the core sample was measured during injection at the different flow rates. The measured differential pressure was plotted as a function of flow rate, with a linear trend line. Then differential pressure was adjusted such that the offset in the linear trend line was equal to zero. Absolute permeability for each core sample was calculated by using Darcy's law with the adjusted differential pressure, and the respective brine viscosities:

$$K = \frac{Q \cdot \mu \cdot L}{A \cdot dP} \quad (3.2)$$

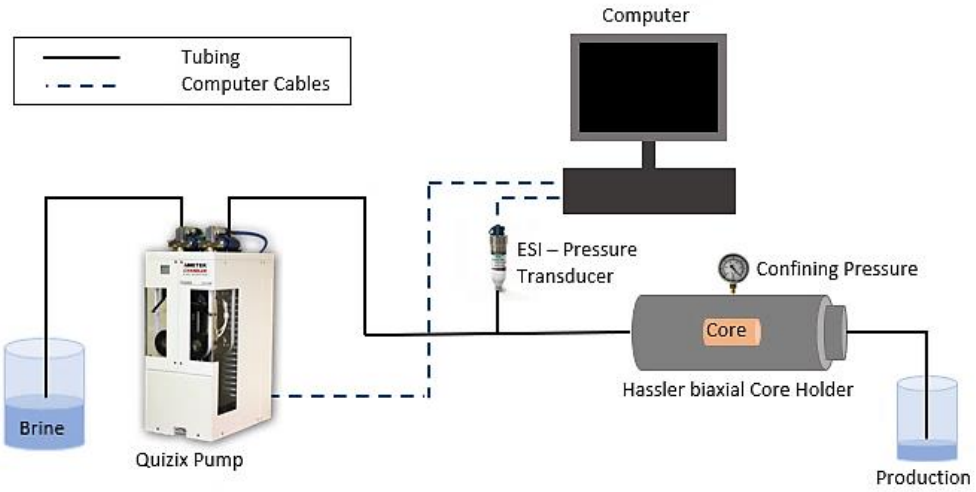

Figure 3.2 – Experimental setup used for measuring absolute permeability. The differential pressure was measured from an ESI pressure transducer at inlet side. ESI pressure transducer had a range from 0-10bars for measurements on Edwards Yellow limestone core samples, and 0-16bars for Portland chalk and Silurian dolomite. Different ranges for pressure transducer were chosen to match the differential pressure range for the core samples, to minimize uncertainties.

3.3.3 Fracturing procedure

Dissolution experiments were conducted in fractured core samples since fractures are a common feature in carbonate rocks. And a direct flow of CO_2 with brine into a restricted volume of the core sample was intended to enable a controlled dissolution. A special device designed at the mechanical workshop at the Department of Physics and Technology in Bergen was used for fracturing the core samples. The design was inspired by the Brazilian test procedures described by Cote and Thimus (1999). The weight of the core samples was measured before fracturing. The device used during fracturing is shown in figure 3.3. The limestone core samples were split into two pieces by horizontally placing the core sample between two metal plates. The metal plates have core shaped tracks with sharp edges placed at the center along its entire length. The sharp edges reduce the area of stress between the device and the core sample, accelerating the making of a fracture and facilitating vertical stress vectors. Stress from a hydraulic press (Enerpac) was gradually applied to the device until the core sample was fractured. The hydraulic press can deliver a maximum overburden pressure of 700bars and was regulated manually by a handle. A pressure gauge was installed allowing pressure readings while fracturing. The approximate overburden pressure that was needed to make a fracture in limestone was 20bars (equivalent with around 2 tons). Loose particles from the fracturing procedure were gently removed and the weight after fracturing was measured for obtaining the amount of lost particles and pore volume during fracturing.

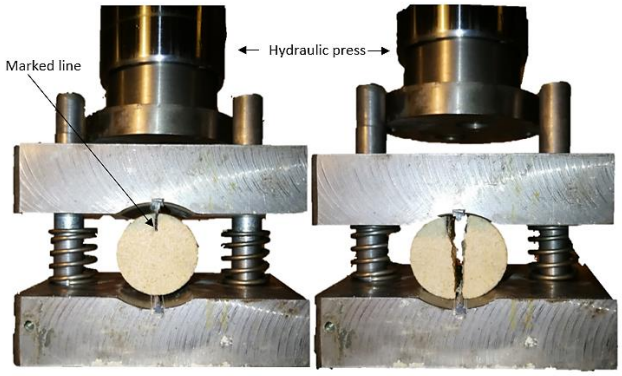

Figure 3.3 – Fracturing device with a limestone core sample before and after fracturing.

Two different sharp edges were used for splitting the core samples (figure 3.4). Core sample L1, L2, and L3, were split with sharp edges shown in (A), whereas for L4 and L5 sharp edges displayed in (B) were used. The sharp edges (A) give a substantial loss of particles during fracturing procedure leaving the fractures more open. Sharp edges were modified (B) to be thinner and with a smaller angle, for decreasing the surface of the core sample that was put to stress by the hydraulic press. Thinner, and smaller angle on the sharp edges gives a minimal loss of particles during fracturing, leaving a tighter fracture. The properties of the sharp edges controlled the aperture of the fracture, in addition, heterogeneities within the longitudinal sides of the fracture.

Figure 3.4 – (A) Sharp edges used to split core samples in experiment L1, L2 and L3. (B) New modified sharp edges used to split core sample L4 and L5.

3.3.4 Micro-CT imaging

Micro-CT images of all core samples were conducted before dissolution experiments, using a ProCon X-Ray CT-ALPHA Computed Tomography scanner. The purpose of CT-scanning before dissolution was to visualize and quantify pore structure and heterogeneities in the core samples to which changes in pore structure after dissolution could be compared. The CT-scanner was equipped with a 125kV micro-focus tube and a 3000x3000pixel detector and was operated by personnel working at the Earthlab, UoB. A piece of folded tape was first attached to one side of the core sample, in addition a marked line was drawn correspondingly to the tape as seen in figure 3.5 to control the orientation of the core sample in images. It was important to have control over the orientation of core samples during CT and PET scans, to have the ability to align and compare the pore structure in the images from the different modalities. It was especially important to have a reference point in micro-CT conducted before experiments. Figure 3.5; (A) shows a micro-CT scan conducted before fracturing procedure and dissolution. The marked line indicates where the fracture was placed in fracturing procedure. (B) shows a picture of a core sample after fracturing procedure with marked line. (C) shows a picture of marked lines on the side of the core sample after dissolution. Throughout PET-scans, the marked line was placed horizontally and towards the left side of the inlet of the core holder. The core sample was then placed on a rotating device in a CT shield cabinet as shown in figure 3.6. The core sample was placed inside a closed container filled with its respective saturation fluid and positioned vertically to the top of the rotating device. The core sample was scanned in a continuous helix motion with 1600 projections per rotation, and exposure time of 500ms. The spatial resolution in CT-image was sample size dependent. Micro-CT images were reconstructed with a spatial resolution of 29.2µm (before-scans for all core samples) and 29.7µm (after-scan for L1, L3 and L5).

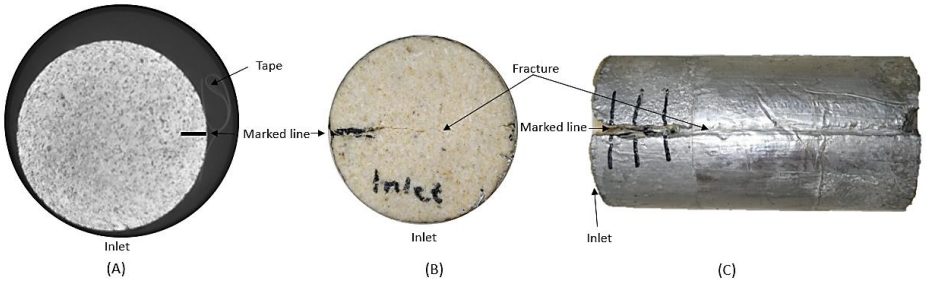

Figure 3.5 – The figure demonstrates how orientation and positioning of fracture was controlled.

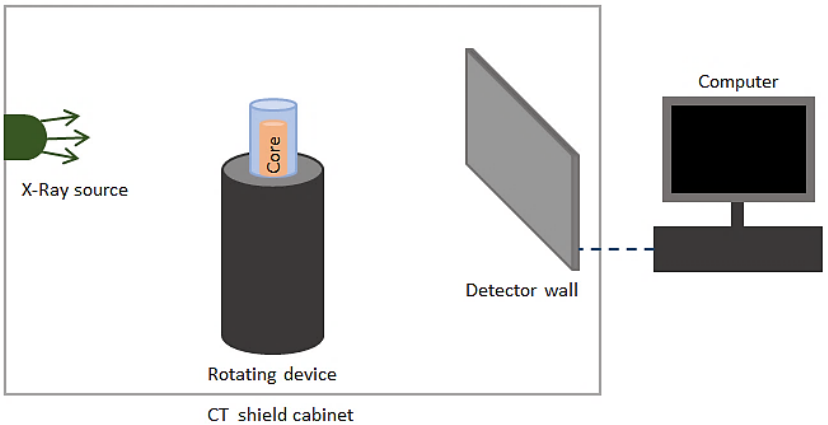

Figure 3.6 – A simple illustration of the micro-CT scanner at the Earthlab, UoB. The detector wall is positioned to the desired voxel size.

3.4 Dissolution during co-injection of CO_2 and brine

CO_2 and brine were co-injected at in-situ conditions in core sample L1, L2, L3, L4, and L5 to examine calcite dissolution. Parameters used for each experiment are listed in table 3.2. Pressure and temperature conditions were chosen to match in-situ conditions where CO_2 is supercritical and temperature of 40°C and pressure 80 or 90bar was used. The first experiment (L1) was performed under a constant pressure of 80bars and temperature of 40°C. The pressure in the pumps and BPR (pumps and BPR was placed under ambient temperature) was dependent on the temperature in the lab and it was observed that the system pressure varied with the pump pressure and BPR pressure. The lab was not well ventilated and therefore on warmer/cooler days the pump pressure and BPR pressure increased/decreased. Since 80bar was close to the phase transition from supercritical CO_2 to gaseous CO_2 (at 73.8bar at 40°C) it was decided that all other dissolution experiments were performed at a system pressure of 90bar for assuring that no phase transition occurred. The fraction of CO_2 injected was chosen to render the partial pressure of CO_2 close to the total system pressure (80 or 90bars), based on the former study (Luquot & Gouze, 2009) explained in section 2.2.5, in addition to match the fraction of CO_2 used in foam/CO_2-experiments for EOR purposes, that is often performed by the Reservoir physics group at UoB.

Based on the previous studies (Ott & Oedai, 2015; Snippe et al., 2020) explained in section 2.2.5, development of wormholes in whole core samples happened at volumetric flow rates in the higher region: for single-phase RT, ~20-70ml/h, and for two-phase RT approx. >70ml/h. Based on this, the total volumetric flow rates used in this thesis to co-inject CO_2 and brine was 40ml/h and 80ml/h, respectively. The respective brine and CO_2 rates are presented in table 3.2. The reactive fluid flow (carbonic acid) rate was assumed to be the same as total flow rate. The volumetric flow rate of CO_2 was corrected for expansion from liquid (CO_2 pump was placed in room temperature) to supercritical properties. An expansion factor was found using density properties of CO_2 (figure 2.4 in section 2.1) between the experiment temperature (40°C) and ambient temperature (average of temperatures from 20-26°C) at respective pressure (80 or 90bar). A coiled injection tubing was used to assure that the fluids were heated to 40°C and mixed before injection.

Table 3.2 – Parameters used in dissolution experiments.

CORE ID	DURATION [h]	PRESSURE/ TEMPERATURE [bar]/[°C]	FRACTION CO_2	FLOW RATE TOTAL [ml/h]	FLOW RATE BRINE [ml/h]	FLOW RATE CO_2 [ml/h]	EXPANSION FACTOR CO_2
L1	96	80/40	0.80	20, 40, 80, 160	4, 8, 16, 32	5.54, 11.08, 22.16, 44.31	0.35
L2	96	90/40	0.80	40	8	19.34	0.60
L3	96	90/40	0.80	80	16	38.68	0.60
L4	96	90/40	0.80	80	16	38.68	0.60
L5	96	90/40	0.80	40	8	19.34	0.60

L = EDWARDS YELLOW LIMESTONE

3.4.1 Core sample and system preparations before dissolution experiment

The fractured core sample was wrapped with aluminum foil to assure that the core halves were aligned during injection. Endpieces were attached to the core sample with aluminum tape as shown in figure 3.7. Aluminum foil was used for reducing radial CO_2 diffusion and damage to rubber equipment, such as the sleeve and O-rings in the core holder. The core sample with the endpieces was mounted in a Hassler biaxial core holder with the fracture oriented horizontally.

Figure 3.7 – On left-hand side, the core sample and end pieces wrapped in aluminum foil for preventing CO_2 migration. On the right-hand side, the core sample orientation.

The core holder was mounted in the setup (figure 3.8) and oriented horizontally to minimize gravitational effects, and confinement pressure to the core sample was applied by the ISCO-pump to approximately 12bar above system pressure. The ISCO-pump injects pump oil between the core holder and the sleeve for maintaining a net overburden pressure. Then the setup tubings and valves were filled brine. An Equilibar backpressure regulator (BPR) shown in figure 3.8 was pressurized using a nitrogen-tank to experimental pressure conditions. The backpressure regulators were used to maintain a constant pore pressure during experiments. BPR1 was pressurized with approximately 3 bars above BPR2, for minimizing pressure fluctuations in the system. Further, the whole setup with the core holder and brine pump (QX5000 pump) was simultaneously pressurized to 80 or 90bar in the heating cabinet at 40°C using brine. The confinement pressure was adjusted manually and parallelly to the system pressure for minimizing the risk of crushing the core sample. The CO_2 pump (QX6000 pump) was pressurized to a liquid phase via a Proserv gas booster and was on standby for CO_2 injection. Brine and CO_2 pumps were controlled by the Quizix PumpWorks Software. The system was tested for leakages by leaving the system without injection for several hours while inlet, outlet, BPR and pump pressures were monitored. An inline pH meter was placed directly after the BPR on the production tubing (ambient condition due to pressure and temperature limitations in the pH electrode). The pH electrode was attached to a pH meter (Ati q45p) and the electrode was calibrated using two different buffer-solution with pH of 4 and 7. Brine injection was performed to measure the permeability of the fractured core sample under experimental conditions using five volumetric flow rates: 100, 150, 200, 150 and 100ml/h, and to measure initial pH conditions. The brine injection rate was thereafter adjusted to measure an initial steady state baseline pressure of brine injection (the respective flow rates are shown in table 3.2). Pressure readings during permeability measurements and baseline injection was obtained by a Alipsens Smart Differential Pressure Transmitter with a range of 0-2.5bar.

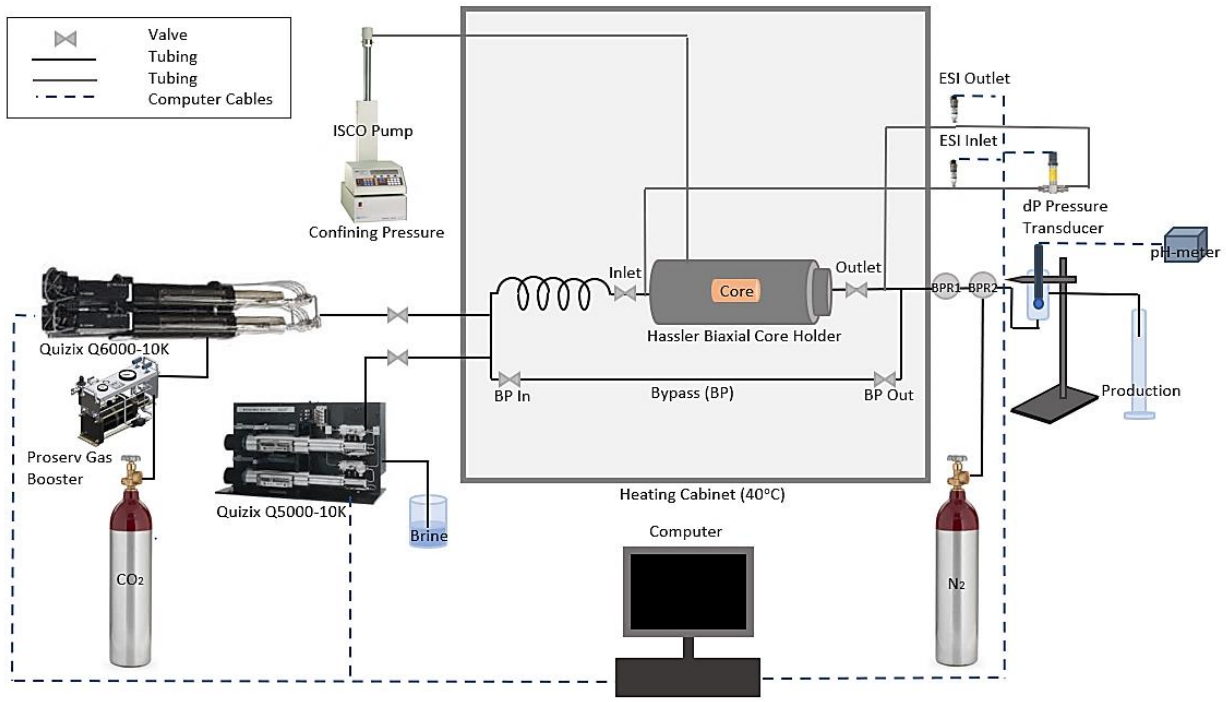

Figure 3.8 – Experimental setup used for calcite dissolution experiments by co-injection of CO_2 and brine. The setup was heated and pressurized such that the CO_2 is at supercritical phase.

3.4.2 Co-injection of CO_2 and brine

Co-injection of CO_2 and brine through the bypass for minimum 0.5hours was performed for stabilizing the system and measuring the pH of the mixed co-injected fluids by the inline pH electrode. The pH measurements were obtained when the electrode was covered with the brine phase. It was important to measure pH when the electrode was covered with the liquid phase, for the purpose to measure the calcite affected phase. Bypass valves were closed, and inlet and outlet valves of the core holder was opened to start co-injection through the core sample. Co-injection lasted for 96hours (4 days), where differential pressure (by Alipsens pressure transducer for more accurate pressure readings), pH and effluents (production volume) where measured and monitored. In addition, pressure at outlet and inlet of the core sample, pressure of the BPR's, and confinement pressure were monitored by four ESI pressure transducers with a range from 0 -100bar and 0-250bar. The volume of effluent was measured for the purpose to produce water production curves that could be used for quantifying the pore volume that had been swept by the co-injected fluids. However, the water production curves were decided to not be considered in this thesis because of large uncertainties. Due to the flow rates chosen, the effluents were produced in cylinders with a considerable uncertainty, in addition, the effluents contained a substantial amount of produced white particles, which leaved the reading of produced water volume difficult. Filtration of white particles from the effluents was also performed (Appendix B), which added uncertainty to the water production curves. During filtration water droplets spills or get stuck in effluent container, leaving an even higher uncertainty in water production measurement.

After co-injection for 4 days, the CO_2 pump was stopped, and injection of brine continued for 24hours to remove CO_2 from the core sample. Brine was injected at 100ml/h the first hour and thereafter set to 10ml/h. A low flow rate was chosen for minimizing further changes (dissolved particle movement etc.) in the core sample while brine was injected. Final steady state brine pressure and absolute fracture permeability was measured in the same manner as initial brine baseline and fracture permeability. A final brine pressure and absolute permeability was measured for comparison to the initial baseline and permeability. The brine pump was set to a retract mode and depressurization of the system started. Depressurizing the system to ambient conditions was done slowly (due to the transition of possible left-over CO_2 from supercritical to gaseous phase around 73.8 bars and 40°C. The expansion is harsh to the equipment and can cause damage/swelling of the sleeve and O-rings). The confinement pressure was adjusted parallel with the system pressure. The core holder with the core sample was taken out of the system and the core sample was disassembled and placed in a container filled with brine. Final permeability was verified by measuring the absolute permeability in ambient conditions, using the same setup as shown in section 3.3.2 with 12bars confinement pressure and an ESI pressure transducer, to assure that the offset in the differential pressure during four days of experiments did not change substantial, and that the final permeability was correct. The final permeabilities measured in ambient conditions were approximately the same as the final permeabilities, therefore the offset during four days of experiment did not change and hence did not affected the final permeability measurements.

3.4.3 Injection of traceable brine during PET/CT-imaging

After dissolution experiments with supercritical CO_2, core sample L1, L2 and L3 was taken to Centre for Nuclear Medicine and PET, Department of Radiology, Haukeland University Hospital in Bergen for PET/CT-scans. Preclinical PET/CT-scans were conducted using a nanoScan PET/CT, and clinical PET/CT-scans were conducted using a Siemens Healthineers scanner under ambient pressure and temperature regime.

PET/CT-scans were conducted to examine flow paths during brine flood with ^{18}F as tracer (i.e., examine reactive fluid flow). The tracer was first produced and delivered by a physicist at Haukeland University hospital. ^{18}F was synthesized to ^{18}F – fluorodeoxyglucose (^{18}F-FDG also called FDG) and stored in a lead vault inside the PET/CT lab. The tubings (figure 3.9) were first filled with brine. Then the core sample was mounted in the core holder and setup. The core holder was special made, adapted to the preclinical PET/CT scanner bed. Confinement pressure with a net overburden pressure of around 12bars to the core sample was applied by an ISCO pump. The system was tested for leakage and the core holder was wrapped with plastic bags to assure that no brine with tracer was spilled inside the PET/CT-scanner during injection. Before PET-scan, a CT-scan was performed, both for retrieving a CT-image for analysis, and for the purpose to position the core sample correctly for the PET-scan. It was important that the whole core sample with the inlet tubing was in the field of view. The PET/CT-scanner was operated by Bergit Brattekås, researcher in the Reservoir Physics group, UoB. After positioning, the start activity of the stored FDG was measured by Heidi Espedal, senior engineer and leader at small animal PET/CT facilities, Haukeland University Hospital. FDG was then mixed with brine and the brine pump (QX 5000 pump) was filled with the radioactive brine (brine pump was emptied before filling it with brine with FDG). The pump was set to the respective flow rate displayed in table 3.3. Two flow rates for each experiment were used: the total flow

rate and the brine flow rate. For L1 the highest out of four rates were used. The core holder was positioned in the PET/CT-scanner and the injection of brine mixed with tracer was started. The PET-scans were conducted with a time frame up to 1.15hours. Pore volume (PV) injected at respective flow rate is displayed in table 3.3. Differential pressure during injection of brine with FDG was measured by two ESI pressure transducers with range from 0-100bars, connected to a Alipsens Smart Differential Pressure Transmitter with a range of 0-16bars for more accurate pressure recordings. After PET-scanning the set up was left untouched for about 24hours to minimize the exposure of radioactive radiation and allow ^{18}F to decay. The core sample and setup were thereafter disassembled from the PET/CT-scanner and the core sample was then stored in a container filled with brine.

Imaging techniques applied for the respective core samples are displayed in table 3.3. Core sample L3 was scanned with clinical PET/CT-scan for comparison to preclinical PET/CT. Clinical PET/CT-scan was conducted directly after preclinical PET-scan still containing activity from the F^{18} isotope. The valves attached to inlet and outlet of the core holder was closed and disassembled from the setup shown in figure 3.9 and the core holder with the core sample containing FDG was carefully and quickly transported to the clinical PET/CT scanner. The whole core holder was placed on the bed of the scanner and thereafter scanned by own operators at Centre for Nuclear Medicine and PET, Department of Radiology, Haukeland University Hospital. The core holder was left untouched until the FDG had decayed totally, and the core sample was then disassembled and stored in a container filled with brine.

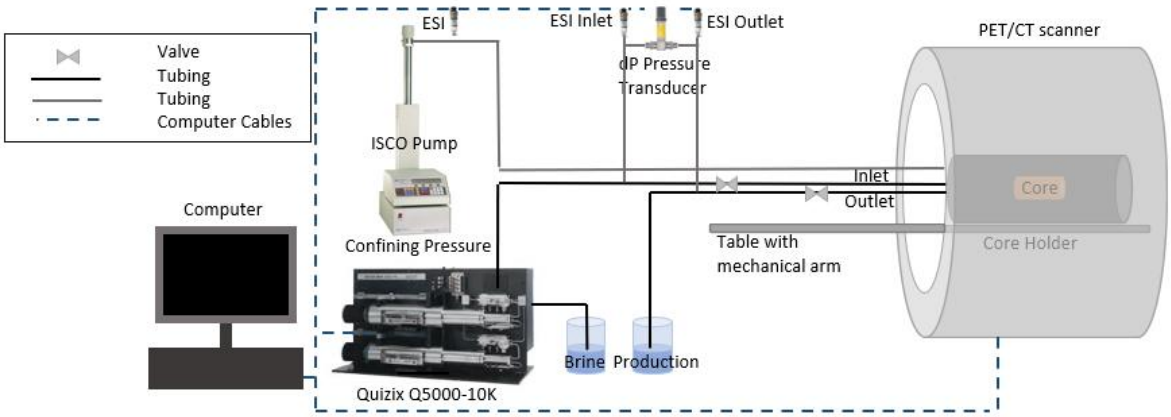

Figure 3.9 – Experimental setup used for low pressure PET/CT-imaging by injection of F^{18}-brine.

Table 3.3 – Imaging techniques and modalities, and parameters used during PET-scans. Brine is mixed with F^{18} and then injected into the core sample.

CORE ID	PET/CT MODALITIES	BRINE WITH F^{18} [ml]	F^{18} - START ACTIVITY [MBq]	VOLUMETRIC FLOW RATE [ml/h]	PV INJECTED (BRINE + ^{18}F -FDG)
L1	Preclinical PET+CT	100	132	160, 32, 160 #2	1.74, 0.65, 1.05
L2	Preclinical CT	-	-	-	-
L3	Preclinical and clinical PET+CT	150	333	80, 16	2.12, 0.17

L = EDWARDS YELLOW LIMESTONE

4 Results and discussion

This chapter presents results and discussion of the experimental work conducted in this thesis. Basic core sample properties for ten Edwards yellow limestone, two Silurian dolomite, and three Rørdal chalk were obtained. A micro-CT scan was conducted on all the core samples before fracturing procedure and dissolution. Micro-CT images were used for rock quantification. Four Edwards yellow limestone cores (L7-L10) were dynamically aged, and the theory, procedure, results, and discussion can be found in appendix A. Fracturing procedure and dissolution experiments were performed on five water-wet Edwards yellow limestone cores for investigation of dissolution propagation. Co-injection of brine and CO_2 into the cores were used to promote dissolution. Preclinical and clinical PET/CT-scans were performed after dissolution, for both dissolution and flow pattern analysis. CT-images were used to visualize and quantify pore/fracture structures and dissolution patterns, while PET-images were used to visualize and quantify dissolution and dissolution patterns by reactive fluid flow. Core sample L1, L3, and L5 was scanned with micro-CT after dissolution for quantification of pore/fracture structure and for comparison to initial images for obtaining changes in the cores caused by dissolution. Dissolution patterns and reactive fluid flow was examined by comparing global measurements to in-situ visualization.

4.1 Basic core properties

Basic core properties were measured for ten Edwards yellow limestone core samples, two Silurian dolomite core samples, and three Portland chalk core samples, and are listed in table 4.1, including dimensions, effective porosity, pore volume, and absolute permeability. The core sample length varied from 61.4-76.1mm, with a diameter from 37.8-38.6mm. Effective porosity ranged from 22.3-27.5% for limestone cores, 12.1-16.5% for dolomite cores and 46.1-46.4% for chalk cores. The range in absolute permeability was from 15.4-41.4mD for limestone, 4.36-189mD for dolomite, and 4.17-5.35mD for chalk. A linear relationship between permeability and porosity for Edwards yellow limestone was obtained, as shown in figure 4.1. The linear relationship was more apparent for lower porosity values than for higher values. The same number of measurements was performed in the lower range of porosities as in the higher range. Higher porosity values may vary more due to more heterogenous core samples with vugs present. A linear trend between porosity and permeability is not common in highly heterogeneous core samples, i.e., the limestone cores used in this thesis were less heterogeneous. A linear trend for the same core material was also obtained by Sandnes (2020) and Tipura (2008). Basic core properties of limestone core samples were measured in earlier work. Sandnes (2020) evaluated 29 different Edwards yellow limestone core samples, where porosity ranged from 20-29%, and permeability ranged from 14-53mD. Former measurements from Skjelsvik (2018) shows a set of 17 limestone core samples with porosity from 20-29%, and permeability from 14-68mD. Tipura (2008) evaluated 34 limestone core samples that had a range in porosity from 16-27%, and permeability 2-29mD. The limestone core samples used in this thesis came from the same supplier and batch as the core samples utilized in previous work by Sandnes (2020), and corresponded well with the measured ranges.

From Ruidiaz et al. (2017) porosity for dolomite core samples ranged from 7-18%, and permeability from 11-558mD. The porosity, and hence the permeability varies significantly within dolomite core samples due

to dolomite cementation. Dolomite cementation causes a typically lower porosity for dolomites than their limestone precursors (Moore & Wade, 2013). In this thesis porosity of dolomite core samples did not vary significantly, but only two cores were evaluated which was not enough to estimate a trend in porosity range. The permeability varied considerably for the two cores, indicating highly heterogenous dolomite core samples. Chalk core samples are usually of a very homogenous character, where Ferno et al. (2010) found a range in porosity from 45-48%, and permeability from 2-7mD for Rørdal chalk. The measured ranges in this work corresponds well with the previous measurements.

Table 4.1 – Measured core sample properties; dimensions (length and diameter), effective porosity, pore volume, and absolute permeability before fracturing.

CORE ID	L [mm] ± 0.1	D [mm] ± 0.1	Ø [%] ±0.02	PV [ml] ±0.01	K [mD] ±0.5
L1	73.1	37.8	22.31	18.30	17.1
L2	73.3	37.8	24.60	17.77	15.4
L3	70.0	37.8	23.97	18.83	25.3
L4	69.6	37.8	26.74	20.89	33.8
L5	67.8	37.8	22.57	17.17	18.8
L6	67.5	37.8	23.23	17.60	24.9
L7	65.9	37.8	26.92	19.90	39.5
L8	64.1	37.8	26.85	19.31	39.1
L9	62.5	37.8	27.52	19.30	39.9
L10	61.4	37.8	25.71	17.71	41.4
D11	63.9	38.6	16.51	12.34	189
D12	76.1	37.8	12.02	10.27	4.4
C13	76.1	38.0	46.08	39.77	5.4
C14	75.3	37.9	46.41	39.43	5.1
C15	75.3	38.4	46.22	40.30	4.2

L = EDWARDS LIMESTONE, D = SILURIAN DOLOMITE, C = RØRDAL CHALK

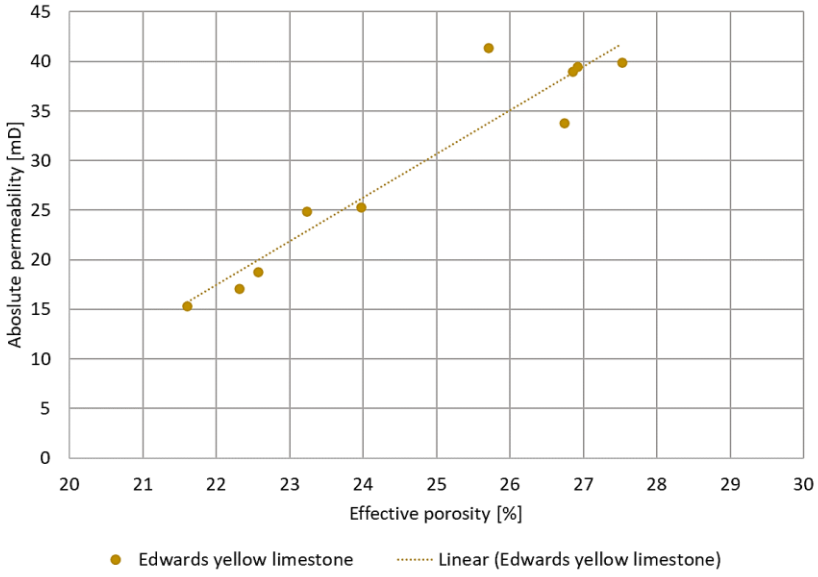

Figure 4.1 – Linear effective porosity vs. absolute permeability trend for Edwards yellow limestone core samples.

4.2 Core quantification with micro-CT imaging

A ProCon X-ray CT-ALPHA Computed Tomography (micro-CT) scanner at the Department of Geoscience, UoB, was used for CT-imaging of 15 core samples. Three core samples: L2 with low permeability (15.4mD), L10 with high permeability (41.4mD) and D12 with low permeability (4.36mD) were further examined for quantification of heterogeneities. The spatial resolution of the CT-images was 29.2μm. Pores smaller than the spatial resolution were not visible in CT-images. Rock quantification of Rørdal chalk core samples was not performed due to its expected homogenous nature with respect to pore size and pore throat distribution (Johannesen, 2008). Micro-CT images and a visual analysis of C13, C14 and C15 are provided in appendix C.

Figure 4.2 shows a cross section from a micro-CT image of the whole length of core D12, with segmented pore network. Pores with a large variety of sizes, including large vugs were displayed in the image. The measurable pore sizes for D12 varied from 33-7663µm. D12 was dominated by vugs and cemented areas. The cemented areas might explain the low measured permeability, given that a small proportion of the vugs and pores were connected (bright areas in figure 4.2). Figure 4.3 displays axial cross sections from micro-CT of L2, L10 and D12. A diversity of pore sizes, including vugs, can be seen in these cross sections. The proportions of vugs may explain the variety in permeability along with connectivity of vugs in L2, L10 and D12. If the vugs connects to pores and other vugs, it most likely gives a higher permeability, whereas vugs with no connection to other pores and vugs is insignificant to the permeability. For L1, pore sizes ranged from 33-2430µm, and for L10 from 33-3095µm, indicating core samples of a highly heterogenous character. The largest vug in diameter for L2, and L10 was approximately 2500µm and 3000µm, respectively. Tipura (2008) observed pores as large as 2000µm in a thin section of Edwards yellow limestone in her work, also Sandnes (2020) found vugs in several Edwards yellow limestone cores using micro-CT images, with diameters of approximately 2000µm.

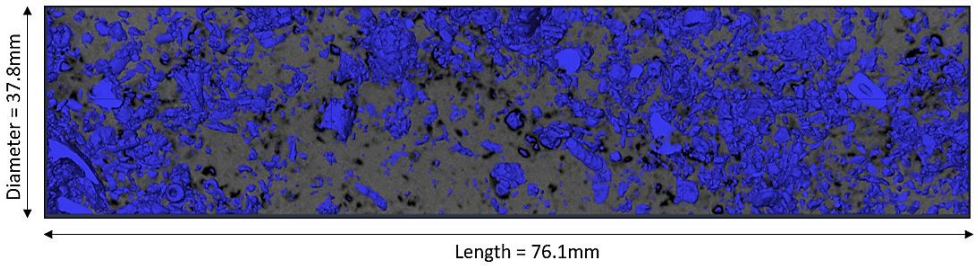

Figure 4.2 – Cross section micro-CT image of D12 with segmented pores (blue) overlying CT-image (greys and black). Note that the micro-CT images have a voxel size of 29.2µm, therefore were pores under this value not captured.

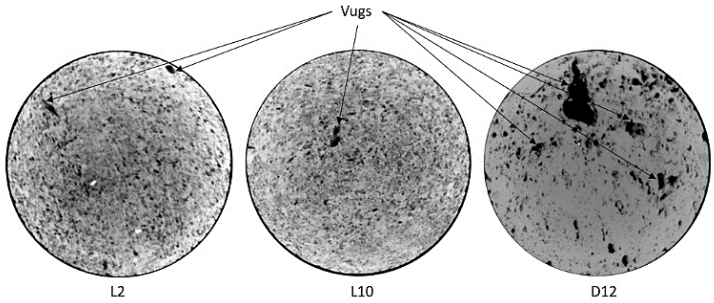

Figure 4.3 – Cross sections from micro-CT images for core sample L2, L10 and D12 confirms vugs. Note that the core sample diameter is 37.8mm in all three core samples.

Pore size distribution for L2, L10 and D12 was obtained from micro-CT images using ImageJ FIJI, which is an image processing software. A micro-CT image of L2 and L10 contains 2160 dicom files (slices), respectively, whereas D12 contains 2201 slices. The slices are stacked together displaying the whole core sample, but due to limitations in computer performance, an increment of slices (cross sections), every other 2mm through the core sample were chosen for measuring pore size distribution. In addition, 2mm between each cross section was selected to minimize double counts of pore sizes. Trainable Weka segmentation, which is a plugin in FIJI was used to threshold the grayscale images to binary images. A default version of thresholding was first tried, but the binary images did not correspond well enough with the overlying CT-image. So, the thresholding was adjusted manually in the trainable Weka segmentation until the overlying CT-image matched the binary image. In each binary image, area of each pore was calculated by the function "analyze particles" in FIJI. Thereafter, the pore diameter was manually calculated in excel by using simple geometry calculations assuming that each pore was a sphere. Figure 4.4 display the pore size distribution for L2, L10 and D12. The plots represent the frequency of each measured pore diameter through the core samples. In L2, the largest proportion (~30%) of pores visible in micro-CT images had a diameter of ~33µm, and the largest proportion (~39%) in L10 also, had pore diameters of ~33µm. For D12 the largest proportion of pores (~60%) had a pore diameter of ~34µm. A minor quantity of pore and vug diameters were in the range ~40-2430µm (L2), ~50-3095µm (L10), and ~110-7663µm (D12). L10 generally had pores and vugs with larger diameter than L2, which may explain a higher permeability in L10, than in L2.

The micro-CT images and pore size distributions confirm the expected heterogeneous nature of Edwards yellow limestone core samples, with a large range in pore sizes and presence of vugs.

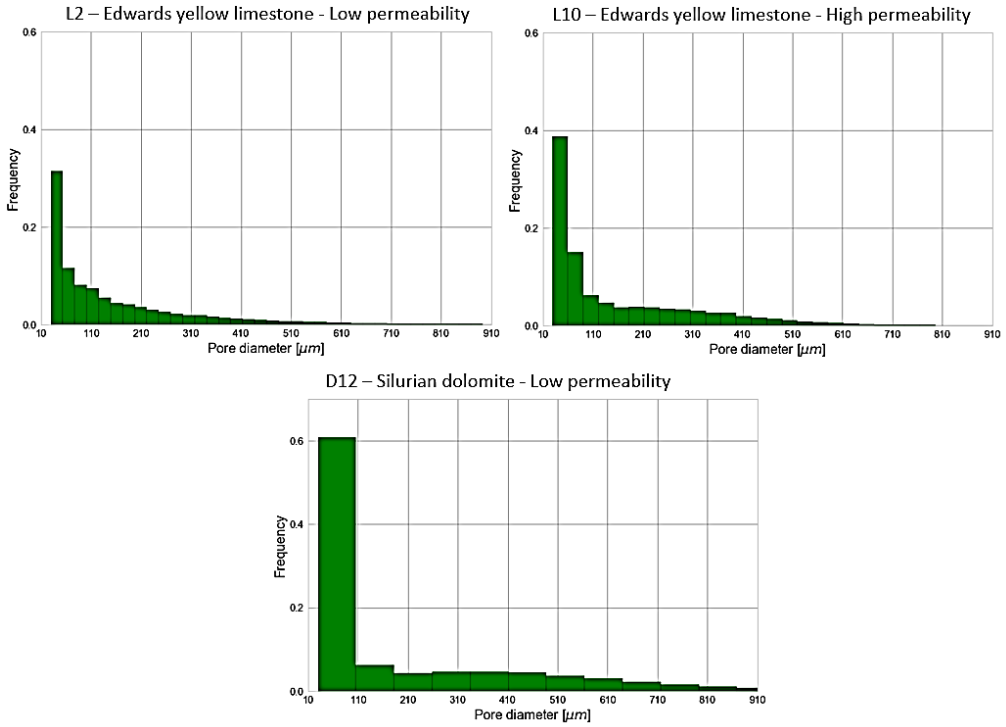

Figure 4.4 – Pore size distribution for core sample L1, L10 and D12 obtained using micro-CT images. The pore diameter is the diameter of the pore bodies assumed as spheres. Micro-CT images was scanned with a voxel size of 29.2µm, therefore pores beneath this value could not be measured.

4.3 Characterization of fracture networks

Fractures are a common feature in carbonate rocks, and dissolution experiments were therefore performed with fractured limestone core samples. The core samples were fractured as described in section 3.3.3 with two different sharp edges as also displayed in figure 4.5. Two different sharp edges were used to get a desired fracture characteristic. Sharp edges (A) were used to split core sample L1, L2, and L3 where a preferential flow channel within the fracture was intended. A preferential flow channel is characterized by heterogeneities that discriminates fluid flow by a lower capillary pressure than within the rest of the fracture and pore network (e.g. a wormhole). The sharp edges (A) were designed such that a substantial loss of particles within the longitudinal sides of the fracture occurred (figure 4.5 (A)). The average amount of lost particles during fracturing for L1, L2 and L3 was 0.94g. Sharp edges (B) were used to fracture L4 and L5, where a nearly homogenous fracture was expected. A homogenous fracture can be described by an equal fracture aperture through the whole fracture. The sharp edges (B) produced a fracture with little loss of particles (figure 2.5 (B)), in comparison to sharp edges (A) used on L1, L2, and L3. The average amount of lost particles for L4 and L5 was 0.54g. For assuring no discrimination of fluid flow in longitudinal sides of fracture in L5, the sides were sealed with silicone strips as shown in figure 4.6.

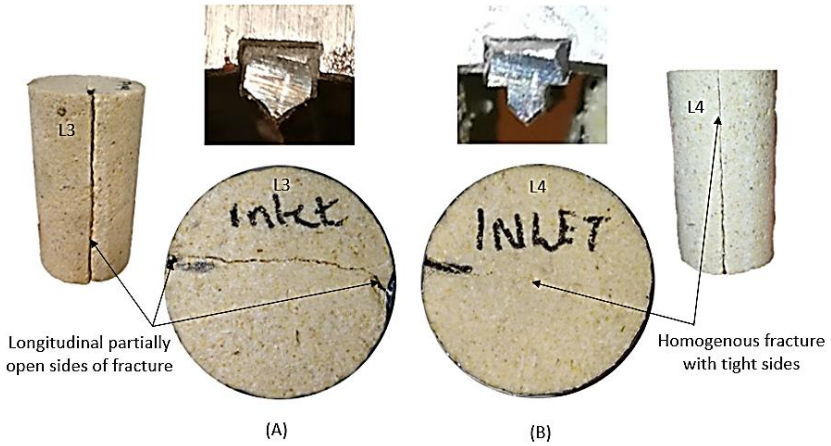

Figure 4.5 – (A) Sharp edges used to split core sample L1, L2 and L3. (B) Sharp edges used to split core sample L4 and L5.

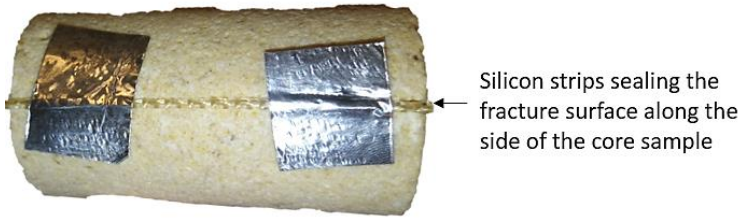

Figure 4.6 – Core sample L5, with silicon strips along the sides of the fracture, attached using aluminum tape.

Initial fracture characteristics for each core sample can be found in table 4.2. The effects on dissolution during reactive fluid flow (co-injection of CO_2 and brine) from different initial fracture characteristics are discussed more thoroughly in several sections below.

Table 4.2 – Initial fracture characteristics and sharp edges used for splitting core sample L1, L2, L3, L4 and L5.

CORE ID	SHARP EDGES USED DURING FRACTURING	INITIAL FRACTURE CHARACTERISTICS
L1	(A)	Tight with longitudinal partially open sides
L2	(A)	Tight with longitudinal partially open sides
L3	(A)	Tight with longitudinal partially open sides
L4	(B)	Tight
L5	(B)	Tight

L = EDWARDS YELLOW LIMESTONE

4.4 Dynamic dissolution from global data

Global data measured during dissolution in core sample L1, L2, L3, L4 and L5 provide a basis for calculating wormhole, dissolution pattern and fracture apertures. Comparison of steady state global data, such as differential pressure before (initial) and after (final) dissolution could provide information of the degree of dissolution, and how dissolution affected the injectivity of CO_2. In addition, to compare dissolution for the two fracture types mentioned in section 4.3 (table 4.2). Dissolution in L1, L2, and L3 was expected to take place mainly within the longitudinal partially open sides (pre-existing wormhole) of the fracture, whereas for L4, and L5 mainly within the fracture. In addition, due to dissolution, a reduction from initial to final steady state pressure was expected. Differential pressure across the unit length of the core samples was measured dynamically during the whole length of the dissolution experiment. Dynamically differential pressure was used to quantify dissolution/wormhole development and propagation, caused by co-injection of CO_2 and brine. The dissolution experiments were performed with pressure, temperature, volumetric flow rate and duration as displayed in table 4.3. Pressurized and heated system was used to obtain in-situ conditions where CO_2 was in supercritical phase. The fraction of CO_2 during injection with brine was 0.8, and it was assumed that a two-phase flow occurred during co-injection. Dissolution experiment for core sample L1, L2, L3, L4 and L5 was performed with the procedure and setup shown in section 3.4.

Table 4.3 – Parameters used during dynamic dissolution on core sample L1, L2, L3, L4 and L5. In addition, measured initial and final absolute permeability.

CORE ID	DURATION [h]	PRESSURE/ TEMPERATURE [bar]/[°C]	FRACTION CO_2	FLOW RATE TOTAL [ml/h]	INITIAL FRACTURE CONDUCTIVITY [mD]	FINAL FRACTURE CONDUCTIVITY [mD]
L1	96	80/40	0.80	20, 40, 80, 160	387±14	1370±14
L2	96	90/40	0.80	40	605±16	716±4
L3	96	90/40	0.80	80	649±6	655±5
L4	96	90/40	0.80	80	463±8	36.09±0.05
L5	96	90/40	0.80	40	38.4±0.2	25.47±0.06

L = EDWARDS YELLOW LIMESTONE

4.4.1 Dynamic dissolution in tight fractures with pre-existing wormhole

Dissolution experiment for core sample L1 was performed with parameters shown in table 4.3. Figure 4.7 shows the differential pressure during dissolution in core sample L1, in addition, steady state pressure before (larger dotted line) and after (smaller dotted line) dissolution measured during injection of brine at 160ml/h. Flow rate of 20ml/h was used the first 24hours, and white particles, assumed to be calcite, were observed in the effluent shortly after the start of co-injection though the core sample. This indicates that a reaction between carbonic acid and the limestone core sample happened at the very beginning of co-injection. White particles were produced during the whole length of the experiment, giving a milky white color of the effluent. At 0PV injected, the co-injected fluids entered the core sample inlet. From 0PV to approximately 0.5PV, differential pressure was smooth without any big pressure fluctuations, presumably due to the brine phase production from the core sample passing through the BPR. From ∼0.5PV and towards the end of dissolution, pressure fluctuations were present which strongly imply that a two-phase flow (CO_2 and carbonic acid) and dissolution/blocking by particles occurred during co-injection. Cyclical pressure fluctuations are presumably due to gas-slugs passing through BPR, caused by the two-phase flow, whereas other fluctuations are caused by rock dissolution or blocking of local areas (presumably within fracture) by dissolved particles. The difference between initial steady state pressure and co-injection pressure, as shown in the very beginning of experiment, was mainly due to density and viscosity differences, in addition to a two-phase flow. The density and viscosity are typically larger in carbonic acid than brine itself, where carbonic acid and a two-phase flow gives a larger pressure response than brine alone. From ∼1-26PV of co-injection at a rate of 20ml/h the pressure had no specific trend. The pressure was dominated by both increasing and decreasing pressure with peaks infrequently, indicating that both dissolution and blocking by dissolved particles occurred. At ∼26PV of co-injection the flow rate was changed to 40ml/h and a decreasing pressure trend was observed during the 24 hours of injection, only interrupted by an error in the pump used for CO_2-injection. The pump stopped due to overheating where the pistons got out of position probably because of a pressure increase in the CO_2-tank, when a temperature increase in the lab from around 25°C to 30°C was observed. The pump needed to be cooled down before the error could be fixed. So, for 48 hours only brine was injected between the changes in flow rate from 40ml/h to 80ml/h. The pressure during brine injection for these 48hours was not included in the plot. The pressure peak at nearly 80PV of co-injection, was where the co-injection started again, and the flow rate was set to 80ml/h. The pressure peak was dominated by another introduction of two-phase flow. A decreasing pressure trend was observed during almost the whole co-injection with a flow rate of 80ml/h. Adjusting the pressure from 80ml/h to 160ml/h at around 185PV show a direct increase in pressure due to a higher differential pressure caused by higher volumetric flow rate. The pressure during 24 hours of injection at 160ml/h was dominated by a relatively stable pressure until around ∼350PV, where the pressure was decreasing. An overall decreasing pressure trend during dissolution from injection at 40ml/h to end of dissolution strongly suggest that the preferable flow channel aperture had increased, since the pressure continues to decrease despite significant increases in flow rates (80ml/h, followed by 160ml/h). In addition, a change from infrequently pressure fluctuations (∼1-26PV; caused by dissolution/blocking) to cyclic fluctuations (∼26-390PV, caused by two-phase flow) may indicate that the preferential flow path was “cleaned”/smoothed during dissolution. The reduction in final steady state pressure during brine injection (0.035bar) supports the indication of a dissolution channel/wormhole (already established flow channel) growth during reactive fluid flow, and hence a

grater injectivity during dissolution was obtained. Steady state absolute permeability measurements before (387mD) and after (1370mD) dissolution shows an increase of 983mD, which indicates a discrimination of reactive fluid flow within the already preferable flow path, leaving most dissolution in that area.

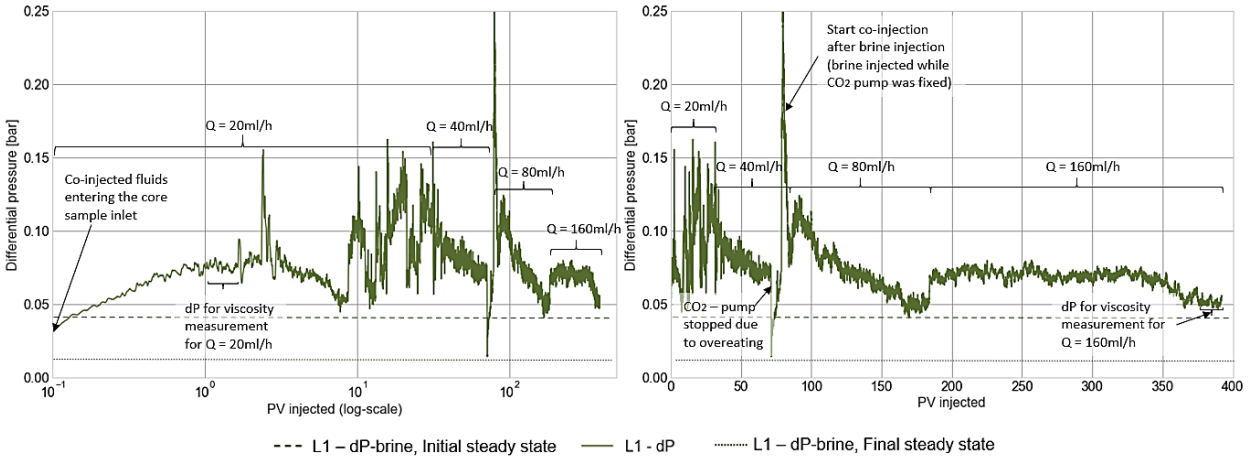

Figure 4.7 – Differential pressure evolution during dissolution in core sample L1. Plots displays the differential pressure during dissolution as a function of pore volume of co-injection. Plot on the left-hand side displays pore volumes of co-injection on a logarithmic scale for acquiring more exact pressure evolution at the start of dissolution. In addition, steady state initial and final differential pressures of brine injection were plotted for volumetric flow rate = 160ml/h.

Dissolution experiment for L2 was performed with parameters shown in table 4.3. Figure 4.8 shows differential pressure evolution during dissolution in L2. From 0PV injected where co-injected fluids entered the core sample inlet to ~0.9PV injected, no substantial pressure fluctuations were observed, as also seen for L1, which probably was due to the brine phase production passing through BPR. From ~0.9PV to the end of dissolution, pressure fluctuations were present, indicating that a two-phase flow occurred (cyclical pressure fluctuations), in addition to rock dissolution and blocking of local areas by dissolved particles (infrequently pressure fluctuations) during co-injection in L2. In addition, a change from infrequently pressure fluctuations (~0.9-15PV; caused by dissolution/blocking) to cyclic fluctuations (~15-210PV, caused by two-phase flow) may indicate that the preferential flow path was "cleaned"/smoothed during dissolution in L2. White particles in effluents for L2 were also observed from the very beginning of co-injection. After ~0.9PV injected and to the end of dissolution a decreasing pressure trend was observed, only interrupted by CO_2-tank problems. At ~25PV injected, the CO_2 tank did not contain enough pressure for the Proserv gas booster leaving large pressure drops and peaks for several pore volumes of co-injection. This event happened at nighttime and the CO_2-tank was replaced with a full CO_2 tank at the morning it was discovered. The small reduction (0.0011bars) from initial to final steady state pressure indicate that a small increase of the narrowest restriction in the already established flow channel occurred. In addition, the steady state pressure decrease might indicate that the already established flow channel discriminated the reactive fluid flow just slightly, which further can indicate that other areas (presumably fracture) were also affected by dissolution. The small reduction from initial to final steady state pressure may also imply that the dissolved calcite particles were still within the core sample or outlet tubing, and not produced in effluent. A great extent of dissolution could take place closer to the inlet side

without affecting the overall core permeability and hence the pressure particularly. The bulk permeability increased by 111mD from initial (605mD) to final (716mD) measured absolute permeability.

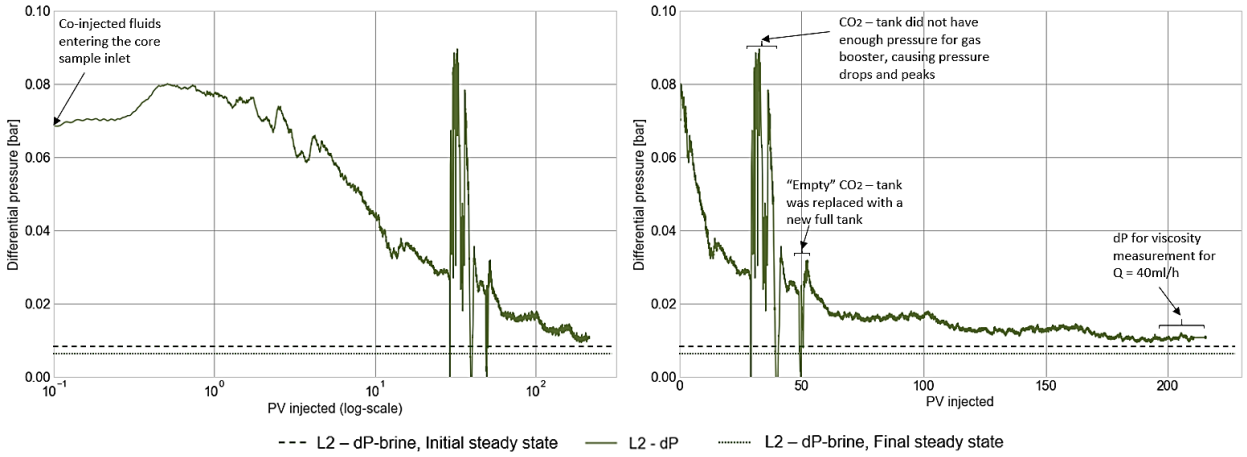

Figure 4.8 – Differential pressure evolution during dissolution in core sample L2. Plots displays the differential pressure during dissolution as a function of pore volume of co-injection. Plot on the left-hand side displays pore volumes of co-injection on a logarithmic scale for acquiring more exact pressure evolution at the start of dissolution. In addition, steady state initial and final differential pressures of brine injection were plotted for volumetric flow rate = 40ml/h.

Dissolution was performed for L3 with parameters found in table 4.3. Figure 4.9 shows the differential pressure evolution during dissolution. From 0PV where co-injected fluids enter the core sample inlet to ~0.85PV injected differential pressure was without pressure fluctuations as also seen for L1 and L2, which was due to the brine phase passing through the BPR. White particles were also observed in the effluent at the very beginning of co-injection in L3, as also seen for L1 and L2. From ~0.85PV to the end of dissolution, pressure fluctuations were present, which show that a two-phase flow (cyclical) and rock dissolution/blocking of local areas by dissolved particles (infrequently) also occurred for L3. In addition, a change from infrequently pressure fluctuations (~0.85-15PV) to cyclic fluctuations (~15-405PV) may indicate that the preferential flow path was "cleaned"/smoothed during dissolution in L3. An overall decreasing pressure trend was observed during dissolution, which indicates that the longitudinal partially open side (established flow channel) of the fracture aperture increased. The minor reduction (0.0016bars) from initial to final steady state pressure indicates that the aperture just slightly increased during dissolution, which also may indicate that the discrimination of reactive fluid flow was not substantial for the pre-existing wormhole. This can indicate that other areas, like the fracture, might have been affected by the reactive fluid flow or that dissolved particles were left behind in the core sample or outlet tubing. However, dissolution can take place close to the inlet side without affecting the pressure and can, hence, not be determined from global measurements of pressure and flow rate. The bulk permeability for L3 only increased by 6mD from initial (649mD) to final (655mD) measured absolute permeability.

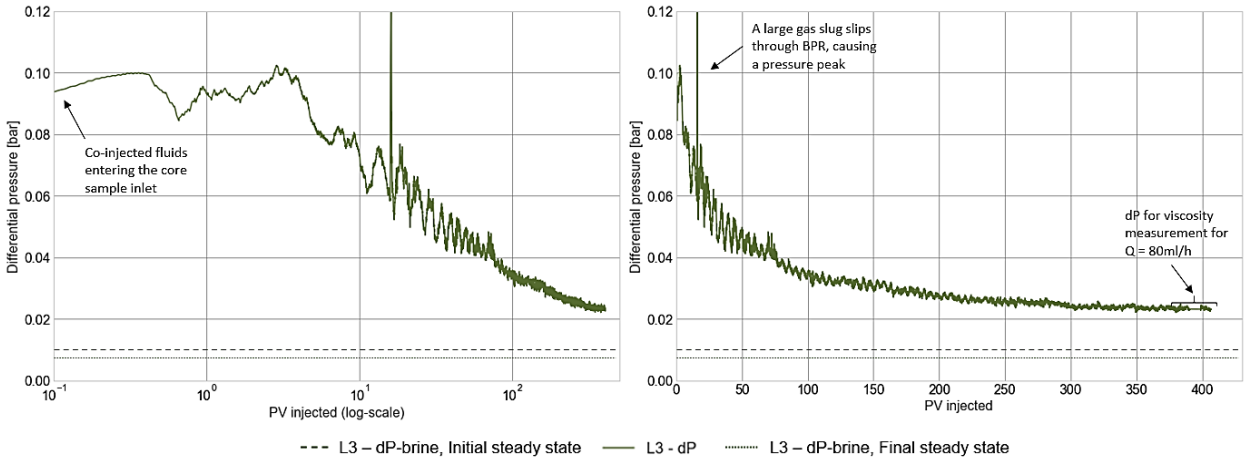

Figure 4.9 – Differential pressure evolution during dissolution in core sample L3. Plots displays the differential pressure during dissolution as a function of pore volume of co-injection. Plot on the left-hand side displays pore volumes of co-injection on a logarithmic scale for acquiring more exact pressure evolution at the start of dissolution. In addition, steady state initial and final differential pressures of brine injection were plotted for volumetric flow rate = 80ml/h.

Figure 4.10 presents pictures of the inlet and outlet end of each core samples, before and after dissolution. Dissolution along the fracture at one side of the core sample was visually observed in all three core samples, i.e., in the already established flow channel made during the fracturing procedure (A). The longitudinal partially open side of the fracture presumably caused a discrimination of reactive fluid flow. The inlet picture for L3 before dissolution shows a preferable flow path to the right side of the fracture, where reactive fluid flow after dissolution in L3, the right partially open side of the fracture seemed to have lost most particles. In the outlet pictures for L2 and L3, only minor changes can be seen, which may explain the small difference in initial and final steady state pressures (injectivity). As mentioned, if the outlet side of the core sample were not affected by dissolution, the measurable bulk injectivity would not be altered significantly.

The differential pressure during dissolution in core sample L1, L2 and L3 had an overall decreasing trend, which indicates dissolution with dissolved particles that were produced from the core sample. During dissolution, white particles were observed in produced effluent from the very beginning and to the end of dissolution. Effluents from L2 and L3, were filtered to separate the white particles, and the particles were sent to the department of Geoscience, UoB for an XRD-analysis. The analysis revealed that the white particles were 100% calcite ($CaCO_3$). Produced calcite shows that a geochemical reaction occurred during co-injection of CO_2 and brine into limestone core samples. The decreasing pressure trend for all three core samples strongly implies that the longitudinal partially open sides of the fracture discriminated the reactive fluid flow. A further decrease towards the end of dissolution indicates changes in geometry of the initial preferable flow path, by increasing the narrowest restrictions, aperture and/or width of the flow channel. The stable pressure trend at the end of experiment indicates no geometry changes in the reactive fluid flow area. Initial preferred flow path that develops to a wormhole could have a positive effect on injectivity, where a dissolution channel at breakthrough increases the injectivity significantly. Injectivity increased for all core samples that had a preexisting preferential flow path, shown by a decrease from initial to final steady state pressures. The pressure trends obtained for L1, L2 and L3 corresponds with former studies (Luhmann et al., 2014; Luquot & Gouze, 2009; Megan M. Smith et al., 2013; Wang et

al., 2016), where the pressure between inlet and outlet of carbonate core samples during carbonic acid injection decreased with time, whereas the injectivity increased by wormhole formation. Formation of a dissolution channel (e.g., wormhole), however, has a negative impact on rock geomechanics.

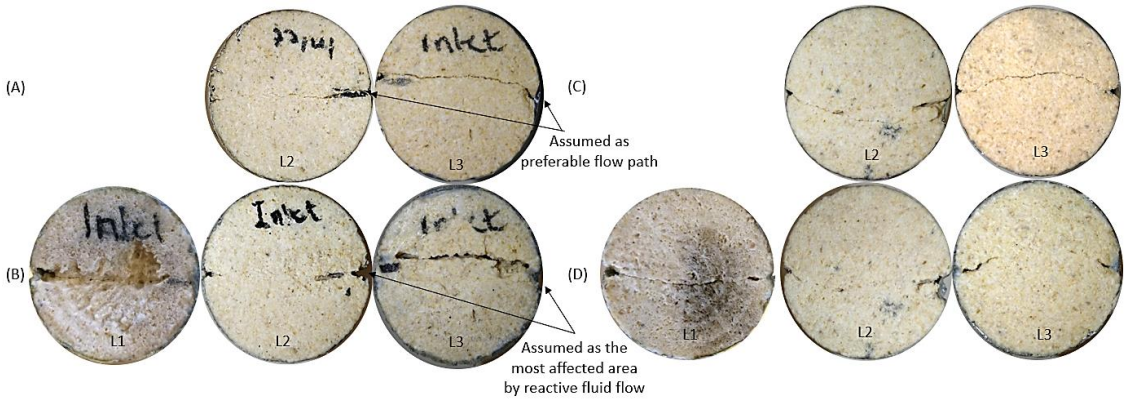

Figure 4.10 – Pictures of (A) core sample inlet before dissolution, (B) core sample inlet after dissolution, (C) core sample outlet before dissolution, and (D) core sample outlet after dissolution. Before pictures for L1 were not obtained.

4.4.2 Dynamic dissolution in tight fractures

Dissolution in L4 by co-injection of CO_2 with brine was performed using parameters found in table 4.3. Figure 4.11 shows the differential pressure evolution during dissolution. From 0PV injected to ~1PV injected, differential pressure showed no fluctuations, which as for L1, L2, and L3 was due to the brine phase passing through BPR. After ~1PV injected to end of dissolution, fluctuations in pressure were present due to a two-phase flow (cyclical) and rock dissolution/blocking of local areas by calcite particles (infrequently). From ~1-9PV no clear pressure trend was observed, but fluctuations with various sizes. Whereas after ~9PV to the end of dissolution, the pressure trend was increasing, with a rapid increase in pressure at ~45PV. An increasing pressure trend might indicate that a two-phase flow in the fracture diverted fluids into the pore network. An increasing pressure could also imply that dissolved calcite particles move within the core sample and clogs the fracture area and parts of the pore network around the fracture. The two dotted arrows shows that the pressure fluctuations increased with increasing pressure and time, which also was an indication of clogged fracture/pore network. Clogging of the pore network or fracture area increases the pore pressure, and hence, the pressure fluctuations. The increase (0.24bars) from initial to final steady state pressure shows a decrease of the injectivity by 427mD. A decrease in injectivity supports the indication of local blocked areas within the pore/fracture network and/or that the co-injected fluids sweep more of the pore network, leaving the pressure to reflect narrow restrictions in the fracture or pore network due to a change in flow path. The increasing pressure trend suggest that the reactive fluid flow was not discriminated within a preferable flow path, particularly. As expected for L4, that had an initial tight fracture.

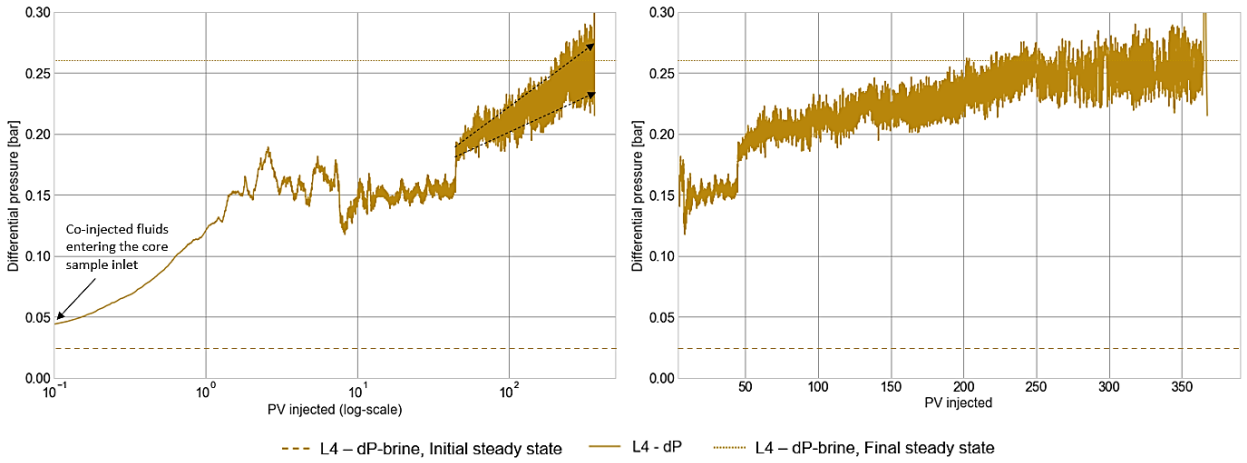

Figure 4.11 – Differential pressure evolution during dissolution in core sample L4. Plots displays the differential pressure during dissolution as a function of pore volume of co-injection. Plot on the left-hand side displays pore volumes of co-injection on a logarithmic scale for acquiring more exact pressure evolution at the start of dissolution. In addition, steady state initial and final differential pressures of brine injection was plotted for volumetric flow rate = 80ml/h.

Dissolution in L5 caused by reactive fluid flow was performed with parameters found in table 4.3. Figure 4.12 shows differential pressure evolution during dissolution. From 0PV to ~0.65PV injected, no fluctuations in pressure were observed, which as previously for L1, L2, L3 and L4 imply that the brine phase was passing through the BPR. After ~1PV, the differential pressure decreases until 9.5PV, with minor fluctuations. From 9.5PV to end of dissolution, fluctuations in pressure start to increase, and from 40PV an increasing pressure trend was observed. Pressure fluctuations as also shown in experiments for L1, L2, L3, and L4, which may appear due to rock dissolution/blocking of local areas by calcite particles (infrequently) through the core sample, or a two-phase flow (cyclical). An overall decreasing pressure trend (L1, L2 and L3), indicates that calcite particles was dissolved and produced from the core sample, whereas an overall increasing trend (L4), indicates that the co-injected fluids sweep more of the pore network around the fracture area and/or that clogging of pores, vugs, and/or local areas of fracture because dissolved particles move within the core sample. The two dotted arrows shows that the pressure fluctuations increased in size with increasing pressure and time, which also was an indication of clogged pore network, as explained in discussion for L4 above. Pressure peaks after ~150PV were large gas slugs slipping through BPR, caused by a damaged inner O-ring in BPR, which was detected after the end of the experiment. The fracture in L5 was characterized as tight. The fracture characteristic may not discriminate the reactive fluid flow particularly, which may cause reactive fluid flow and dissolution around the fracture. Dissolved calcite particles cannot move out of the core unhindered, and e.g., clogs pores, vugs or areas of the fracture. In addition, diversion of flow into the pore network might give an increase in pressure alone. The small increase (0.07bars) from initial to final steady state pressure indicates a decrease in injectivity, where the absolute permeability from initial (38.4mD) to final (25.4mD) decreased with 13mD. This strongly implies clogging of the pore/fracture network during dissolution in core sample L5, and that the reactive fluid flow divers into the pore network outside fracture.

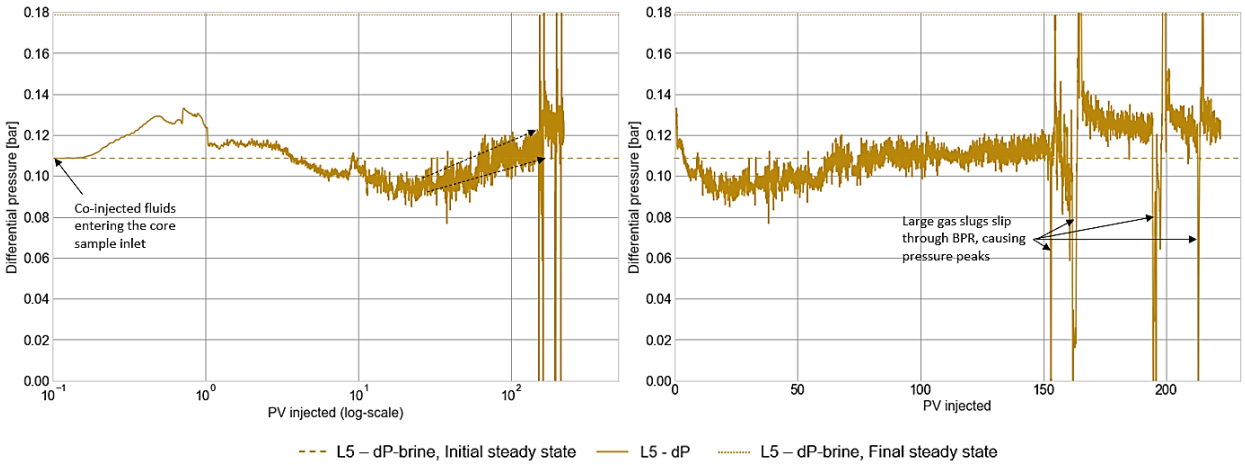

Figure 4.12 – Differential pressure evolution during dissolution in core sample L5. Plots displays the differential pressure during dissolution as a function of pore volume of co-injection. Plot on the left-hand side displays pore volumes of co-injection on a logarithmic scale for acquiring more exact pressure evolution at the start of dissolution. In addition, steady state initial and final differential pressures of brine injection were plotted for volumetric flow rate = 40ml/h.

Figure 4.13 shows pictures of inlet and outlet, before and after dissolution for core sample L4 and L5. The inlet of both core samples shows little to no evidence of a preferable flow path in the fracture area before dissolution. The outlet changed slightly around fracture area during dissolution, and the fracture seems to be clogged at the outlet side after dissolution. Bulk injectivity therefore decreased during co-injection despite obvious dissolution at inlet side.

The differential pressure during dissolution in L4 and L5 had an overall increasing trend that indicates clogging of pore/fracture network due to movement of dissolved calcite particles within the core sample and/or pore network swept by reactive fluid flow. Clogging of pores, vugs and local fracture areas may happen partially, and a total clogging, might explain the rapid pressure increase at ~45PV and ~9PV, for L4 and L5, respectively. The assumed movement of dissolved calcite particles within the core sample, that were not produced, could be supported by the produced effluents, that appeared to contain less calcite particles because the brine production appeared much clearer than observed for L1, L2 and L3. Note that clogging of outlet tubing towards the outlet ESI pressure transducer (see setup in section 3.4.1) could also increase the differential pressure. The fracture characteristic of L4 and L5 may not discriminate a preferred flow path as in experiments with a preexisting wormhole (L1, L2, and L3), which therefore gives an expectation that the reactive fluid flow sweeps more of the pore network, rather than just the fracture network and the already established flow path. The substantial difference in the decreased permeability for L4 (427mD), and L5 (13mD) was presumably caused by the silicone strips (figure 4.6) used in the longitudinal sides of the fracture in L5, which probably caused no flow within the sides of the fracture. Initial permeability for L5 was 38mD, whereas for L4, initial permeability was 463mD.

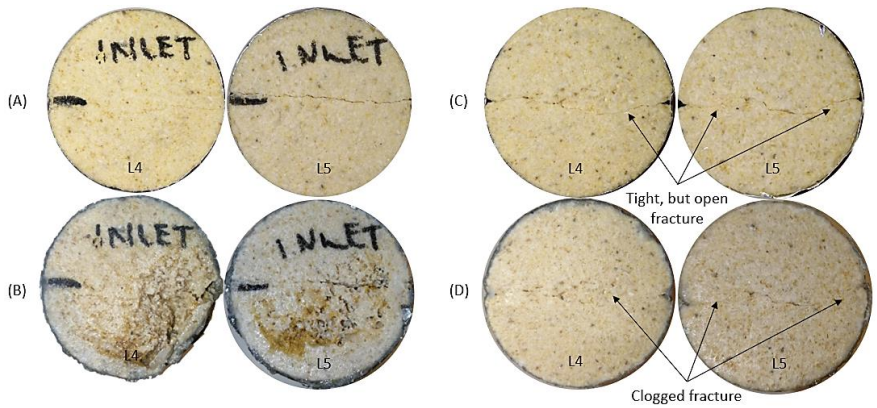

Figure 4.13 – Pictures of (A) core sample inlet before dissolution, (B) core sample inlet after dissolution, (C) core sample outlet before dissolution, and (D) core sample outlet after dissolution.

4.4.3 Apparent viscosity of co-injected brine and CO_2 during dissolution

Apparent viscosity of the co-injected fluids was obtained using steady-state pressure data at the start or end of co-injection experiment and calculated using permeability measurement before and after co-injection where only brine was injected and, presumably, no further changes in pore structure occurred. Equation 2.8 was used to calculate apparent fluid viscosity (section 2.4). Fluid viscosity was further used to calculate an approximation of wormhole aperture, which will further be presented and discussed in section 4.4.4 below.

For experiment L1, fluid viscosity was measured for the lowest flow rate at 20ml/h and calculated using the initial absolute permeability (table 4.3), and the highest flow rate at 160ml/h and calculated using the final absolute permeability (table 4.3). The pressure measurements used, are shown in figure 4.7. The apparent fluid viscosity during injection at 20ml/h was measured to be 3.1cP, whilst at 160ml/h apparent fluid viscosity was 1.19cP. The viscosity at a rate of 40ml/h was calculated with pressure data as shown in figure 4.8 and final permeability from experiment performed on L2 (table 4.3). The viscosity during injection at 40ml/h was measured to be 1.5cP. The apparent viscosity at a rate of 80ml/h was calculated with pressure data as shown in figure 4.9 and the final permeability from experiment L3 (table 4.3). The apparent viscosity during injection at 80ml/h was measured to be 1.2cP. Differential pressures used to calculate apparent fluid viscosity were nearly stable, however, small pressure fluctuations were observed, caused by the effect of the BPR on the system pressure. Similar effect have been observed in previous studies (Skjelsvik, 2018). Uncertainties in calculated apparent fluid viscosity, due to pressure fluctuations is shown in table 4.4.

Two-phase flow likely occurred during co-injection of CO_2 and brine into a water saturated core sample. The apparent viscosity of co-injected fluids was assumed to reflect the viscosity of a liquid solution consisting of two phases. Apparent viscosity for all flow rates used (table 4.4), was greater than viscosity of CO_2 and brine alone, which corresponds well with former studies where CO_2 dissolved in brine resulted in a higher brine viscosity (Islam & Carlson, 2012). In two-phase flow, viscosity plays an important role. Viscosity characterizes the fluids resistance with respect to deformation under shear stress. The lower a fluid's viscosity, the lower its resistance to flow and displacement by another fluid. Therefore, estimations

of fluid viscosity are important, because it can say something about the ability CO_2 or carbonic acid have, to displace each other inside the core sample. Carbonic acid has typically higher density and viscosity than CO_2 itself, therefore, carbonic acid has a great ability to displace CO_2 present in the core sample, and hence cause dissolution.

Table 4.4 – Calculated apparent viscosities using averaged steady state differential pressure either at the end or the start at the experiment, with either initial permeability or final permeability found in table 4.3.

CORE ID	VOLUMETRIC FLOW RATE [ml/h]	FLUID VISCOSITY [cP] CO_2 + BRINE
L1	20	3.10±0.51
L2	40	1.52±0.28
L3	80	1.22±0.14
L1	160	1.19±0.31

L = EDWARDS YELLOW LIMESTONE

4.4.4 Wormhole/fracture characterization from global measurements

Wormhole apertures from global data were obtained and further compared to measurements by in-situ imaging. The purpose of the comparison was to check the plausibility of quantification of dissolution and dissolution patterns (wormholing) by global measurements. Average end-point wormhole aperture was measured by applying Poiseuille's law (eq. 2.7) with the obtained apparent viscosities displayed in table 4.4, differential pressure and the respective volumetric flow rates during dissolution. In addition, average initial and final wormhole aperture was found by steady state differential pressure, brine viscosity and flow rates used to measure permeability before and after dissolution. Endpoint, initial and final wormhole aperture is shown in table 4.5 with uncertainties. Average initial and final hydraulic fracture apertures (table 4.6 with uncertainties) were measured using Buckingham's (eq. 2.9) in the same manner as for Poiseuille's. Buckingham's was used to compare final hydraulic fracture aperture to measurements of average fracture aperture found by micro-CT after dissolution. In addition, used to quantify total initial fracture area before dissolution, which will further be discussed briefly (section 4.5.2).

Table 4.5 – Calculated wormhole apertures from Poiseuille's law.

CORE ID	WORMHOLE APERTURE [mm], POISEUILLE'S LAW, INITIAL (BRINE) ±0.001	WORMHOLE APERTURE [mm], POISEUILLE'S LAW, FINAL (BRINE) ±0.001	END-POINT WORMHOLE APERTURE [mm], POISEUILLE'S LAW (CO-INJECTION)
L1	0.360	0.494	0.42±0.04
L2	0.403	0.420	0.47±0.02
L3	0.414	0.416	0.43±0.02
L4	0.374	0.202	0.23±0.01
L5	0.206	0.186	0.25±0.02

L = EDWARDS YELLOW LIMESTONE

Dynamic development of wormhole aperture is shown in figure 4.14 and 4.15. End-point wormhole apertures obtained by global measurements were averaged from the data displayed in figure 4.14 for L1, L2, and L3, and in figure 4.15 for L4 and L5. The end-point wormhole aperture was calculated to be 0.42mm for L1, 0.47mm for L2, 0.43mm for L3, 0.23mm for L4 and 0.25mm for L5. As seen in figure 4.14 and 4.15 the wormhole aperture was inversely proportional to the differential pressure across the core sample. Higher wormhole apertures were measured for L1, L2, and L3 (average of 0.44mm), than for L4 and L5 (average of 0.24mm). For L1, L2, and L3 a decreasing pressure trend occurred during dissolution, which as indicates that a wormhole increases its narrowest aperture. Calculated initial and final wormhole apertures for L1, L2, and L3 shows that the preexisting wormhole grew with 0.13mm (L1), 0.02mm (L2), and 0.01mm (L3). The growth of the preexisting wormhole inside the longitudinal partially open side of fracture in L1, L2 and L3, decreases the initial low capillary pressure zone (already established flow channel) even more, which results in a decrease in pressure and hence increase reactive fluid (carbonic acid) flow. The discrimination of reactive fluid flow caused dissolution to occur mainly within the wormhole, and therefore continued to increase its aperture. Average end-point wormhole aperture measured for L4, and L5, however, appeared almost as half the size as measured for L1, L2, and L3 and an increasing pressure trend was observed during dissolution (figure 4.15). The final wormhole aperture decreased compared to the initial. This indicates that the preferred flow path got clogged by dissolved calcite particles or that the reactive fluid either changed its preferable flow path during dissolution or due to a lack of preferential flow path. The fracture in L4, and L5 was not initially considered to have an already established flow channel as for L1, L2, and L3. And therefore, a discrimination for reactive fluid flow in L4, and L5 was expected to be less substantial.

Table 4.6 – Calculated hydraulic apertures from Buckingham's (BH).

CORE ID	$\bar{e}_{BH}$ [mm], INITIAL (BRINE) $\pm$0.001	$\bar{e}_{BH}$ [mm], FINAL (BRINE) $\pm$0.001
L1	0.052	0.078
L2	0.059	0.063
L3	0.061	0.062
L4	0.053	0.023
L5	0.024	0.021

L = EDWARDS YELLOW LIMESTONE

Calculated hydraulic apertures by Buckingham's (table 4.6) has the same trend as calculations for wormhole aperture (Poiseuille's), but with a factor of 10 in difference. Since Buckingham's assumes a flow between two separate parallel plates (fracture), measured final hydraulic fracture apertures by Buckingham's for all core samples will be compared and discussed when average fracture aperture found by micro-CT after dissolution is evaluated (section 4.5.3). In addition, initial average hydraulic fracture apertures will be used in discussion regarding quantification of dissolution within fracture area (section 4.5.2). Therefore, are apertures by Buckingham's not discussed further in this section.

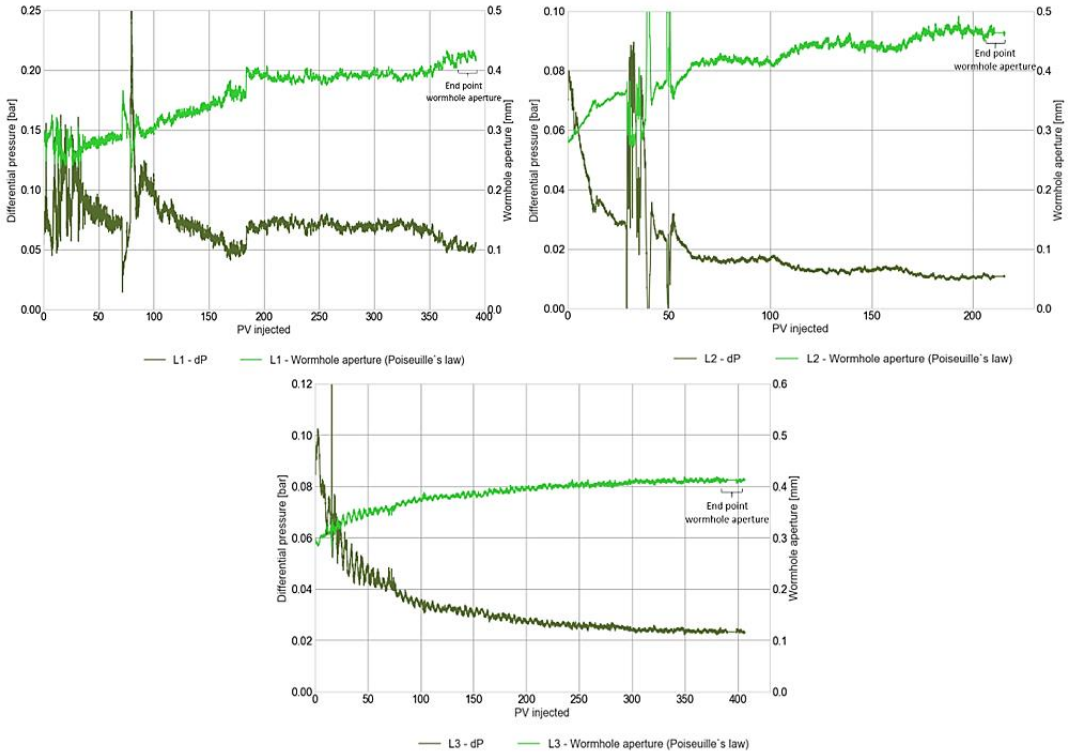

Figure 4.14 – Plots show differential pressure and wormhole aperture as a function of pore volume of co-injection during dissolution experiment for core sample L1, L2, and L3. End-point wormhole aperture is displayed in table 4.5. Note that pressure peaks and hence wormhole aperture peaks are explained in figure 4.7, 4.8 and 4.9, respectively.

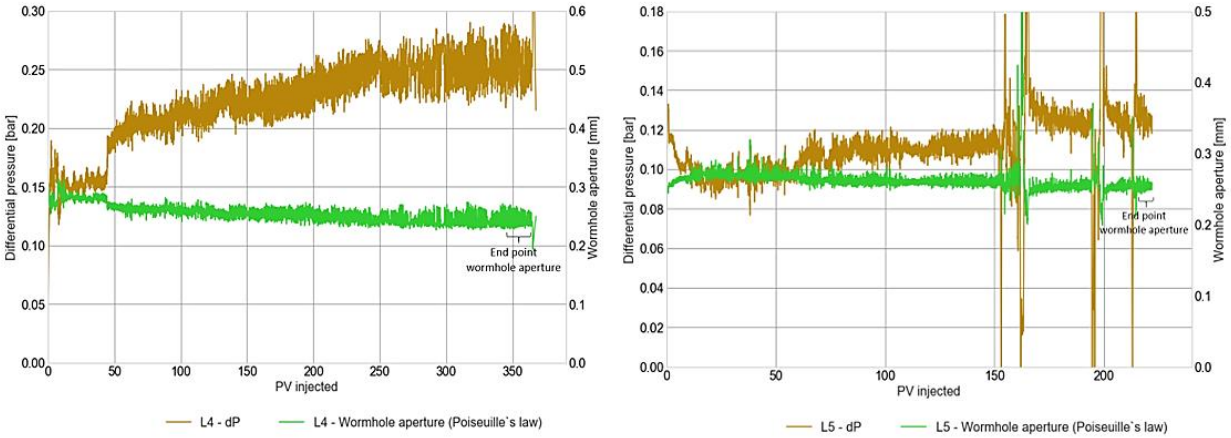

Figure 4.15 – Plots show differential pressure and wormhole aperture as a function of pore volume of co-injection during dissolution experiment for core sample L4, and L5. End-point wormhole aperture is displayed in table 4.5. Note that pressure peaks and hence wormhole aperture peaks are explained in figure 4.11, and 4.12, respectively.

The difference between final wormhole aperture (brine viscosity) and end point wormhole aperture (co-injection viscosity) was mainly due to viscosity differences between the injected fluids, were end-point wormhole apertures were more uncertain than final wormhole aperture measurements. Poiseuille's law assumes pressure drop in an incompressible and Newtonian fluid in laminar flow through a cylindrical conduit with a constant cross section, basically the law describes the pressure drop due to viscosity of the fluid. Due to the assumptions in the law, the wormhole aperture measured during dissolution was

considered as estimated value with a considerable uncertainty. The calculated uncertainties (table 4.5) were mainly impacted by pressure fluctuations caused by the BPR (gas slugs). Major uncertainties not considered when calculating wormhole aperture with Poiseuille's law are e.g., tortuosity and the wall roughness of the dissolution channel/wormhole, or the fracture and fluid flow in pore network outside the wormhole. In addition, a non-Newtonian behavior of co-injection with CO_2 and brine shown by their respective viscosities (table 4.4). Uncertainties of measured average initial and final wormhole aperture by Poiseuille's and hydraulic fracture aperture by Buckingham's were affected by differential pressure, and volumetric flow rate, and appeared as very low. The pressure measurements during five changes in flow rate appeared to have an almost perfect linear trend with $R^2 \approx 1$. A common value of uncertainties for all initial and final wormhole and hydraulic fracture apertures is shown in table 4.5 and 4.6, respectively. Major uncertainties were not considered in calculation for Buckingham's either; like tortuosity and wall roughness of the fracture, and that fluid flow occurs outside fracture, since Buckingham's assumes laminar flow between two smooth, parallel plates, separated by a distance (aperture). Note that both hydraulic aperture by Buckingham's and wormhole aperture by Poiseuille's was measured with confinement pressure. Confinement pressure would cause a compression of the fracture, and therefore a compressed aperture.

4.4.5 Brine pH during dissolution

Geochemical interaction as dissolution of calcite was expected during dissolution by co-injection of CO_2 and Ekofisk brine into limestone core samples at in-situ conditions. pH measurements during dissolution were obtained to see if, and when, a geochemical reaction between carbonic acid and calcite occurred. pH measurements were obtained by an inline pH meter at ambient conditions (see experimental setup and procedure in section 3.4.2), and it was assumed that the initial pH was slightly affected (i.e., less acidic) by the already present calcium in Ekofisk brine. Figure 4.16 represent the pH as a function of pore volumes (PV) of co-injection during dissolution experiment for L2, L3, L4 and L5. pH for Ekofisk brine was obtained before dissolution and average pH was 5.58 (blue dotted line). Average baseline pH for the co-injected fluids (20% Ekofisk brine mixed with 80% CO_2) was measured to be 4.28 ± 0.06 for L2, L3, and L4, while for L5 it was measured to be 5.25. Dissolution experiment for L5 was performed straight after experiment for L4, and calcite precipitation was observed in tubings and BPR. Calcite precipitation in tubings and BPR impacted the pH measurements of the co-injected fluids before experiment L5. Calcite in carbonic acid would naturally try to achieve a chemical equilibrium and therefore make the carbonic acid closer towards a neutral solution. Between every dissolution experiment for L2, L3 and L4, foam experiments were performed in the setup by Aleksandra Soyke from the reservoir physics group at UoB. She observed production of calcite from tubings and BPR during foam experiment, leaving clean tubings and BPR. This may be the reason of the deviation for carbonic acid pH measured in L5 with respect to L2, L3 and L4.

The outlet tubing was flushed with co-injected fluids before injection through the core sample, hence, initial pH (0PV) represented an 80/20 combination of CO_2 and brine and was not descriptive of the fluids flowing through the core. For L2 and L3 an increase in pH was observed after 1.3PV of co-injection, and after approximately 3.6PV of co-injection for L4, and L5. The observed increases in pH for all four experiments were due to a geochemical interaction between calcite and carbonic acid, where an addition

of calcite to the brine resulted in a significant increase in brine pH. The difference between the time of pH increases for L2, L3 and L4, L5, may have a link to the fracture characteristics. pH increased faster in L2 and L3 with preexisting wormhole, and slower in L4 and L5 with tight fracture. Shortly after the increase in pH, stabilized values between 5.52-5.59 for all four core samples were observed. The pH during the 4 days of dissolution never appeared above 6, which corresponds to a former study performed by Steel et al. (2018), where a dissolution experiment was performed over a six month period, and a buffering system was observed. The calcite mixed with carbonic acid buffered the carbonic acid towards a chemical equilibrium and the pH in the former study never increased enough to reach an chemical eqilibrium, and did not go above a pH=6. At pH <6, carbonic acid dominates (Stumm & Morgan, 1995). Therefore, it was assumed in this work that the carbonic acid still contributed to dissolution of calcite in the core samples, despite the increase in pH.

Because pH measurements were performed at ambient conditions, it most likely gave an overestimation of measured pH, where the true pH in the pressurized and heated system presumably was more acidic. When the co-injected fluids were depressurized from in-situ conditions to ambient conditions, CO_2 transform to gas. The measured pH reflects the pH of brine with a minor degree of dissolved CO_2, giving a less acidic solution. The pH of carbonic acid under in-situ conditions is normally around 3 (Snippe et al., 2020). pH measurements in this work indicates a geochemical reaction between calcite and carbonic acid, where calcite buffers the carbonic acid from a pH of approximately 4.28 to 5.5 in possibly overestimated values. The geochemical reaction occurs shortly after introduction of the carbonic acid to the limestone core samples.

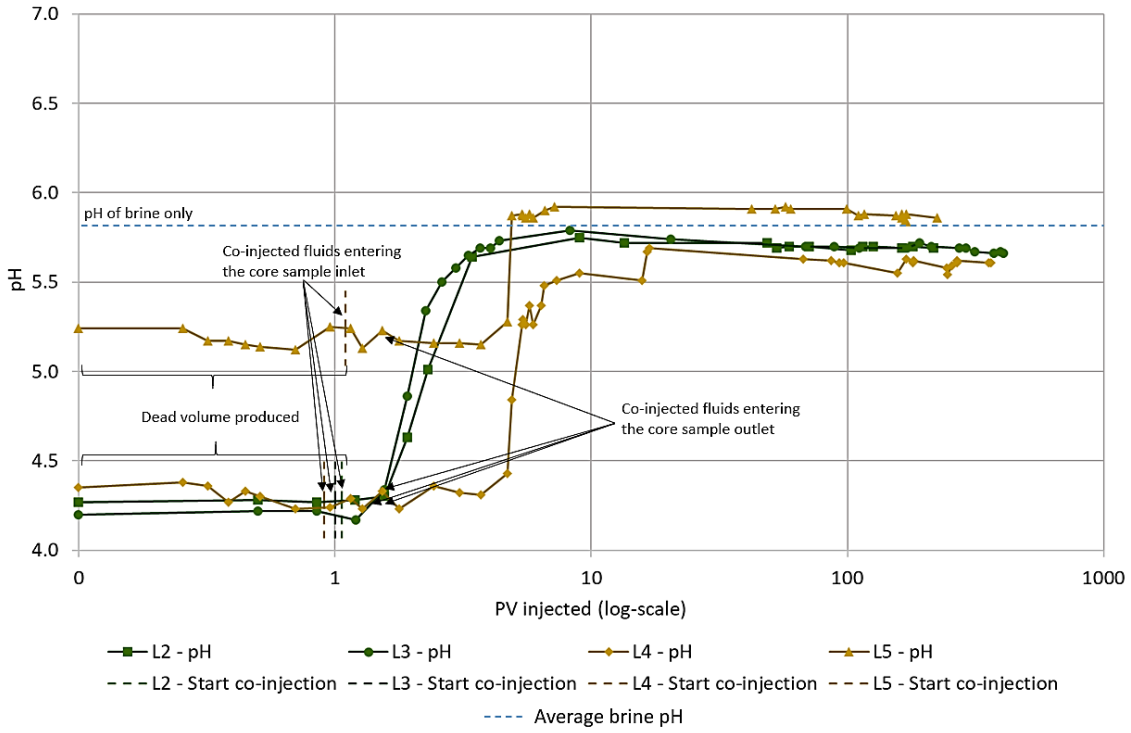

Figure 4.16 – pH evolution during dissolution. Plot displays pH as a function of pore volume of co-injection. In addition, an average pH of Ekofisk brine.

4.4.6 Important observations during dissolution

Several important observations were obtained during dissolution of Edward yellow limestone by co-injection of CO_2 and brine:

- An overall decreasing pressure trend was observed for core sample L1, L2 and L3, and indicated that the reactive fluid flow mainly occurred in the partially open sides of the fracture. An initial preferable flow path discriminates dissolution and may facilitate further wormholing.
- Injectivity increased during co-injection in cores with a preexisting wormhole (L1, L2, and L3), visible in a decrease from initial steady state pressures to final. A more substantial decrease was observed for L1, in comparison to L2, and L3 which strongly indicate that the partially open side of fracture in L1 discriminated the reactive fluid more than in L2, and L3. However, the minor decrease from initial to final steady state pressure for L2, and L3 may indicate that the reactive fluid flow occurred within other areas within the fracture and pore network around the fracture.
- The overall increasing pressure trend during dissolution for L4 and L5 (tight fracture) indicated no discrimination of a preferred flow path, which therefore gives an expectation that the reactive fluid flow sweeps the entire fracture area. In addition, clogging of pore/fracture network was suggested as a reason for the increasing pressure trend. Clogging would negatively impact the injectivity of CO_2 and CO_2 storage potential but could increase the CO_2 storage security by limiting migration of CO_2. Improved sweep efficiency increases the CO_2 storage potential and decreases the probability of wormhole development (positive for the geomechanics stability of carbonate rock).
- An increase from initial to final steady state pressures for L4, and L5 was obtained, which strongly indicated that the bulk injectivity had decreased during dissolution.
- Viscosity of CO_2/brine mix appeared to be shear thinning.
- Initial and final wormhole apertures for L1, L2, and L3 showed that preexisting wormhole grew during dissolution, whereas for L4, and L5 with tight fracture, wormhole aperture decreased. End-point and final wormhole aperture obtained from global measurements showed that L1, L2, and L3 had a wider flow path, than L4, and L5 after dissolution. End-point and final wormhole aperture for L1, L2 and L3 was approximately twice as wide as in L4, and L5.
- The brine pH during dissolution was buffered by calcite particles to a chemical equilibrium, due to a geochemical interaction between CO_2, brine, and calcite. The pH was buffered with an approximate increase of 1.22. The increase in pH strongly suggests that a geochemical reaction between carbonic acid and calcite occurred.

4.5 In-situ quantification of dissolution after co-injection

PET/CT imaging was used to quantify changes in pore/fracture network and reactive fluid flow due to dissolution of calcite during co-injection of CO_2 and brine. Table 4.7 shows the different imaging techniques and modalities performed before and after dissolution for the five limestone core samples. Micro-CT images were examined using image analysis software ImageJ FIJI, preclinical PET/CT-images (high resolution) and clinical PET/CT-images were examined using image analysis software InterviewFusion.

Table 4.7 – Imaging techniques and modalities applied on core sample L1, L2, L3, L4, and L5.

CORE ID	PET/CT MODALITIES -INITIAL	PET/CT MODALITIES -FINAL
L1	Micro-CT	Micro-CT + Preclinical PET/CT
L2	Micro-CT	Preclinical CT
L3	Micro-CT	Micro-CT + Preclinical PET/CT + clinical PET/CT
L4	Micro-CT	-
L5	Micro-CT	Micro-CT

L = EDWARDS YELLOW LIMESTONE

4.5.1 Visual characterization of dissolution patterns by micro-CT images

Dissolution patterns developed during co-injection were evaluated by micro-CT images. Micro-CT images for L1, L3, and L5 after dissolution were taken under consideration. Figure 4.17 (for L1), figure 4.18 (for L3) and figure 4.19 (for L5) shows a selection of axial, coronal and sagittal cross sections. Based on the inlet side for sagittal and coronal cross sections, all three core samples show the tendency towards compact conical dissolution at inlet side, with a dominant wormhole that extends over the unit length of core sample L1 and L3. Whereas for L5, a main wormhole reaches only ∼13.5mm into the core sample. Development of wormholes was enacted to initial heterogeneities of the fracture (Yang et al., 2020). L1, and L3 had initial fracture characterized as tight with longitudinal partially open side of the fracture, which resulted in wormhole formation in one side along the whole unit length of the core sample. L5, however, had an initial fracture characterized as tight through the whole core sample, which resulted in a main wormhole within the fracture (longest wormhole), with several small wormholes outside the fracture area. The main wormhole did not extend over the unit length of the core sample. Development of wormholes in L1, and L3 reveals that the reactive fluid preferred to flow within the already established flow channel (longitudinal partially open sides of fracture) as expected. Development of dissolution patterns were strongly affected by the initial heterogeneities within the fracture as shown for L1 and L3. In addition, dissolution patterns were dependent of the injection rate: co-injection in L1 was performed with four flow rates, where the highest was 160ml/h, and resulted in a compact conical dissolution at inlet with a conduit-like-wormhole. In L3 the flow rate was 80ml/h and formed a wormhole-like dissolution, but with compact conical dissolution at inlet. L5 was performed with a flow rate of 40ml/h, which resulted in compact conical dissolution with development of small wormholes. Former studies (Luhmann et al., 2014; Ott & Oedai, 2015; Snippe et al., 2020) described in section 2.2.5 showed that dissolution in whole carbonate core samples during co-injection at flow rates from 20-70ml/h formed compact dissolution at the inlet side, whereas flow rates >70ml/h transitioned from compact dissolution to wormholes with time. Dissolution in the fractured core samples in this thesis with approximately the same injection rate

regimes, showed that compact conical dissolution occurs at inlet side for fractured core samples as well. However, wormhole formation through the whole unit length of core sample L1 and L3 as an addition to compact conical dissolution deviates from the former study. The extend of the wormholes reveals that the reactive fluid flow was discriminated in the high permeability area (longitudinal partially open sides of the fracture) in L1 and L3. Whereas for L5 (tight fracture), the fracture was only slightly more permeable than the pore network and the main wormhole did not extend though the core sample. As seen in the axial cross sections close to the inlet side, slightly more dissolution occurred in lower parts of the fracture and the cross section. More dissolution in lower parts of the fracture was expected due to gravitational effects, because of density differences in the two-phase flow. Where $\rho_{\text{Carbonic acid}} > \rho_{\text{Brine}} > \rho_{CO_2}$. On field scale, compact conical dissolution at inlet side can be a threat against the well integrity, whilst wormholes and fractures can have a positively effect for the injectivity of CO_2, but a negatively effect on CO_2 storage potential.

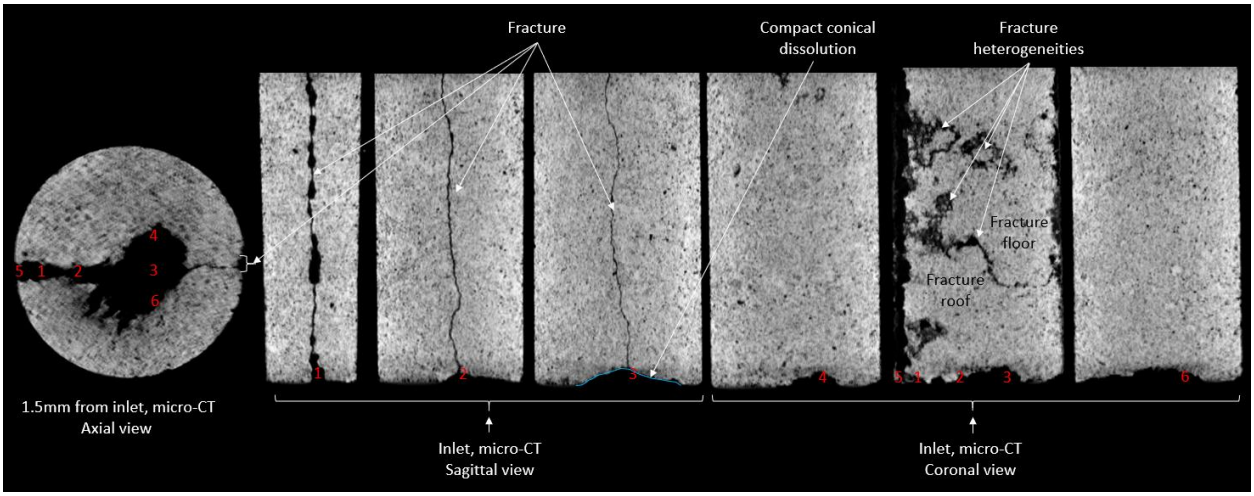

Figure 4.17 – Axial, sagittal, and coronal micro-CT cross sections of core sample L1. The position of the axial cross section corresponds to sagittal and coronal cross sections. Fracture heterogeneities is referred to when both the fracture roof and fracture floor is present in the cross-section image.

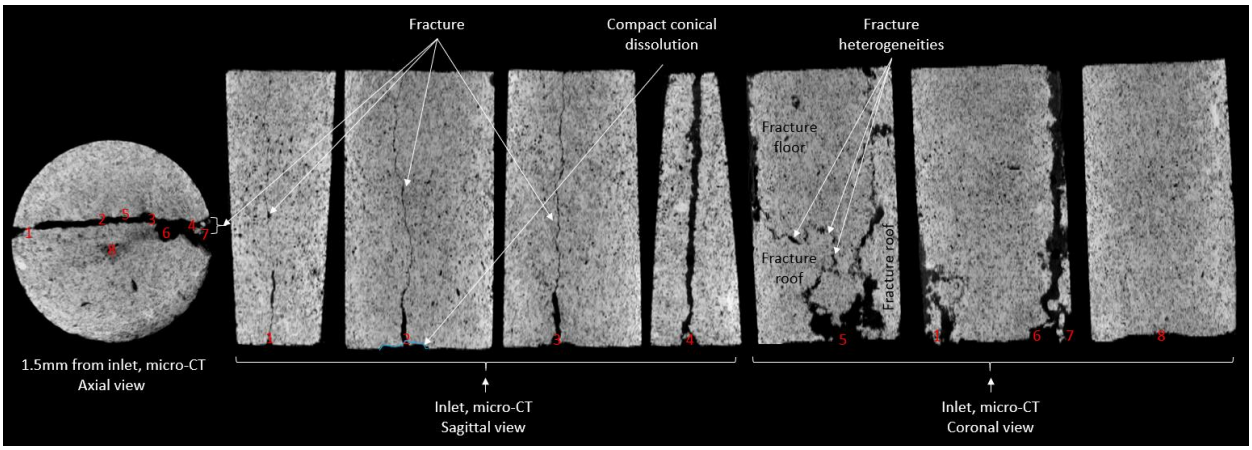

Figure 4.18 – Axial, sagittal, and coronal micro-CT cross sections of core sample L3. The position of the axial cross section corresponds to sagittal and coronal cross sections. Fracture heterogeneities is referred to when both the fracture roof and fracture floor is present in the cross-section image.

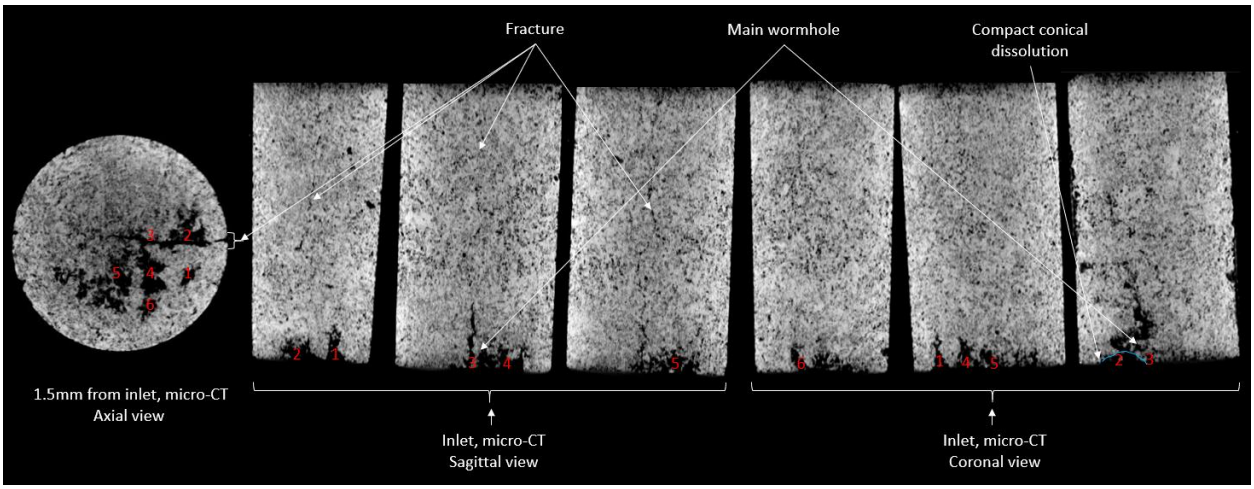

Figure 4.19 – Axial, sagittal, and coronal micro-CT cross sections of core sample L5. The position of the axial cross section corresponds to sagittal and coronal cross sections. Fracture heterogeneities is referred to when both the fracture roof and fracture floor is present in the cross-section image.

4.5.2 Quantification of dissolution by micro-CT images

Absolute porosity was measured from cross sections in micro-CT images for core sample L1, L3 and L5. The purpose of evaluating absolute porosity before and after co-injection was to quantify where most of the dissolution had occurred in the core sample. Absolute porosity during co-injection of CO_2 and brine into fractured limestone core samples was expected to change. Especially, a substantial change in porosity due to a discriminations of reactive fluid flow which results in local dissolution within fracture area. For quantification of dissolution, core samples were scanned by micro-CT before (initial) and after (final) dissolution experiments. Initial and final absolute porosity were measured both for whole cross sections and in region of interest around fracture area. The method for finding absolute porosity from micro-CT images is shown in figure 4.20. The figure illustrates an axial cross section after fracturing and co-injection, in addition, a 3D cylindrical core sample. The micro-CT image of the core sample was divided into slices, with approximately 1.5mm between each cross section, using image analysis software ImageJ FIJI. Thereafter a line tool in FIJI was used to calibrate the scale of the images, using the known core sample diameter. The brightness and contrast of the image was adjusted mainly to remove noise around the core sample, before thresholding of the image was applied to transform to a binary format where black color represent pores, vugs and fracture and white color was matrix. The fraction area of black color corresponds to the absolute porosity. An example of transition from grayscale to binary image is displayed in figure 4.21. The combined void space before and after dissolution was measured both for the whole cross sections through the core sample, and around fracture area, displayed as red boxes (ROI) in figure 4.20. The ROI was placed manually at the inlet, outlet, and middle cross section, and interpolated for all cross sections by a function in FIJI. Positioning the ROI boxes on initial images (without fracture) were controlled as demonstrated in figure 3.5. Initial and final absolute porosity was measured three times, respectively, where adjustment of brightness and contrast, and thresholding were performed each time. The three combined void space measurements had the purpose to show uncertainties in thresholded images. Thresholding can deviate each time, due to a visual interpretation of the pore space, which is

highly uncertain. In addition, beam hardening (shown as more white areas of the outer edge in the grayscale image (figure 4.21)) may affect the measurement of combined void space, because pores may not appear as black color along the edge. The most influential factor was the quality of micro-CT images. Spatial resolution for micro-CT images was around 29-30µm, which was an ideal resolution for capturing most of the pores, vugs and fracture. But the quality of the images was also dependent on a stable micro-CT scan, which involves no movement or vibrations near the CT-scanner during scanning. Vibrations can cause the core sample to move just slightly under a CT-scan and affect the reconstructed image by making it blurry. In addition, the number of projections can contribute to make the image clearer or blurrier. A small number of projections makes the image blurrier, whereas a higher number of projections makes the image clearer. But a higher number of projections makes the scanning time much longer. Micro-CT images were slightly blurry due to small observed movements of the core sample while rotating on the rotation device during micro-CT scanning. The blurry quality of the images makes the thresholding difficult, because there are less sharp edges between the grayscale colors in the image. Quantification of absolute porosity before and after dissolution is influenced by these factors.

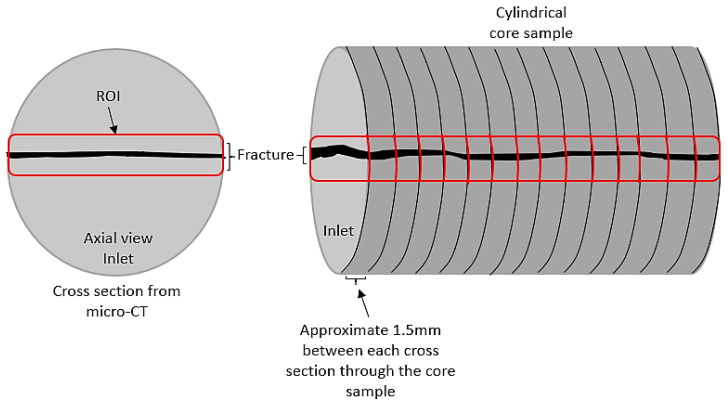

Figure 4.20 – Figure displays method for measuring changes in absolute porosity in the whole axial cross sections from micro-CT scans before and after fracturing and dissolution. In addition, absolute porosity was measured within ROI displayed as red boxes.

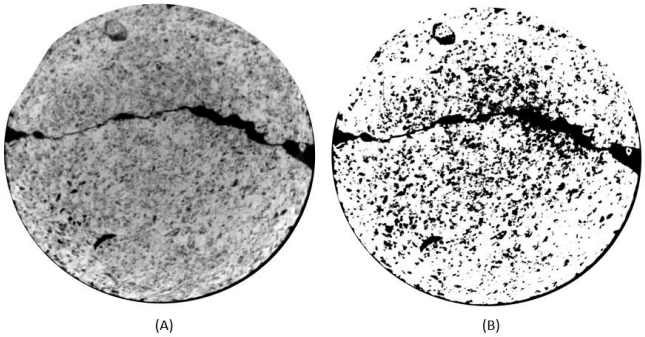

Figure 4.21 – Axial cross section of a micro-CT image after dissolution in L3, where (A) is an 8-bit grayscale image with adjusted brightness and contrast, and (B) is a binary image.

Figure 4.22 displays the measured absolute porosity before (dotted line) and after (whole line) dissolution for whole cross section (yellow) and within ROI (green) for core sample L1. The absolute porosity is presented as a function of length, from the inlet to the outlet side of the core sample. The uncertainties due to thresholding are displayed as error bars in the plot. From 0mm (inlet) to ~34mm an average increase in absolute porosity of the whole cross section was 4%, whereas within the ROI an increase was 12%. From ~34-72mm no significant increase in absolute porosity was observed for the whole cross sections, but around the fracture there was an increase of 4%. The minor changes (0-4%) in absolute porosity shows that the bulk matrix dissolution due to co-injection of CO_2 and brine in a fractured core sample was minor. However, dissolution in and around fracture area was substantial, where porosity increased with ~12%. This was expected due to a discrimination of reactive fluid flow in the fracture ($P_{c,fracture} < P_{c,pores}$). Most of the porosity changes occurred from the inlet side and towards outlet porosity changes decreases, which is supported by inserts of micro-CT cross sections. At ~1.5mm from inlet, inserts show that a substantial dissolution occurred around the fracture area, giving ~25% increase of porosity. Whilst for inserts at ~62mm shows a minor increase of ~2%. The fracture itself, before dissolution must have affected the increase in porosity. Due to the lack of micro-CT images before dissolution with fracture, initial fracture aperture found by Buckingham's (table 4.6) with known core sample diameter was used to estimate the total fracture area within a cross section. The total fracture area was 0.17%, which is an approximated value with several simplified assumptions (section 2.4). The approximated fracture area indicated that initial fracture contributed just slightly to a porosity increase.

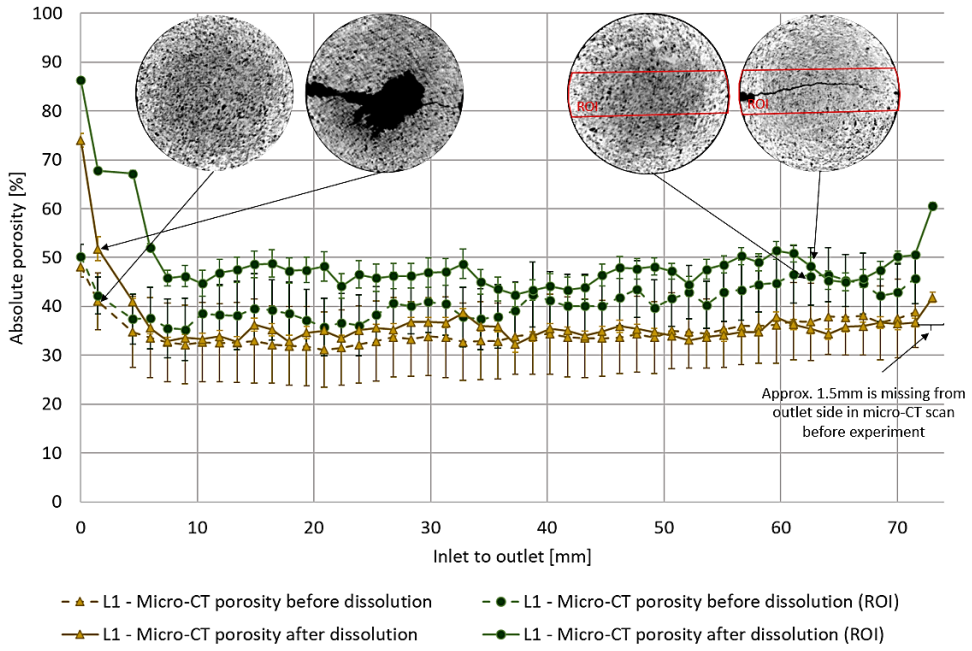

Figure 4.22 – Plot displays absolute porosity conducted from binary micro-CT images, before and after fracturing and dissolution, from whole cross sections and within ROI for L1. Note that the image before dissolution missed approximately 1.55mm of the outlet, caused by the positioning of the detector wall during micro-CT scanning.

Figure 4.23 displays the measured absolute porosity for L3. From 0mm (inlet) to ~21mm an average increase in absolute porosity of the whole cross section was 5%, whereas within the ROI an increase was 14%. From ~21-63mm the increase in absolute porosity for the whole cross sections was 4.5%, whereas within ROI the increase was 5%. The minor change (4.5-5%) in absolute porosity for whole cross sections shows that dissolution only impacted the bulk porosity slightly, as also seen for L1 above. Within fracture area, the increase of 14% show the same as for L1, where the changes of absolute porosity were more substantial. Indicating that most dissolution occurred within the fracture. In addition, most of the porosity changes occur from the inlet side and with length porosity changes decrease. Cross section inserts in figure 4.23, visually supports the ~10% increase of porosity near the fracture area at ~12mm from the inlet side. And inserts at ~61mm from inlet side supports lower increase of ~5% in porosity. As for L1 above, lack of micro-CT images before dissolution with fracture resulted in approximated initial fracture area, calculated from apertures found by Buckingham's (table 4.6) and with known core sample diameter, the total fracture area was 0.2%. The approximated fracture area indicated that initial fracture contributed just slightly to a porosity increase.

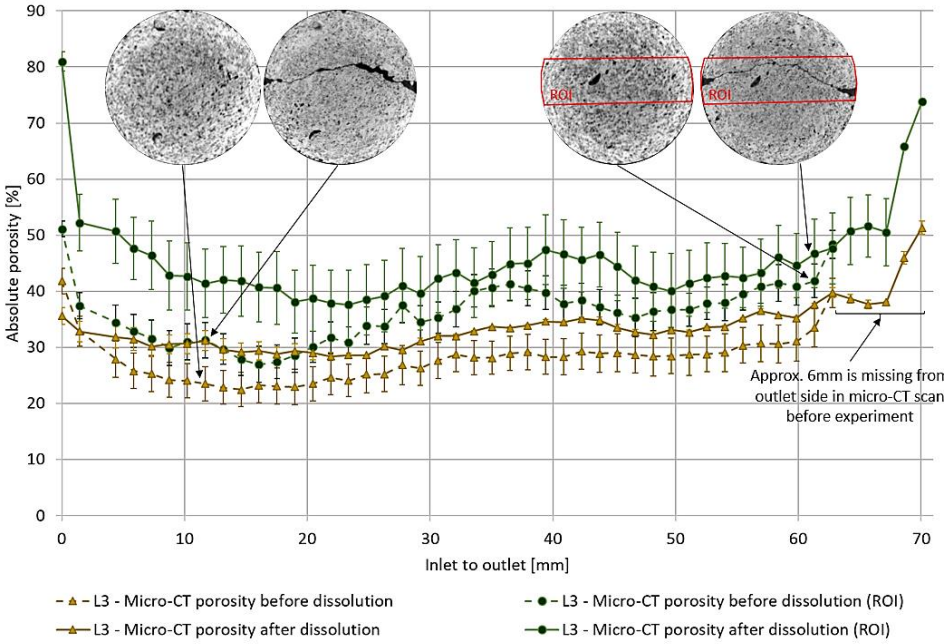

Figure 4.23 – Plot displays absolute porosity conducted from binary micro-CT images, before and after fracturing and dissolution, from whole cross sections and within fracture area (ROI) for L3. Note that the before image was missing approximately 6mm of the outlet, caused by the positioning of the detector wall during micro-CT scanning.

Figure 4.24 displays the measured absolute porosity for L5. From 0mm (inlet) to ~6mm an average increase in absolute porosity of the whole cross sections was 5%, whereas within fracture area an increase of 12% was found. From ~6-64mm a decrease in absolute porosity of ~1.2% for the whole cross sections was obtained, whereas within fracture area, an average increase in absolute porosity was ~0.2%. At outlet side from approximately 64-67mm an increase of porosity for the whole cross sections was ~13%, and within fracture the increase was ~18%. The sudden increase in porosity at outlet side, may possibly be due to an easier production of dissolved calcite particles. At outlet side dissolved particles can be directly produced to the outlet tubing. However, dissolved particles from porosity increase (12%) within fracture

area at inlet side, was assumed to move within the fracture area towards outlet. The minor increase of porosity (~0.2%) at fracture area towards outlet (~6-64mm) indicates either: that dissolved particles from inlet side was left behind in already dissolved areas of the fracture (clogging) or that minor dissolution occurred. With the observed increasing pressure trend as discussed in section 4.4.2, with a fracture initially characterized as tight, reactive fluid flow was assumed to divert into the pore network surrounding the fracture. The inserts shown in figure 4.24 (near inlet) reveals that dissolution occurred outside fracture area. As measured for L1 and L3: L5 had an initial fracture area of 0.08%, which indicated that initial fracture contributed marginally to a porosity increase.

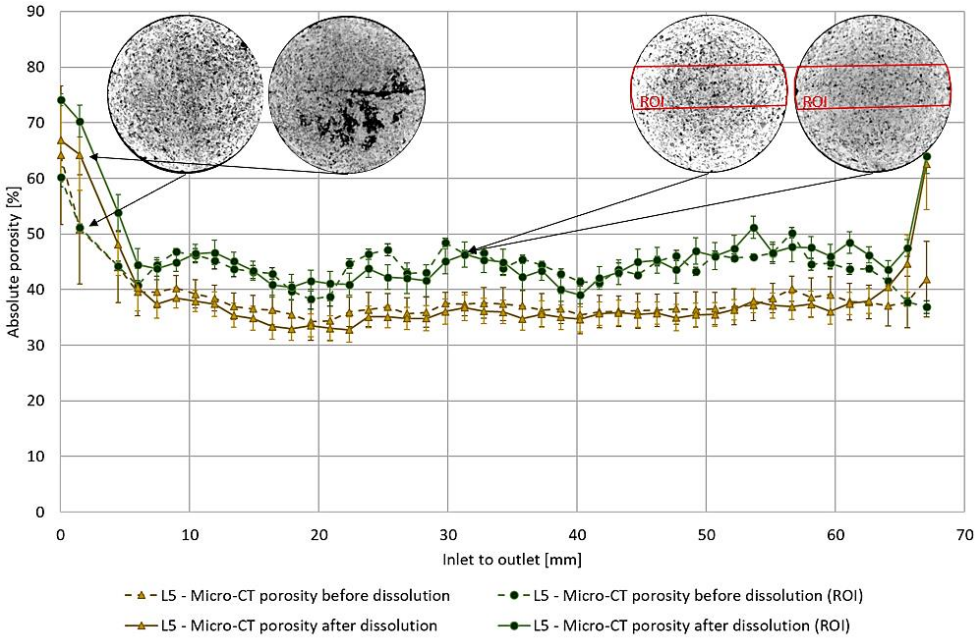

Figure 4.24 – Plot displays absolute porosity conducted from binary micro-CT images, before and after fracturing and dissolution, from whole cross sections and within fracture area (ROI) for L5.

Figure 4.25 shows dissolution around fracture area as a function of normalized core sample length (from inlet to outlet) for core sample L1, L3, and L5. Overall, for all three core samples more than 10% of the core material was dissolved within the first fracture increment (=0.07) during co-injection, showing that most of the dissolution occurred close to the inlet side. The dissolution trend at inlet side corresponds well with former similar studies by (Yang et al., 2020). From fracture increment 0.14-1 of the core samples, L1 and L3 shows more dissolution (~6% and ~6.5%, respectively) than L5 (~1%). L1, and L3 has a similar dissolution trend where dissolution was higher towards inlet and decreased towards outlet (see trend lines for L1, and L3). For L5, the overall dissolution trend was nearly flat (see trend line for L5). The different dissolution trends could be coupled to the initial fracture system, where for L1, and L3 a preferential flow path was established before dissolution with a substantial conductivity, causing the reactive fluid flow to be concentrated in the flow path, and hence dissolve that area. In addition, a wider fracture aperture in the partially open longitudinal sides of the fracture promotes a production of dissolved particles. The discrimination of reactive fluid flow, and hence dissolution within the fracture caused a substantial increase of porosity in fracture area for core sample L1 and L3, whereas the surrounding area showed little change in porosity. This corresponds with a former similar study by (Yang

et al., 2020) (section 2.2.3). Whereas, for L5, with an initial fracture characterized as tight, production of dissolved particles through the fracture was inhibited, and therefore cause clogging of local areas of the fracture. In addition, a tight fracture could promote dissolution in other areas than the fracture, due to diversion of reactive fluid flow.

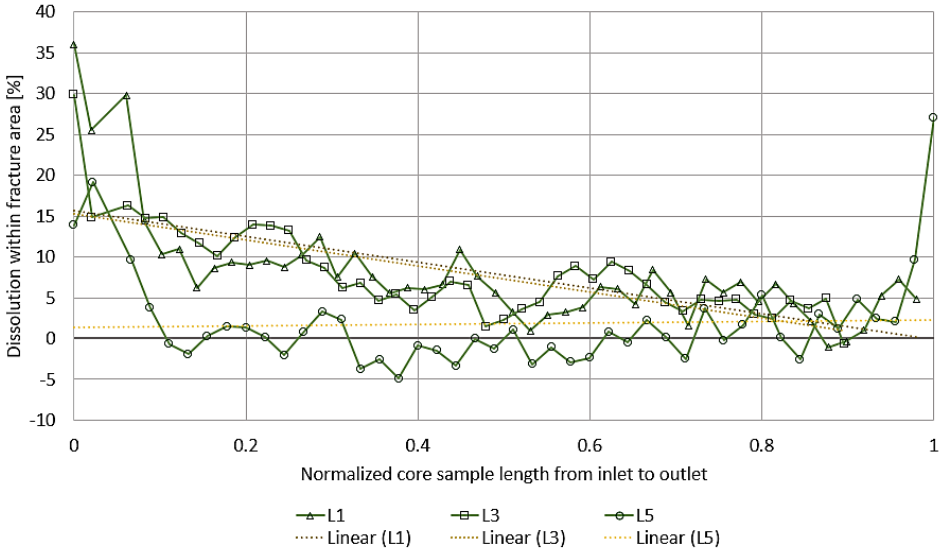

Figure 4.25 – Plot displays dissolution within fracture area (ROI) for core sample L1, L3, and L5. Note that parts of outlet in micro-CT images before dissolution for L1, and L3 was missing.

4.5.3 Quantification of fracture aperture by micro-CT

An average fracture aperture after dissolution was found by micro-CT images for L1, L3, and L5 for comparison of calculated final hydraulic aperture by Buckingham's using global data (section 4.4.4). Figure 4.26 demonstrates how average fracture aperture (micro-CT) was obtained using ImageJ FIJI. The micro-CT image of the core sample was divided in slices with approx. 1.5mm between each cross section. Vertical fracture apertures (white arrows in axial cross section) were manually measured by a line tool in FIJI for each slice through the core sample and averaged.

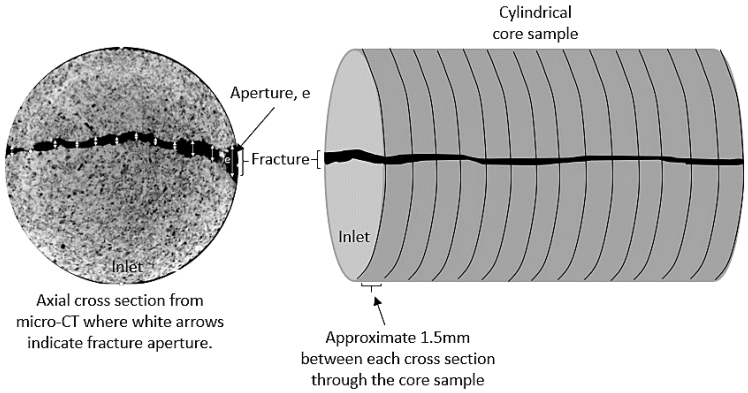

Figure 4.26 – Figure displays method for measuring average fracture aperture by micro-CT image.

Average fracture aperture from micro-CT images is displayed in table 4.8, with final hydraulic fracture aperture from Buckingham's. Average fracture aperture by micro-CT for L1, and L3 was 0.68mm and 0.72mm, respectively. For L5, a smaller aperture of 0.28mm was found. From Buckingham's using global data, final hydraulic apertures for L1 and L3, was 0.078mm and 0.062mm, respectively. For L5, a smaller final hydraulic aperture of 0.0208mm was found. Overall, for all three core samples, hydraulic apertures by Buckingham's were a factor of 10 smaller than the average fracture apertures from micro-CT. Therefore, using Buckingham's for estimating the narrowest restriction within the fracture was not suitable when a wormhole (L1, and L3) is present, and where fluid flow is assumed to divert into the pore network outside the fracture (L4, and L5). In addition, several uncertainties (section 4.4.4) due to the assumptions in Buckingham's is present.

Table 4.8 – Measured average fracture apertures from micro-CT images and average final hydraulic fracture apertures by Buckingham's.

CORE ID	$\bar{e}_{BH}$ [mm] - FINAL (BRINE) $\pm$0.001	$\bar{e}_{Micro-CT}$ [mm] - FINAL
L1	0.078	0.68$\pm$0.06
L2	0.063	NM
L3	0.062	0.72$\pm$0.06
L4	0.023	NM
L5	0.021	0.28$\pm$0.02

L = EDWARDS YELLOW LIMESTONE

4.5.4 Quantification of preferential flow paths by PET and CT images combined

Fracture and wormhole characteristics as average and maximum fracture aperture, maximum wormhole aperture and volume of wormhole have been examined by using PET/CT images. The maximum wormhole apertures were compared to the wormhole apertures found using global data with Poiseuille's law. The purpose of investigation of wormhole and reactive fluid flow by applying imaging techniques was to evaluate the plausibility of using global data for quantifying wormhole/dissolution propagation during co-injection of CO_2 and brine in limestone core samples.

The aperture of wormhole for L1, L2, L3, and L5 was evaluated, in addition volume of wormhole and dissolution was obtained for L1, and L3, by using different imaging techniques. Aperture and volume of wormholes through polymer gel have previously been measured by PET-images by Bergit Brattekås et al. (2017). In this thesis a similar approach of the method as used in the previous study was used for measuring aperture and volume. The method for finding maximum wormhole aperture, and volume by PET/CT is displayed in figure 4.27. The figure illustrates an axial cross section after fracturing and dissolution, in addition, a 3D cylindrical core sample. PET/CT images were divided into several cross sections, with approximately 1.5mm between each cross section. A line tool in FIJI was used to calibrate the scale of the images, using known core sample diameter. A line tool in ImageJ FIJI was used to examine wormhole apertures and widths for CT-images, while a line tool in InterviewFusion was used for PET-images. Measurements of maximum fracture aperture was found by measuring three apertures (whole line arrows) within the wormhole where the maximum aperture was filtered out and evaluated. Three

apertures with three widths (dotted line arrows) within the wormhole was found for calculating an average volume of the wormhole. Note that for PET images, aperture and width was found by measuring the PET-signal only, which corresponds to fluid distribution.

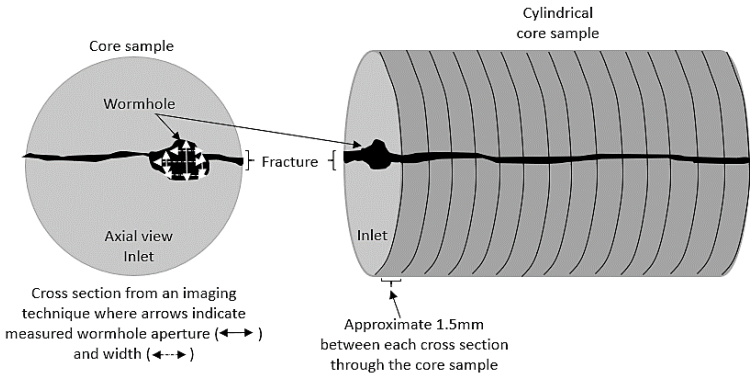

Figure 4.27 – Method for measuring maximum wormhole aperture and wormhole volume from the different imaging techniques.

Figures 4.28, 4.29, 4.30, and 4.31 show plots of maximum apertures as a function of core sample length, from inlet to outlet side. Maximum apertures were obtained from the respective imaging techniques for core sample L1 (figure 4.28), L2 (figure 4.29), L3 (figure 4.30) and L5 (figure 4.31). The plots also include maximum aperture found during measurements of average fracture aperture (grey line with triangle), end point wormhole aperture by Poiseuille's law calculated from global data (lime green line) and inserts of axial cross sections from imaging techniques.

For L1, maximum aperture from all the imaging techniques and modalities applied, follows the approximate same trend and values. Except measured maximum aperture from PET-images close to outlet side, which shows larger measured aperture. Average max. aperture by PET from 62mm to outlet of the core sample was measured to be 4.7mm, and by CT average max. aperture was 2.12mm. Larger measured apertures from PET-images can be explained by that the apertures were measured from the PET-signal. The PET-signal corresponds to tracer distribution within the core, and therefore may the increase in aperture at outlet side be due to fluid flow in areas around the wormhole, e.g., within the fracture and other low capillary pressure areas. This can indicate that dissolution occurred in areas close to the outlet that could not be determined by CT. From inlet to 62mm of the core sample average max. aperture by PET (2.5mm) was approximately the same as by CT (2.8mm). Generally, measured average max. aperture from preclinical PET increased with time, where flow rate of 160ml/h were used at the beginning of the PET-scan, while 32ml/h, and 160ml/h #2 followed. The apertures for flow rates were, 2.35mm, 3.17mm and 3.3mm, respectively. Diffusion of convective flow (traceable brine) with time during PET-scan might explain the larger measured apertures during injection at 160ml/h (start of PET-scan) than 160ml/h #2 (end of PET-scan). Diffusion makes the traceable brine appear in larger areas as PET-signal, and hence larger wormhole apertures were measured. Diffusion might be both flow rate and time dependent, which indicates that apertures measured form PET-images obtained at the end of a PET-scan (160ml/h #2) gives a more accurate description of the aperture that is affected by the reactive fluid flow. The inserts shown in figure 4.28 represent the core length which the arrow indicates. Visually, one can see that at the inlet side (~1.5mm from the inlet) of the core sample larger apertures were found,

compared to ~9mm and ~65mm into the core sample. The end point wormhole aperture measured from global data for L1 was 0.42mm, while the average wormhole aperture found from imaging techniques from inlet to outlet side was 2.82mm. All PET/CT images, except micro-CT images were performed with approximately 12bars confinement pressure. Wormhole aperture found by Poiseuille's law, using global data, was also obtained with 12bars confinement pressure. However, the measured maximum aperture from micro-CT corresponded well with measured apertures from preclinical PET/CT, which indicates that the compression of the fracture from the confinement pressure was insignificant when investigating apertures. The larger measured aperture (2.82mm) by images, than by global data (0.42mm) strongly indicates that aperture measurements by global data only represent the narrowest restrictions in a wormhole, as expected.

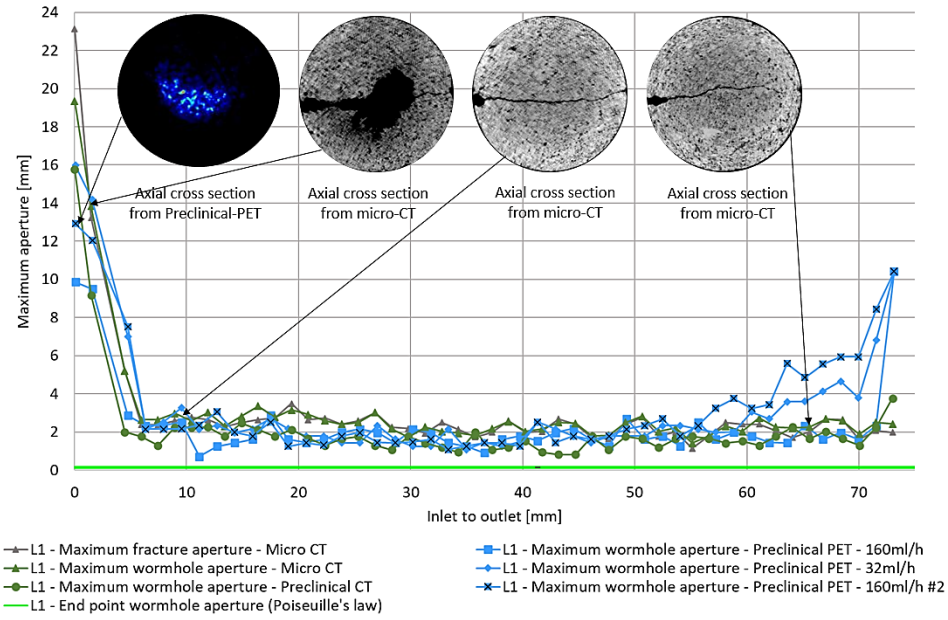

Figure 4.28 – Plot shows measured maximum fracture and wormhole aperture from inlet to outlet side of core sample L1. In addition, end point wormhole aperture from Poiseuille's law was plotted.

Maximum wormhole aperture as a function of core sample length for L2 by preclinical CT is plotted in figure 4.29. The plot also contains the end-point wormhole aperture found from global data. Measured end point wormhole aperture was 0.47mm, while average maximum wormhole aperture for the whole length of the core sample was 2.33mm. The lower end-point aperture by Poiseuille's, than by CT, indicates the same as mentioned for L1; that global data only reflects the narrowest restrictions in a wormhole. A comparison of apertures from Poiseuille's and PET was not obtained, due to cyclotron malfunction in the Small Animal PET/CT-scanner.

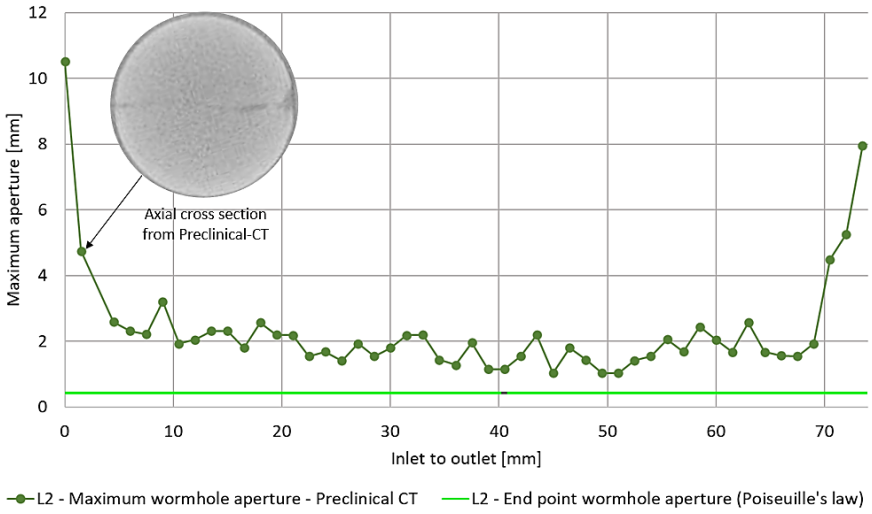

Figure 4.29 – Plot shows measured maximum wormhole aperture from inlet to outlet side of core sample L2. In addition, end point wormhole aperture from Poiseuille's law was plotted.

Measured maximum wormhole aperture for L3 by PET/CT images, with end point wormhole aperture form Poiseuille's is shown in figure 4.30. The largest wormhole aperture was obtained close to the inlet side. The cross-section inserts support the measured maximum apertures, where at the inlet cross section (0mm) measured apertures were substantial larger than the measured maximum aperture for ~33mm into the core sample. The same trend in measured apertures by PET in L1, was also observed for L3; measured average max. aperture from preclinical PET with flow rate 16ml/h (3.01mm) was larger than measured at flow rate of 80ml/h (2.01mm). Flow rate of 80 ml/h was performed at the very beginning of the PET scanning and diffusion of convective flow (traceable brine) with time during PET-scan might explain the larger measured apertures during injection at 16ml/h at a later time. Average aperture measured from PET image at 16ml/h was exactly 1mm larger than average aperture at 80ml/h, which indicates that measured apertures from images obtained from PET-scans at a later time frame (16ml/h) correspond to actual apertures, since the reactive fluid flow had time to diffuse in the whole wormhole area. End-point wormhole aperture found by Poiseuille's law for L3 was 0.43mm, while the average maximum wormhole aperture measured from PET and CT images was 2.54mm. The lower end point aperture by Poiseuille's, than by CT, indicates the same as mentioned for L1 and L2; that global data only reflects the narrowest restrictions in a wormhole.

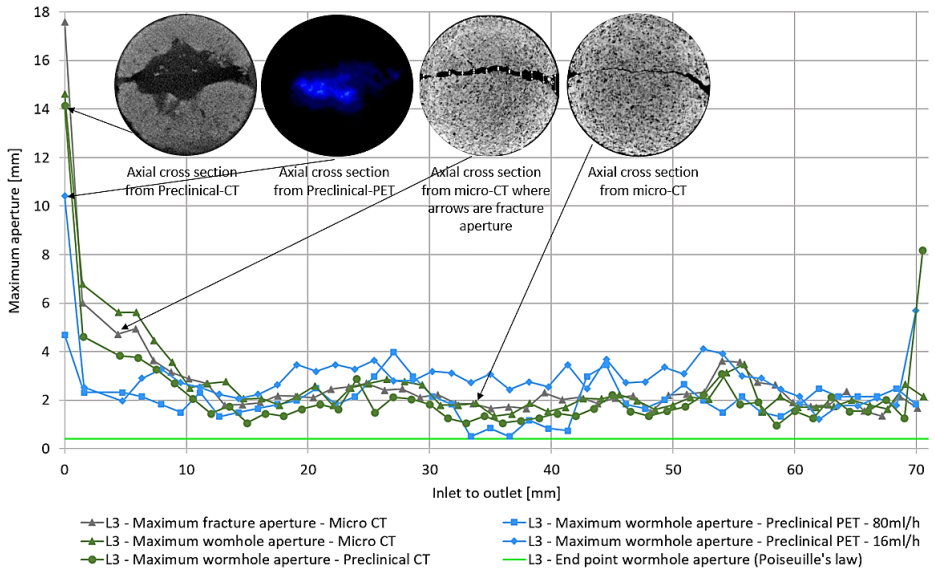

Figure 4.30 – Plot shows measured maximum fracture and wormhole aperture from inlet to outlet side of core sample L3. In addition, end point wormhole aperture from Poiseuille's law was plotted.

Figure 4.31 shows measured maximum fracture aperture, and maximum wormhole aperture for L5. Several small wormholes were detected close to the inlet side, and the longest wormhole within the fracture was chosen as main wormhole (figure 4.19). The main wormhole was only detectable from inlet to ~13.5mm into the core sample. Aperture found from Poiseuille's law was 0.25mm, while average maximum fracture aperture for the main wormhole was 1.38mm. Arrows in the figure with description "narrow restrictions" shows that parts of fracture correspond with measured aperture from global data, while rest of the apertures have higher values. Which implies that using Poiseuille's law for estimating wormhole/fracture aperture only exhibits the narrowest restrictions within the reactive fluid flow area as also shown above for L1, L2, and L3. Because global data only reflects the narrowest restriction in a wormhole. The method cannot quantify the range of apertures.

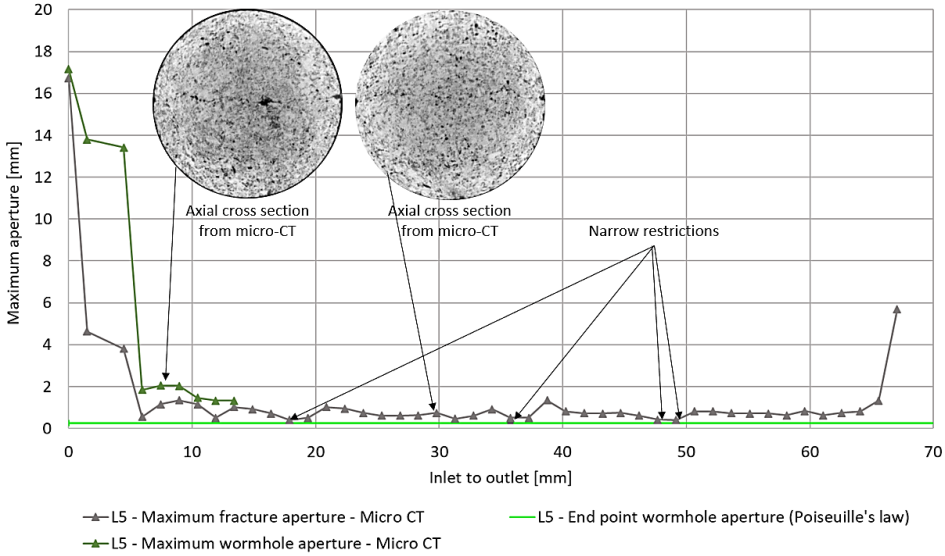

Figure 4.31 – Plot shows measured maximum fracture and wormhole aperture from inlet to outlet side of core sample L5. In addition, end point wormhole aperture from Poiseuille's law was plotted. Note that the wormhole did not extend to outlet.

All four plots (figure 4.28, 4.29, 4.30 and 4.31) shows the same maximum aperture trend. Close to inlet side of the core sample, maximum aperture was measured to be considerable larger than the rest of the core sample. Larger measured maximum apertures were typically within the first 10mm of the core sample. The trend of measured maximum wormhole aperture corresponds well with measured trend of dissolution (section 4.5.2) with larger maximum wormhole aperture and dissolution at the inlet compared to the rest of the core sample. Dissolved calcite particles have been displaced from the core sample, or flow towards outlet and remain in the fracture network. Remained dissolved particles could have caused the lower degree of dissolution towards outlet, and therefore smaller measured apertures. Overall, for L1, L2, L3, and L5, wormhole aperture measured from PET/CT images was considerable larger than the apertures measured using global data with Poiseuille's law. Differential pressure of a core sample during co-injection corresponds to narrow restrictions in the flow path. So, from Poiseuille's law using global data, quantification of only narrow restrictions in a wormhole/flow path could be found. Applying imaging techniques was necessary to give a precise quantification of wormhole/dissolution pattern, and reactive fluid flow propagation through the whole core sample.

Figure 4.32 and 4.33 show measured wormhole/reactive fluid flow volume from PET and CT for core sample L1 and L3, respectively. Figures also contains 3D images from PET and micro-CT scans, and cross section from preclinical CT. The figure displays the time frame during PET-scanning for the respective flow rates. Note that the method for finding wormhole/reactive fluid flow volume is shown in figure 4.27 and explained above. The wormhole volume is presented as percentage of total bulk volume with uncertainties due to the method of calculating wormhole/reactive fluid flow volume.

For core sample L1 (figure 4.32), wormhole volume (whole PET signal) measured by the respective imaging techniques were below 2%. Wormhole volumes measured by dynamical PET images showed a growth in volume with time. The image from PET scan during injection at 160ml/h #2 with a time frame from 0.95-1.15h gave the largest wormhole volume (1.86%), while the PET-scan performed from 0-0.2h showed a smaller wormhole volume (0.807%). The growth in wormhole volume with time, indicates that diffusion of convective flow occurred during PET scanning, which allows the traceable brine to spread in larger parts of the wormhole and possibly into the fracture. Wormhole volume from micro-CT (1.27%) and preclinical CT (1.04%) deviates from each other. The spatial resolution of preclinical CT (125x125x377μm) was much poorer than the micro-CT (29.3x29.3x29.3μm) which made it more difficult to measure the wormhole volume, because edges between matrix and wormhole appeared blurry, whereas in micro-CT image the edges appeared sharp. The largest wormhole volume obtained from the imaging techniques (1.86% of bulk volume) was evaluated towards the initial effective pore volume of the whole core sample (18.3ml, table 4.1) where it was assumed that without the fracture, the reactive fluid flow would have swept the entire pore volume. A discrimination within preexisting wormhole showed that the sweep efficiency and, hence, pore volume favorable for CO_2 sequestration had decreased with ~91%. Wormholing in L1 caused an increased injectivity of CO_2 as discussed in section 4.4.1. However, the discrimination of reactive fluid flow limited to a small volume causes a small reactive surface area, and therefore contributes to less dissolution, which is favorable to limit an overall geomechanical weakening. Local geomechanical weakening is expected to occur by wormholing.

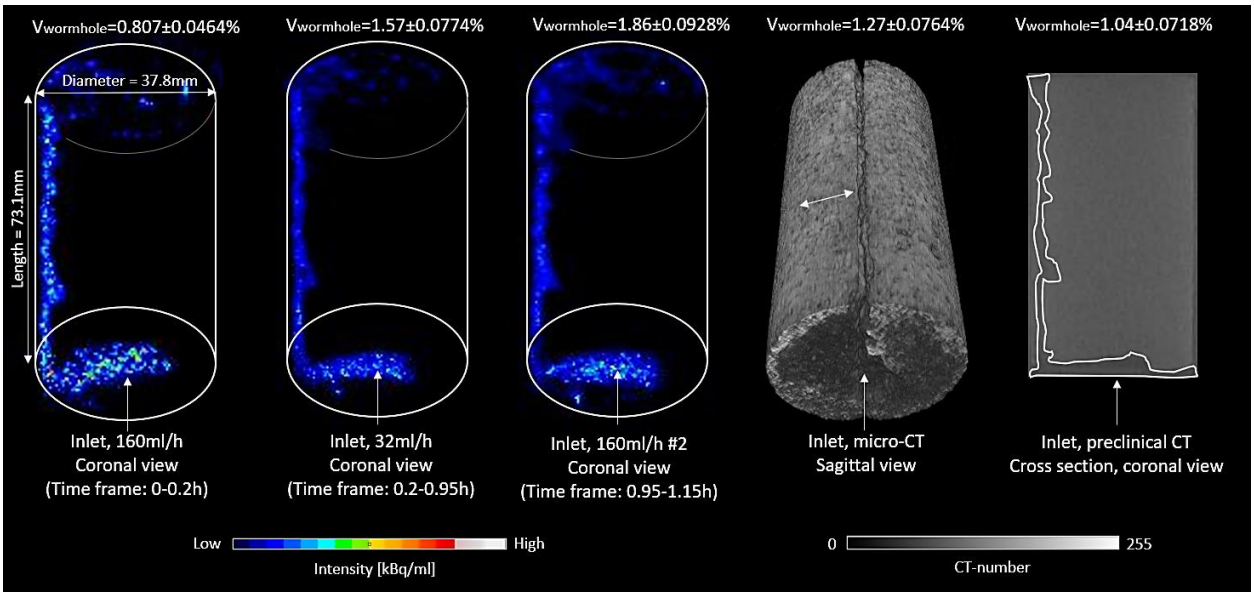

Figure 4.32 – Figure displays 3D-images from preclinical PET-scans and micro-CT scan, and a coronal cross section from preclinical CT for L1. In addition, volume of wormhole and PET-signal from the different imaging techniques. PET images have a 16-color scale, whereas CT images has an 8-bit grayscale.

Wormhole volumes measured from the respective imaging techniques applied on core sample L3 after dissolution are displayed in figure 4.33. From PET-images both wormhole volume and whole PET-signal volume was measured. The strongest PET-signal (light blue area) was assumed to be the wormhole. The largest wormhole volume measured was from PET-image scanned with brine injection at 16ml/h and with the time frame 0.47-0.67h. Which as mentioned above for L1, most likely was due to diffusion of convective flow with time. The measured whole PET-signal, which includes all the intensities detectable in the PET images was largest at the reconstructed image from brine injection at 16ml/h. The volume was measured to be 16.2% of total bulk volume. Whilst reconstructed PET-image from 80ml/h (time frame: 0-47h) showed a volume of 8.05%. The doubled PET-signal volume, from the dynamic PET-images (80ml/h to 16ml/h) shows that lower flow rate (16ml/h) and with time lateral diffusion seems to become considerable, and the reactive fluid flow spreads in larger areas around the wormhole and the fracture (dark blue area). The dark blue area appeared in areas around fracture, indicating that some of the pore network had been affected by the reactive fluid. The indication could be supported by a large degree of dissolution in fracture area for L3 shown in section 4.5.2. The volume of the whole PET-signal (16.2% of bulk volume) gives a wider reactive surface area, and therefore a probability of more dissolution of calcite within L3, than shown in L1. The larger reactive surface area for L3 than for L1, may have transpired due to the estimated initial average fracture apertures which for L3 ($\bar{e}_{Buckingham}$ =0.061mm) was larger than for L1 ($\bar{e}_{Buckingham}$ =0.052mm). The reactive fluid would more easily disperse and flow into a larger area (low capillary pressure) than a smaller area (high capillary pressure), due to a larger concentration gradient (section 1.4) and lower capillary pressure in wider areas. In addition, L1, might have had more substantial difference between the aperture of the longitudinal partially open sides and the fracture aperture, than L3. Leaving a more substantial discrimination of the reactive fluid to flow in the open side in L1. Whereas L3, shows less discrimination of reactive fluid to flow in the established flow channel (partially open side). The volume of wormhole measured from all imaging techniques applied for L3 was

near 1.5% of total bulk volume. The largest measured PET signal was 16.2% of bulk volume and evaluated towards the initial effective pore volume (18.8ml, table 4.1) where it was assumed that without the fracture, the reactive fluid flow would have swept the entire pore volume. A discrimination within pre-existing wormhole and fracture in L3, showed that the sweep efficiency and, hence, pore volume favorable for CO_2 sequestration had decreased with ~33%. For L3, as also mentioned for L1, wormholing increases the injectivity of CO_2 shown by a higher permeability after dissolution (section 4.4.1). In L3, discrimination of reactive fluid flow was less than for L1, shown by PET-signal within and areas around fracture.

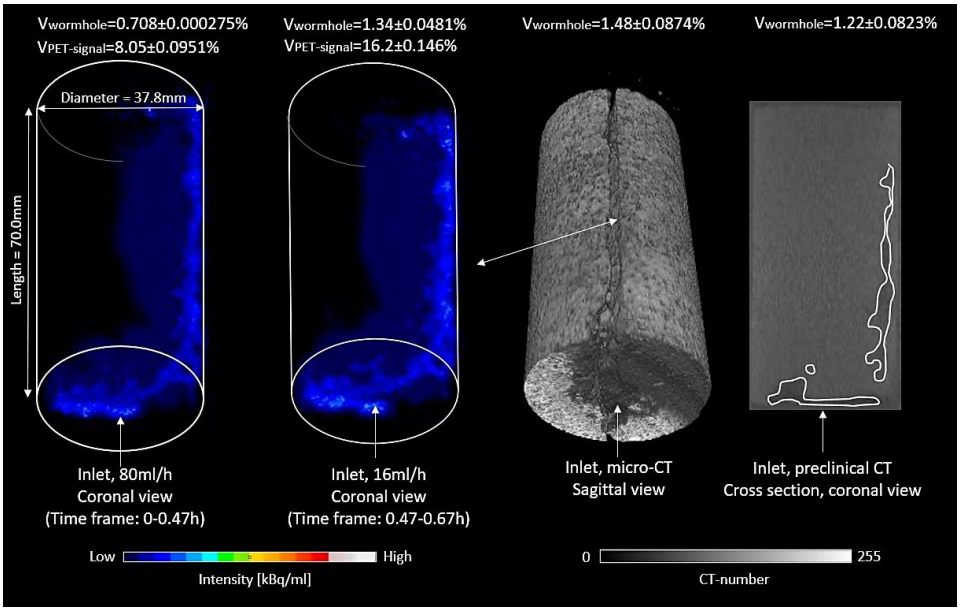

Figure 4.33 – Figure displays 3D-images from preclinical PET-scans and micro-CT scan, and a coronal cross section from preclinical CT for L1. In addition, volume of wormhole and PET-signal from the different imaging techniques. PET images have a 16-color scale, whereas CT images has an 8-bit grayscale.

Whole PET-signal from L3 indicates that most of the reactive fluid flow appears within wormhole, by the highest intensity occurrence. Mean intensity of wormhole area (white outline) measured from a coronal cross section (figure 4.34) was 324kBq/ml. Whereas, mean intensity in dark blue area was 108kBq/ml.

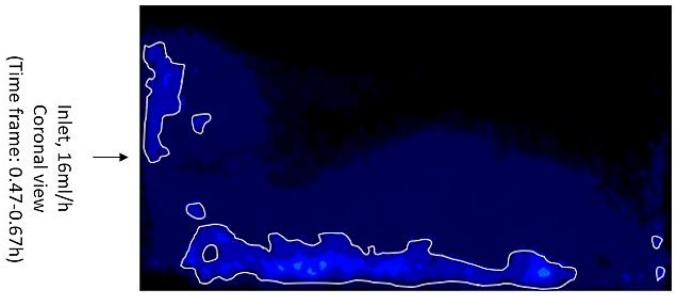

Figure 4.34 – Coronal cross section of core sample L3, during PET-scanning with traceable brine injection at 16ml/h.

PET-images appears to be more beneficial for measurements of wormhole characteristic, and reactive fluid flow localization than CT images alone. Measured wormhole apertures and volumes from CT images alone was based on a visual interpretation and assumptions on where the wormhole was located.

Whereas PET images give a direct reactive fluid flow location, and hence the real area where dissolution of calcite occurred, i.e., dissolution/flow patterns as for example a wormhole. PET-images could also reveal that volumetric flow rate and time frame effects the prevalence of the reactive fluid flow. Where lower flow rates (for L3) and later time frame exhibit a larger reactive fluid flow area. J. Kulenkampff et al. (2008) performed PET-scans to evaluate diffusion in fractures, by changes in flow rates. It was observed significant differences of the flow field at different flow rates during PET-scans. At higher flow rates the tracer appeared to travel along a narrow flow path and immediately reached the outlet, while at lower flow rates lateral dispersion becomes significant and the tracer distribution propagates more uniformly over the full width of the fracture. This effect was primarily due to the increasing impact of molecular diffusion within the fluid-filled fracture at the low fluid flow rate. This study corresponds well with the measured prevalence (volume) of PET-signal for core sample L3. Whilst for L1, the study corresponds for the two first flow rates, where 160ml/h shows a smaller volume of PET signal than at a flow rate at 32ml/h. The flow rate of 32ml/h was followed by injection at 160ml/h for the second time, and the PET-signal was still increasing, which does not correspond with the former study. So, the traceable brine from L1, shows that by changing the flow rate from high to low, and back to high again, does not affects the prevalence of the PET-signal as expected from the former study. Therefore, the increased PET signal for L1 and L3, strongly indicates that the diffusion of traceable brine was more dependent on time, and not changes in flow rates. Note that the intensities in a PET-signal decreases with time due to decaying of FDG, giving an increase of noise around the visible PET-signal. Low-activity values from PET-scan are more affected by background noise, than higher-activity values. (Johannes Kulenkampff et al., 2016; Zahasky & Benson, 2018). The increased background noise as detected scatter events (photons from annihilation event) outside line of response (LOR) or random counts caused by a false LOR during PET-scan, gives poorer quality of the PET-image. The background noise could be quantified within a ROI in PET image outside of the core sample and inlet tubing, where the sum of events (PET-signal) was measured. Table 4.9 shows the volumetric flow rate, time frame and sum of events outside for core sample L1 and L3 during PET scan. For both core samples, the sum of events within ROI of background increased with time which indicates that more noise was present in reconstructed images conducted at later time frame. Caused by the decreasing activity values of FDG with time (decaying). The background noise contributes to giving a poorer quality of the PET-images, which gives fewer clear edges of the PET-signal. Therefore, were measurements of PET-signal at a later time frame more uncertain, and hence wormhole/reactive fluid flow volume measurements more uncertain.

Table 4.9 – Displays the volumetric flow rates and time frame for each flow rate during PET-scanning, and the sum of intensity measured in a ROI outside the core sample in PET-images reconstructed for the different rates.

CORE ID	VOLUMETRIC FLOW RATE [ml/h] DURING PET-SCAN	TIME FRAME [h]	SUM INTENSITY ROI OUTSIDE [Bq]
L1	160	0 - 0.20	18.98
L1	32	0.20 - 0.95	42.51
L1	160 #2	0.95 - 1.15	45.44
L3	80	0 – 0.47	47.54
L3	16	0.47 – 0.67	144.52

L = EDWARDS YELLOW LIMESTONE

4.5.5 Quantifying localization of reactive fluid saturation by preclinical PET images

A simple streamtube analysis was used to quantify location of reactive fluid flow in dynamic PET-images (reconstructed images for each flow rate) for L1, and L3. Quantifying the location of fluid flow by PET could describe the reactive fluid saturation within the core sample, and hence reveal location where dissolution occurred. A simplified method for streamtube analysis in this work was inspired by B. Brattekås, Gauteplass, Brekke, Fernø, and Ersland (2020), where sub-core scale (streamtube) analysis was performed for quantification of local displacement variations during multiphase flow by using PET-images. The method used in this work is displayed in figure 4.35. Core-scale PET-images were sliced in five coronal cross sections with a separation of 2.5mm between each. The center cross section was located to represent the center of the core sample (full known diameter of core sample) parallel to the fracture. The cross sections were located such that the fracture area was covered by the simple streamtube analysis. Each cross section was divided into six equal smaller flow elements (2D streamtubes) parallel to the flow direction. The sum of PET-signal within each streamtube was measured and normalized for comparison. Streamtubes for each cross section with dynamic PET-images were compared, in addition streamtubes in all cross sections for the respective PET-images.

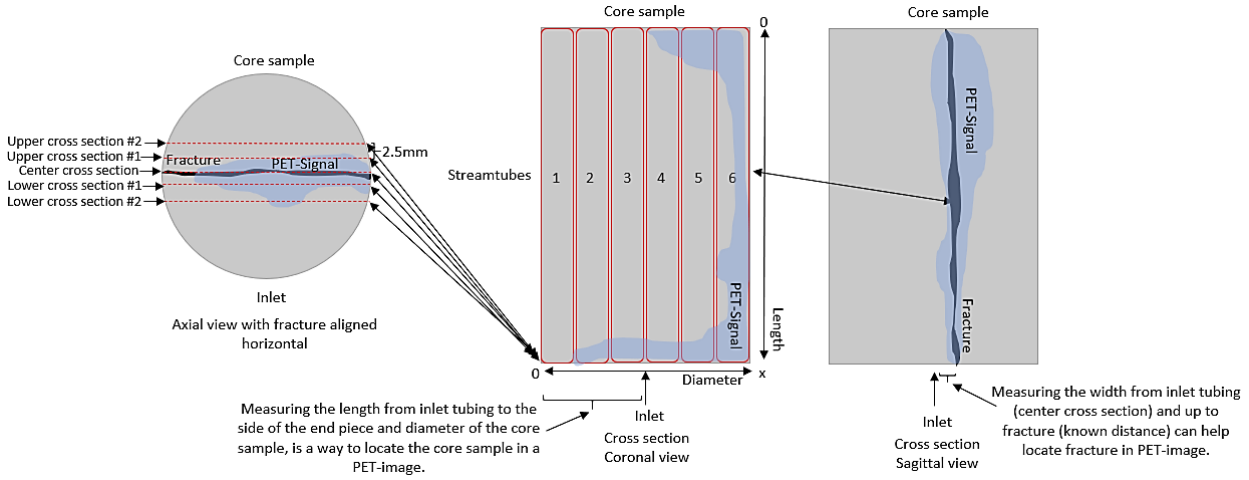

Figure 4.35 – Method for measuring PET-signals in streamtubes for quantification of local fluid flow, hence where dissolution has occurred. A CT-image obtained before PET-scan is also a way to locate the core sample in a PET-image, by overlying the modalities.

Figure 4.36 shows plots of normalized PET-signal between the streamtubes within each cross section (CS) obtained from PET-images for L1. The plots compare PET-signal in streamtubes (ST) within each statically reconstructed image obtained during injection of traceable brine at 160ml/h, 32ml/h and 160ml #2. The time frames for each respective flow rate can be found in table 4.9. For all three flow rates most of detected annihilations events (PET-signal) occurred within ST1. For center CS (fracture), 100% of the streamtubes (ST1) had a PET-signal, which gives a fully reactive fluid saturation area of 6.3x73.1mm^2, at the very left center side of the core sample (core sample orientation during PET-scan is shown as inserts in the plots). In ST1, upper CS #1 for all three flow rates gave an average of 31% reactive fluid saturation compared to 13% for lower CS #1. 100% fluid saturation in ST1 for center CS and the larger reactive fluid saturation in upper CS (31%) #1 compared to lower CS #1 (13%) indicates that reactive fluid saturation was mostly located at left center side and slightly above that, probably affected by the initial

heterogeneities of the longitudinal partially open side of fracture. For center CS and upper CS #1 and #2, a rapid decreasing occurrence of events were observed from ST1-6, where in ST3-6 small amounts (average of 1%) of PET-signal were detected. The small amounts of events were mostly due to the visual observed PET-signal present at the inlet side of the core sample (see 3D PET-signal insert in plots). Events detected in especially ST6 could have been mostly due to background noise since the PET-signal was not visually distinguishable from the images. Most of the reactive fluid saturation occurred within ST1 (100% for center CS) and decreased rapid towards ST6. The simple streamtube analysis by dynamic PET images for L1, strongly suggest that most dissolution and hence development of a wormhole occurred at the very left center side of the core sample, i.e., in the pre-existing wormhole. Changes in flow rate did not affect the preferable flow path of reactive fluid particularly.

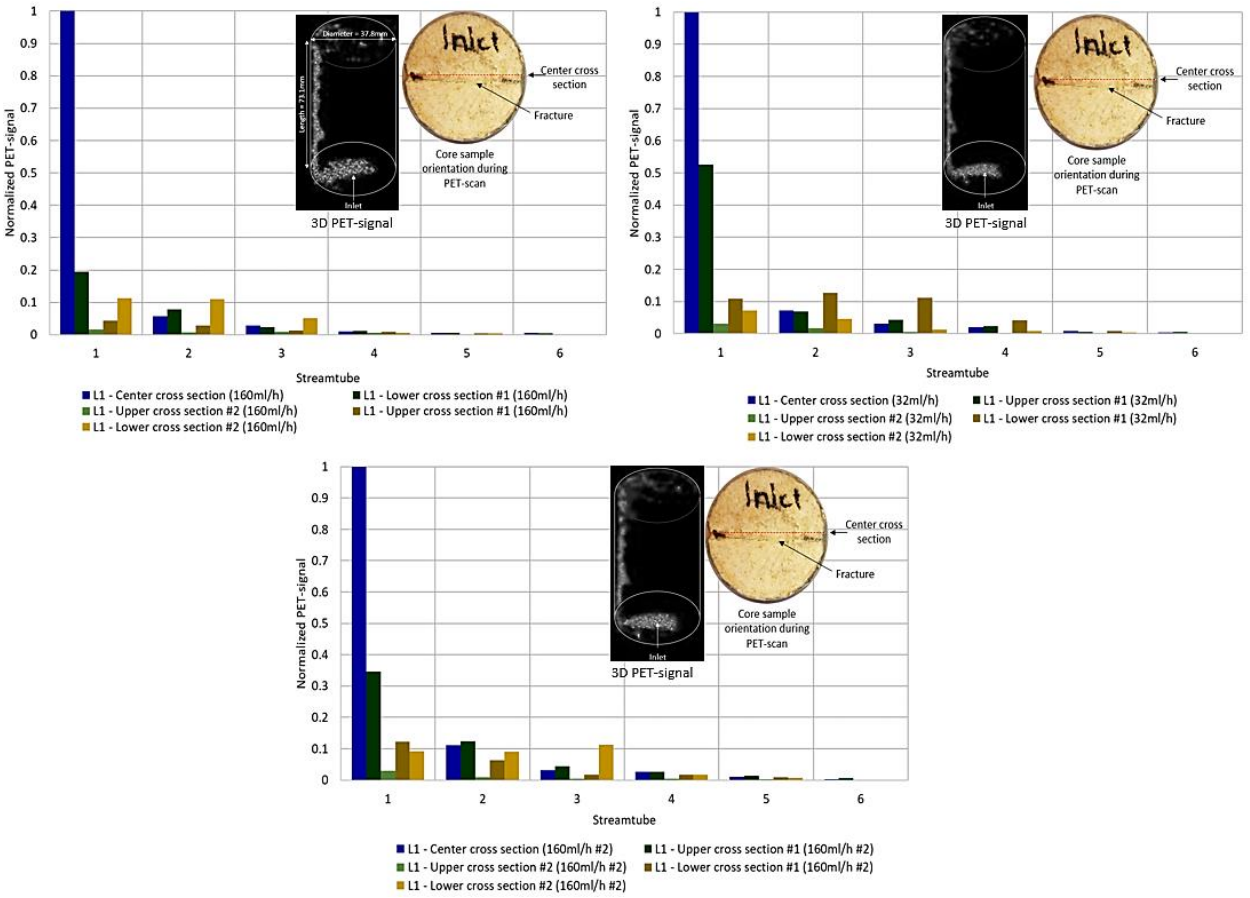

Figure 4.36 – Plots show simple streamtube analysis for L1 by dynamic PET-images obtained for flow rate 160ml/h, 32ml/h, and 160ml/ #2. The plots contain normalized PET-signal as a function of streamtubes with 3D PET image, and picture of core sample inlet after dissolution.

Figure 4.37 shows plots of normalized PET-signal between the streamtubes within each cross section (CS) obtained from PET images for L3, similar as for L1. The plots compare PET-signal in streamtubes (ST) within each PET-image obtained during injection of traceable brine at 80ml/h and 16ml/h. The time frames for each respective flow rate can be found in table 4.9. For both statically reconstructed image, most detected PET-signal for all cross sections (48%) occurred within ST6, followed by 42.5% for ST5, 28% for ST4, 13% for ST3, 8.4% for ST2, and 1.5% for ST1. In ST6, upper CS #1 (by 80ml/h), show 100% reactive fluid saturation, whereas for 16ml/h, ST6 in center CS show 100% reactive fluid saturation, which indicates that reactive fluid flow moved downwards due to the change in flow rate. The lower flow rate (16ml/h) and later time frame might give the reactive fluid time to diffuse laterally within the fracture, and hence fill more of the flow path. Generally, most reactive fluid saturation occurs at center CS, while the upper CS #1 shows more reactive fluid saturation than lower CS #1. Inserts of core sample orientation during PET-scan (inlet) show that the longitudinal partially open side of the fracture corresponds to center CS, while the rest of the fracture has an upwards curved shape, explaining the observed larger number of events in upper CS (23%), than lower CS (16%). From most detected events in ST6, the average events decrease almost linearly towards ST1. The decrease from one side to another for L3 was not that rapid as observed for L1 (power-like decrease), which clearly indicates that the reactive fluid saturation in L3 occupies some area within the fracture. In addition, the relatively high counts of events in lower CS #2 and upper CS #2, strongly suggest that not only the fracture area was affected by the reactive fluid, but also part of the pore network close to the fracture. As mentioned most counts of events occurred within ST6 (48%), and decreased linearly towards ST1, which indicates that the preferable flow path for reactive fluid is within the ST6 area, especially at center CS, and upper CS #1, i.e., within the pre-existing wormhole. The preferable flow path occurred visually as a wormhole in PET-images, by the strongest intensity (see 3D PET-signal inserts in plots). Whereas the PET-signal in ST5-3 strongly suggest saturation of reactive fluid within the fracture and pore network in connection with fracture. The preferable flow path of reactive fluid flow did not change particularly with changes in flow rate.

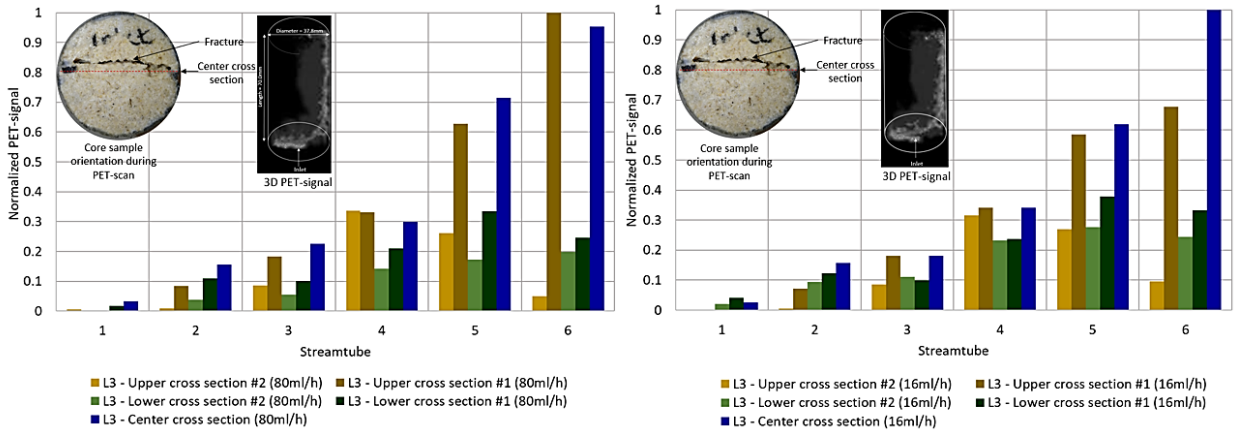

Figure 4.37 – Plots show simple streamtube analysis for L3 by dynamic PET-images obtained for flow rate 80ml/h and 16ml/h. The plots contain normalized PET-signal as a function of streamtubes with 3D PET image, and picture of core sample inlet after dissolution.

The simple streamtube analysis displayed as normalized PET-signal as a function of streamtubes is visually comparable to the 3D-PET images. Streamtube analysis, hence, seems to be an efficient method for

quantifying heterogeneities and, hence, preferred flow paths for reactive fluid flow, including dissolution. For future work, applying a more advanced streamtube analysis, by applying more cross sections and streamtubes both parallel and perpendicular to the flow, may reveal the reactive fluid saturation and dissolution voxel by voxel. Investigation of reactive fluid saturation at the voxel-scale could give a more precise localization of the preferred fluid flow path and could describe volume of dissolution accurately if PET-scans of traceable brine injection before and after dissolution are performed. A 3D simulation model of streamtube analysis on voxel-scale for accurate descriptions of heterogeneities in porous media by PET have previous been performed by Zahasky and Benson (2018). Note that streamtube analysis plots for each cross section for L1, and L3 can be found in appendix E.

4.5.6 Evaluation of best fitted imaging techniques and modalities for pore/fracture network and reactive fluid flow quantification at the core-scale

Three different imaging techniques, and two different modalities have been used in this thesis for an initial evaluation of what technique and modality that was best fitted for quantification of dissolution. Micro-CT, preclinical PET/CT, and clinical PET/CT were applied, and their respective spatial resolution used in this thesis can be found in table 4.10. Imaging techniques have been evaluated by both their spatial resolution and the type of quantification that could be unlocked from each technique.

Table 4.10 – Voxel size for the imaging techniques applied and types of quantification found by PET and CT.

IMAGING TECHNIQUE/MODALITY	VOXEL SIZE [μm]/ SPATIAL RESOLUTION	CORE ID	UNLOCKED QUANTIFICATION OF:
MICRO-CT BEFORE	29.2x29.2x29.2	L1, L2, L3, L4, L5	Pore size distribution and heterogeneities
MICRO-CT AFTER	29.3x29.3x29.3	L1, L3, L5	Fracture, pore network, dissolution patterns, dissolution, large and smaller heterogeneities
PRECLINICAL CT	125x125x377	L1, L2, L3	Dissolution patterns, dissolution, large heterogeneities
PRECLINICAL PET	400x400x400	L1, L3	Dissolution patterns, dissolution, heterogeneities, reactive fluid flow path/area/volume, (preferable flow path), reactive fluid saturation
CLINICAL CT	168x168x1500	L3	Large heterogeneities and dissolution patterns, but not quantifiable
CLINICAL PET	825x825x1500	L3	Reactive fluid flow, but not quantifiable

Micro-CT has the best spatial resolution of all techniques applied, where core samples were scanned with a spatial resolution of ∼29μm. The high spatial resolution gives a low signal to noise ratio which is preferable. The high resolution in micro-CT enables the whole fracture, dissolution patterns and all pores and vugs with a size above spatial resolution. Therefore, micro-CT images are suited for quantification of pore size distribution, determination of heterogeneities, segmentation of pores and fracture network, and estimation of dimensions and volume of dissolved area/dissolution patterns. Micro-CT images conducted

before and after dissolution can quantify the degree of dissolution caused by reactive fluid flow. However, limitations in micro-CT images regarding quantification of dissolution patterns, is the visual interpretation of where the reactive fluid flow occurs. The location and quantification of dissolution patterns is therefore based on assumptions made by the interpreter. In addition, a main restriction is computer and software performance. A micro-CT image contains a set of several thousands of files, where one micro-CT image is at a size of 50GB (in this thesis). The large size of the images requires a computer with high enough RAM, and GPU. For a proper analysis for whole (all files included) micro-CT image of core samples with the dimensions used in this thesis, a minimum of 256GB RAM is required. In this thesis micro-CT images where analyses with an increment between slices, due to computer limitations. The computer used in this thesis had 32GB RAM which complicated the image analysis. In addition, image analysis software ImageJ FIJI is a free version and simple segmentation and volume rendering of the pore network was not enabled. However, a 3D image of the whole core sample was obtained in FIJI, in addition to a volume viewer where it is possible to browse through cross section within xy, xz, and yz plane of the core sample. Note that ImageJ FIJI also was used to obtain pore size distribution, quantifying absolute porosity before and after dissolution, measure wormhole/fracture apertures, and generate cross section images of dissolution patterns.

Preclinical CT had a poorer spatial resolution than micro-CT, with a voxel size of 125x125x377μm, and hence a larger SNR. Preclinical CT did not enable the fracture, nor parts of the pore network due to the low resolution (CT parameters are meant for small animal imaging (e.g., maximum tube voltage 70kVp)) However, wormhole/dissolution channel measurements (aperture and volume) could be obtained, but with an even higher uncertainty than by micro-CT, due to the visual interpretation of localization of dissolved area. Preclinical CT was nevertheless crucial for positioning of the field of view as a preparation to PET-scanning. In addition, a preclinical CT could directly overlie a PET-image of the same core sample, giving a direct comparison and coupling of larger heterogeneities and reactive fluid flow. The software used for image analysis on preclinical CT was FIJI, for measuring wormhole aperture and volume, and InterviewFusion for overlying PET-images. InterviewFusion could also give cross section images in all planes. 3D images are normally possible to obtain but was not possible to obtain for images in this thesis, due to thresholding problems.

Preclinical PET showed to be the best suited technique to quantify dissolution, and especially dissolution patterns, because it enables the actual reactive fluid flow, and hence preferable flow path, wormhole dimensions and volume, areas other than preferable flow path that was saturated with reactive fluid, and the degree of dissolution. The voxel size of preclinical PET was 400x400x400μm and the PET images alone could reveal the most important characteristics needed for analysis of dissolution and reactive fluid flow. A combination of preclinical PET and micro-CT unlocks the most important characteristics needed for quantification of dissolution. High temporal resolution provides insight into dynamic fluid flow, which is a significant advantage.

Clinical PET and CT obtained for L3, had the poorest image voxel size, with 168x168x1500μm for CT, and 825x825x1500μm for PET. In addition, the field of view positioning was way too large for the dimensions of a core sample. Therefore, no data or quantifications were obtained from clinical PET and CT in this thesis.

Figure 4.38 shows coronal cross sections from L3 where all imaging techniques were applied, for a visual demonstration of differences in spatial resolution. Each imaging technique is represented and their respective spatial resolution for each cross section can be found in table 4.10.

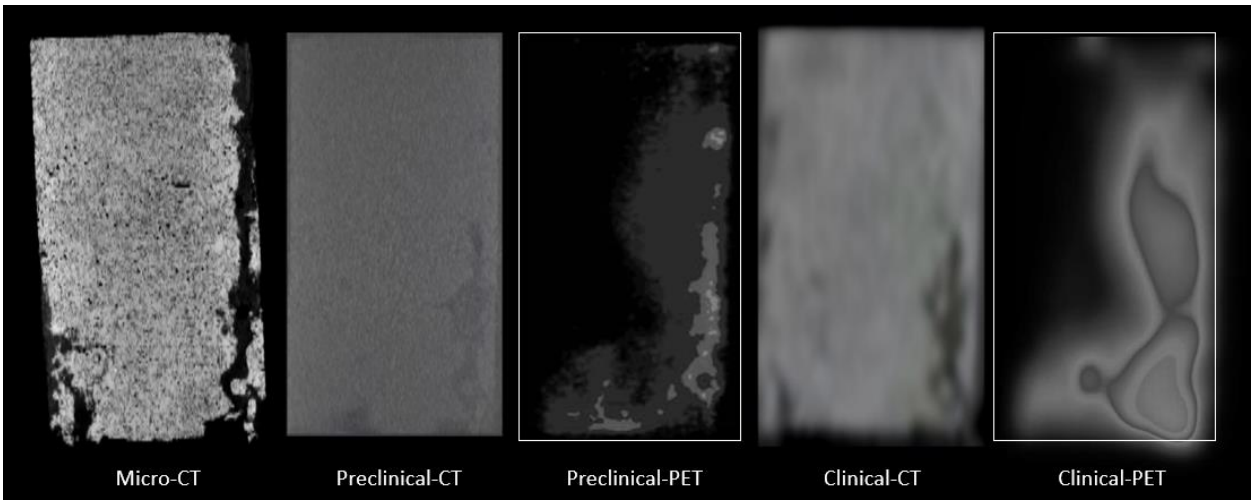

Figure 4.38 – Coronal cross section obtained by each imaging technique applied for L3.

4.5.7 Important observations of dissolution found by application of in-situ imaging techniques

Several important observations were obtained during PET/CT analysis:

- Micro-CT images showed that dissolution in fractured core samples with injection rate of 40ml/h, 80ml/h, and 160ml/h caused compact conical dissolution at inlet side. However, wormhole formation through the whole unit length of core sample L1 (160ml/h) and L3 (80ml/h) as an addition to compact conical dissolution were obtained. The extend of the wormhole reveals that the reactive fluid flow was discriminated in the high permeability area (longitudinal partially open sides of the fracture) in L1 and L3. Whereas for L5 (40ml/h), where a main wormhole only extended 13.5mm from inlet into the tight fracture, indicating that the fracture only was slightly more permeable than the pore network.
- Absolute porosity measurements for L1, L3 and L5 showed that dissolution mainly affected the inlet side of the core sample and towards the outlet side dissolution decreased. For L1 and L3 the most affected area was around fracture area. For L5 neither fracture area or whole cross section were affected substantially, except close to the inlet and outlet.
- Overall, for L1, L2, L3, and L5, wormhole apertures measured from PET/CT images were considerable larger than the apertures measured using global data with Poiseuille's law. Differential pressure of a core sample during co-injection corresponds to narrow restrictions in the flow path. So, from Poiseuille's law using global data, quantification of only narrow restrictions in a wormhole/flow path could be found. Therefore, applying imaging techniques were necessary to give a precise quantification of wormhole/dissolution pattern, and reactive fluid flow propagation through the whole core sample.

- From PET-images, the PET signal showed that the sweep efficiency of the reactive fluid flow decreased in L1 and L3, due to the discrimination of reactive fluid flow within the pre-existing wormhole and fracture, which also decreases CO_2 storage potential.
- PET-images appears to be more beneficial for measurements of wormhole characteristic, and reactive fluid flow localization than CT images alone. CT images alone exhibits the pore structure, and it could be difficult to estimate the location of the wormhole, and hence quantify the wormhole characteristics. Whereas a PET image gives the real reactive fluid flow and immediately displays the dissolution/flow pattern.

5 Conclusions and future work

This chapter presents conclusions of the analysis obtained from the experimental work, and suggestions for future work on this research topic.

5.1 Conclusions

- The expected heterogeneous nature of Edwards yellow limestone and Silurian dolomite core samples were confirmed by micro-CT. Imaging demonstrated a large range in pore and vug size distribution, leaving a range from 33 - 3095µm for limestone and 33-7663µm for dolomite. Smaller pores were not captured due to limitations in spatial resolution.
- Dissolution of carbonate rock occurred during co-injection of CO_2 and brine in all core plugs, largely controlled by the initial fracture network.
- In fracture network A (longitudinal flow channel at the fracture side), a decreasing pressure trend was measured in three experiments (L1, L2, L3), i.e., injectivity increased. Reactive fluid flow was discriminated in the partially open side of the longitudinal fracture and localized dissolution within the flow channel occurred; confirmed by PET-images for L1 and L3.
- In fracture network B (tight fracture), an increasing pressure trend was measured in two experiments (L4, L5), i.e., injectivity decreased. Reactive fluid flow was therefore not discriminated particularly in the fracture, and dissolution outside fracture area was confirmed by micro-CT image for L5.
- An XRD-analysis of produced particles were performed (appendix B), which confirmed that particles produced in effluents during CO_2 and brine co-injection was 100% calcite. pH measurements also indicate calcite dissolution, visible by an increasing effluent pH, due to buffering.
- Overall, wormhole aperture measured from PET/CT images was considerable larger than the apertures derived from global data with Poiseuille's law. The global pressure measurements during co-injection correspond to narrow restrictions in the dissolved flow path.
- *In-situ* imaging was crucial to give a precise quantification of wormhole/dissolution pattern, and reactive fluid flow propagation through the core samples.
- A simple streamtube analysis performed on PET images seem to capture heterogeneities well and can be used to quantify preferred flow paths for reactive fluid flow.
- The work in this thesis strongly suggests that preclinical PET with micro-CT gives the best opportunities to quantify dissolution and wormholing due to the combined high spatial and temporal resolution. PET-images were beneficial for measurements of wormhole characteristic and reactive fluid flow localization, whereas micro-CT-images reproduced the pore structure to visually establish the location of the wormhole. A combination of preclinical PET and micro-CT unlocks the most important characteristics needed for quantification of dissolution.

5.2 Future work

Some suggestions for future work within this subject are listed below:

- Investigate dissolution during co-injection with several fractions of CO_2 and evaluate the suppression CO_2 causes on the reactive fluid (carbonic acid) flow.
- Perform baseline injection with traceable brine imaged by PET before dissolution for comparison. Use the PET-images to quantify initial heterogeneities and couple the results to PET-images after dissolution.
- Investigate dynamic dissolution during co-injection by applying PET-imaging, which can be coupled to pressure data. Both on fractured and whole core samples.
- Extend the simple streamtube analysis for a more thorough investigation of reactive fluid flow distribution.
- Perform co-injection on dolomite (D11-D12), and chalk core samples (C13-C15).
- Investigate dissolution dependency on wettability, using oil-wet limestone core samples (L7-L10).
- Investigate the impact of calcium overload in the injected brine composition on dissolution.

Appendix

A Theory, experimental procedure, wettability measurements by Amott-Harvey wettability index, and analysis of wettability alteration

A.1 Wettability

In this thesis, the wettability of four Edwards yellow limestone core samples (L7-L10) were altered to oil-wet conditions, and the Amott-Harvey wettability index was measured. It was initially meant to investigate CO_2 injection in both water-wet and neutral-wet systems, but only water-wet systems were considered. Wettability have shown to have an effect on waterflood behavior, irreducible water saturation, residual oil saturation, dispersion and electrical properties (Fernø, Torsvik, Haugland, & Graue, 2010).

From Craig (1971) wettability is defined as: "The tendency of one fluid to spread on or adhere to a solid surface in the presence of other immiscible fluids". Wettability in a rock-oil-brine system is a crucial factor that is controlling the flow, location, and distribution of fluids in a reservoir, and influences capillary pressure, relative permeability, waterflood behavior, electrical properties, and tertiary recovery. Factors that can alter the original wettability in a reservoir is by adsorption of polar compounds and/or deposition of organic matter originally in place by the migration/injection fluid (e.g., crude oil or CO_2). As well as brine chemistry, ionic composition, pH, mineral surface, pressure, and temperature of the system. Surface-active compounds are more present in heavier fractions of crude oil, like resins and asphaltenes, which have the most polar compounds (William G. Anderson, 1986).

Consider a reservoir with a system of rock-oil-brine interactions; the system is water wet when the water occupies the small pores and has contact with most of the rock surface. The system is oil-wet when the location of the fluids is reversed from the water-wet system. If the rock in the system has no strong wetting preference, the system is neutral-wet. Wetting preferences of reservoirs range from strongly water-wet to strongly oil-wet with neutral-wet between. Besides these two wetting preferences (strong and neutral wettability), there is a third type called fractional wettability (FW). Here the reservoir has spot like oil-wet sites on the rock surface, the origin of this state could be variation in mineralogy, precipitation, or that the pore shape consists of flat surfaces. In figure A.1 the term mixed-wet is used, this term is a special type of fractional wettability. In mixed wettability where it is likely that oil has migrated (primary drainage) into a water-wet formation, the oil occupying the larger spaces of the pores has altered the wettability and the contacted pore surfaces. Mixed wettability is divided into mixed-wet large and mixed-wet small, where large means that the larger pores have an oil-wet preference and small means that the smaller pores have an oil-wet preference. Note that the difference between fractional- and mixed-wettability is that the former has no specific locations for the oil-wet surfaces, but mixed wettability has (Salathiel, 1973).

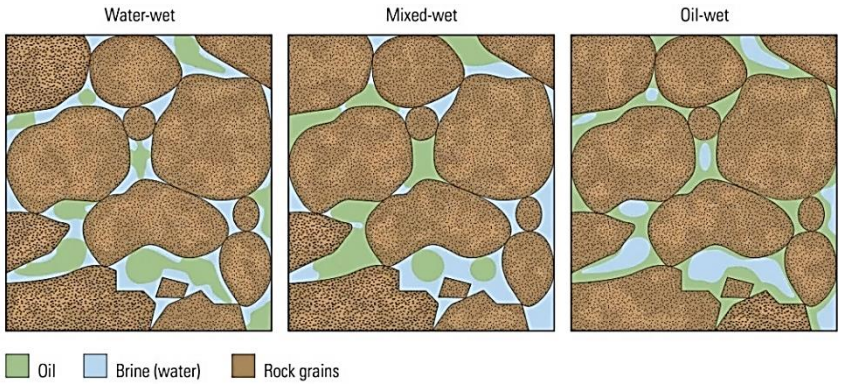

Figure A.1 - Illustration of different wettability preference in a rock-oil-brine system. For water-wet system, the oil remains in the center of the pores. For mixed-wet system, oil has displaced water from some of the grain surface. For the oil-wet system, water is in the middle of the pores. Figure obtained from Abdallah et al. (1986).

All reservoirs were initially water-wet since reservoirs were deposited in an aqueous environment and that oil migrated later in the reservoir. Extensive laboratory experience has given the conclusion that the wettability in a reservoir strongly depends on the absence or presence of polar compounds of the penetrating fluid. The effect of the polar compounds depends on which characteristic the rock have, if it is silica, carbonate or clay (Craig, 1971). In this thesis carbonate core samples are considered, and they are assumed to have a strongly water wet preference, since the outcrops never have been naturally exposed to any other fluid than water. Carbonate rocks have a positively charged, weakly basic surface and therefore tends to adsorb simple organic acids. Carbonate HC reservoirs have a wettability from oil-wet to neutrally wet. (William G. Anderson, 1986), whereas carbonate saline aquifer is water wet. In a carbonate reservoir it is beneficial to inject CO_2 for EOR purposes. CO_2 contributes to a change in capillary forces between oil and water and results in a greater oil recovery. Wettability of a carbonate rock is in this thesis important to understand because it plays a vital role to predict structural and residual trapping capacities.

A.2 Fluid preparations

Preparation and filtration of crude oil was performed as suggested by Ferno et al. (2010). To mix the Ekofisk crude oil before collecting it into smaller containers, the barrel was rotated. Thereafter, crude oil was transferred to an accumulator cell and injected through a limestone filter. The limestone filter was drained with crude oil to a low water saturation before filtration. During filtration, the crude oil was injected through the limestone filter at constant rate to remove impurities. All this inside a heating cabinet of 80°C. The filtered crude oil was collected and stored in closed containers at 80°C with a minimum air exposure and interference until it was used to alter the wettability of four limestone core samples. Filtration of crude oil was performed in the same setup (figure A.2) as used for wettability alteration.

As suggested by Fernø et al. (2013) n-decane was filtered through a alumina- and silica-filled column, This was performed for the purpose of removing surface active components. During filtration, the components of the filter became discolored and the filtered decane appeared clearer. After filtration, the filtered decane was stored in closed containers at room temperature.

A.3 Wettability alteration by dynamic aging method

For altering the strongly water-wet preference of the chosen core samples (L7-L10), a dynamic aging method was used, and the experimental setup shown in figure A.2. The procedure of Ferno et al. (2010) was applied. The wettability alteration was started by draining the core sample to S_{wi} with filtered crude oil and with a constant pressure gradient up to 2 bar/cm. To obtain a low and uniform S_{wi} at least 2.5 pore volumes of filtered crude oil were injected in both directions of the core sample and until production of water had ended for several minutes. The production of brine was measured to find S_{wi}, where the core sample was assumed to be 100% saturated with brine. After drainage, the rate was set to 1.5ml/h and the core sample was flooded with crude oil for three days each way (a total of 144h). After six days of aging, the filtered crude oil was displaced with decaline, then decaline was displaced with n-decane. Both displacements were performed at a constant rate of 50ml/h and 2.5 PV was injected each way. Decaline was used to prevent a mixing of mineral oil and crude oil for avoiding asphaltene precipitation (A. Graue, Aspenes, Bogno, Moe, & Ramsdal, 2002). All the steps of the dynamic aging method were performed in a heating cabinet at 80°C. After aging, the core samples were stored in containers with n-decane and cooled to room temperature for at least 24 hours to prepare for measurements of the Amott-Harvey wettability index.

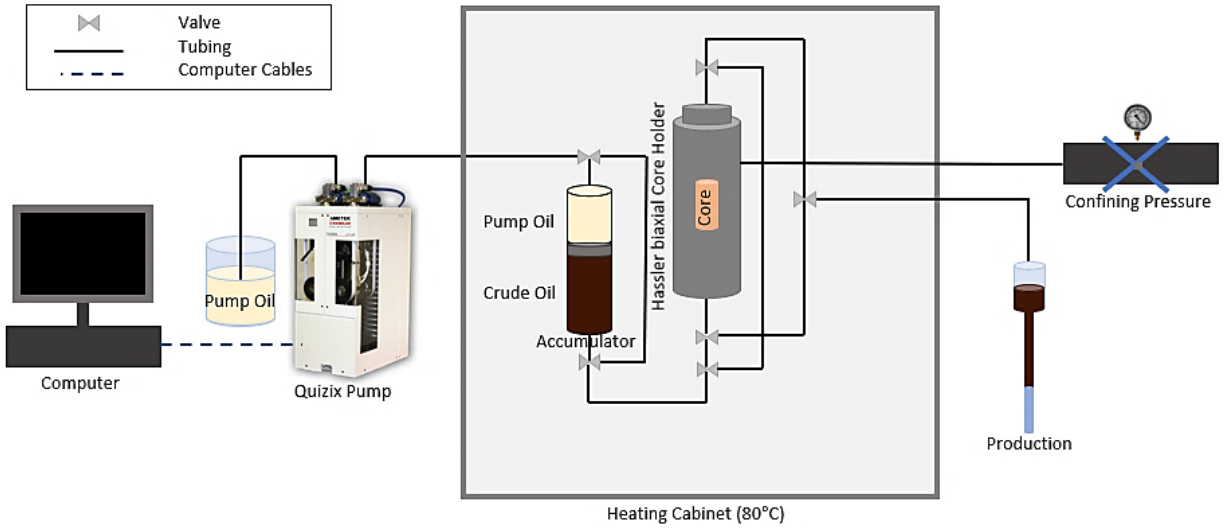

Figure A.2 – Experimental setup used for wettability alternation.

A.4 Wettability measurements by Amott-Harvey relative displacement Index

To determine the wettability preference of the aged core samples, the quantitative *Amott-Harvey method* was used. The Amott-Harvey method is a modification of the Amott wettability test where imbibition and displacement are combined to measure average wettability. The method is based on the fact that the wetting fluid will generally imbibe spontaneously into the core, displacing the nonwetting one. To demonstrate that the wetting preference of a core sample is water wet when oil is the coating fluid, one can allow water to imbibe into the core. The water will displace the oil from the surface and one can say

that the core sample prefers to be in contact with water (William G. Anderson, 1986). In an oil wet core sample saturated with brine, oil will imbibe and displace the water in the core sample.

The wettability was determined by following the four steps of the Amott-Harvey method (figure A.3):

1. Spontaneous imbibition: The core sample at S_{wi} was placed in an imbibition cell and submerged into brine for 168 hours (figure A.4). The production of n-decane by spontaneous capillary imbibition was measured ($V_{o,sp}$).
2. Forced imbibition: The core sample was mounted in the same setup as shown in figure 3.2 (section 3.3.2), and the n-decane in the core sample was displaced with brine (at least 2.5 PV injected each way). The production of n-decane by forced imbibition was measured ($V_{o,forced}$).
3. Spontaneous displacement: The core sample is once again placed in an imbibition cell, but this time submerged into n-decane for 168 hours (see figure A.4). The production of brine by spontaneous capillary displacement was measured ($V_{w,sp}$).
4. Forced displacement: The core sample is mounted in the same setup as shown in figure 3.2 (section 3.3.2), once again, and the brine inside the core sample was displaced by n-decane (at least 2.5 PV injected each way). The production of brine by forced displacement was measured ($V_{w,forced}$).

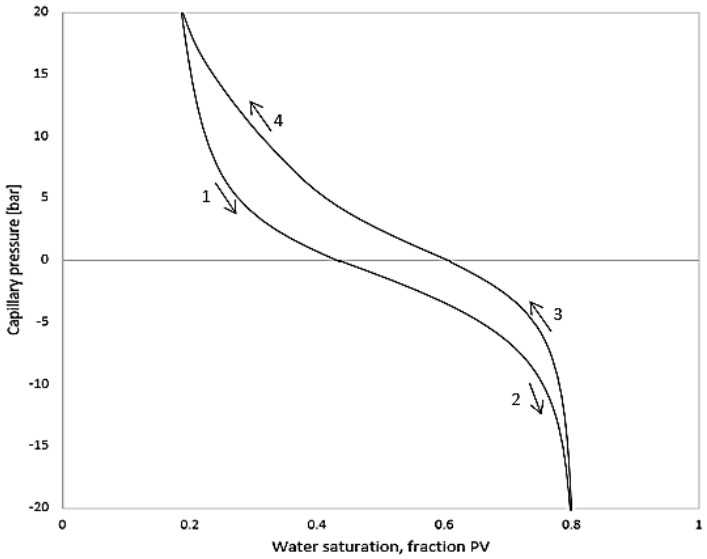

Figure A.3 – The four steps from the Amott-Harvey method. (1) Spontaneous imbibition, (2) Forced imbibition, (3) Spontaneous displacement and (4) Forced displacement.

The Amott-Harvey wettability index (I_{AH}) is calculated by the following equation (William G. Anderson, 1986):

$$I_{AH} = I_w - I_o = \frac{V_{o,sp}}{V_{o,tot}} - \frac{V_{w,sp}}{V_{w,tot}} = \frac{V_{o,sp}}{V_{o,sp}+V_{o,forced}} - \frac{V_{w,sp}}{V_{w,sp}+V_{w,forced}} \quad \text{(A.1)}$$

Where I_w is the wettability index of water and I_o is the wettability index of oil. The Amott-Harvey index varies from -1 to 1. I_{AH} = 1 for strongly water wet, and I_{AH} = -1 for strongly oil wet. For values in between, see table A.1:

Table A.1 – Relation between Amott-Harvey wettability Index and wettability.

	AMOTT-HARVEY INDEX, I_{AH}
WATER WET	$0{,}3 \leq \mathrm{I_{AH}} \leq 1$
NEUTRAL WET	$-0{,}3 \leq \mathrm{I_{AH}} \leq 0{,}3$
OIL WET	$-1 \leq \mathrm{I_{AH}} \leq -0{,}3$

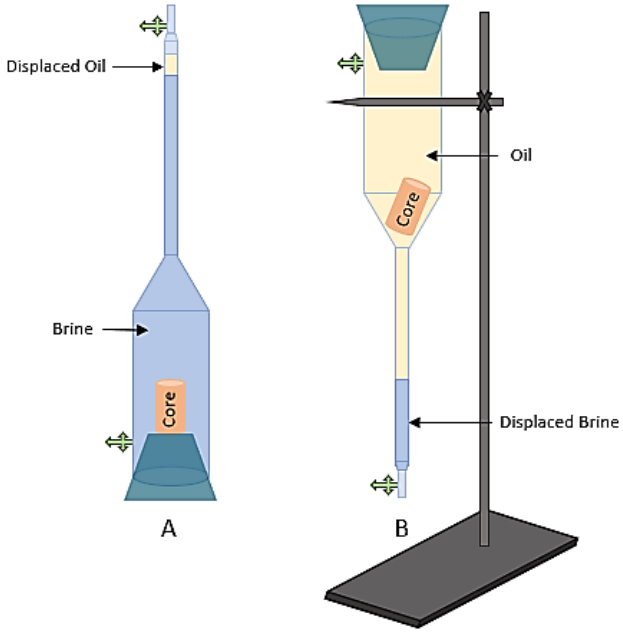

Figure A.4 – Experimental setup for A) Spontaneous imbibition of oil with brine, and B) Spontaneous displacement of water with oil.

A.5 Wettability alteration results and analysis

This section present results from 4 aged limestone core samples (L7, L8, L9 and L10), where brine constituted the aqueous phase and mineral oil (n-Decane) constituted the oleic phase. The core samples were used to investigate the wetting alteration produced by the given oil/rock/brine system by the dynamic aging method as described above. The dynamic aging method was found by Sandnes (2020) to give a more uniformly distributed wetting preference than static aging. The core samples where aged for the purpose to investigate dissolution of calcite with another wetting preference to see if it deviates from dissolution in strongly water-wet core samples. The core samples where not used in dissolution experiments in this work, because understanding a simpler system as a water-wet system was prioritized. The aged core samples are preserved and can be used for future work.

Table A.2 – Measured Amott-Harvey wettability index for core sample L7, L8, L9, and L10.

CORE ID	I_{AH} ±0.003
L7	-0.055
L8	-0.036
L9	-0.45
L10	-0.026

L = EDWARDS LIMESTONE

After performing dynamic aging method for the four core samples, full Amott-Harvey cycles were performed to measure the wettability index (I_{AH}): spontaneous imbibition, forced imbibition, spontaneous displacement, and forced displacement. Based on the production from the cycle, the wettability index was calculated and can be found in table A.2. The four core samples chosen for wettability alteration has porosity and permeability that was approximately equal to obtain a simpler comparison of the indexes. The Amott-Harvey wettability index for L7, L8, L9 and L10 was -0.055, -0.036, -0.45 and -0.026 respectively. These indices indicates that the oil spontaneously displaces some of the water in the core samples. No spontaneously water imbibition was recorded. For L9, 3.8ml of water was produced during spontaneous displacement, leaving a strong indication that the core samples were of an oil wet character. Whereas for L7, L8 and L10 under 1ml of water was produced during spontaneous displacement, leaving an indication that the core samples were closer to a neutrally wet character, although produced water by spontaneous displacement suggest tendencies towards weakly oil-wet conditions. The measured indices correspond to neutral-wet conditions for core sample L7, L8 and L10, while for L9 the index indicates oil-wet conditions. Figure A.5 displays increase in oil saturation as a function of time during one cycle of spontaneous displacement, where water was displaced by the oil in L7, L8, L9 and L10. The Amott-Harvey cycle for L9 and L10 was performed in the beginning of March 2020, leaving the spontaneous displacement to last for 1129hours due to Covid-19 lockdown.

The four core samples aged dynamically by crude oil, where one Amott-Harvey cycle was performed confirmed that the wettability had been altered to slightly oil wet. Water was spontaneously displaced by oil, while no spontaneous water imbibition found place. The wettability alteration of four Edwards yellow limestone core samples obtained nearly neutral or slightly oil-wet wettability preference.

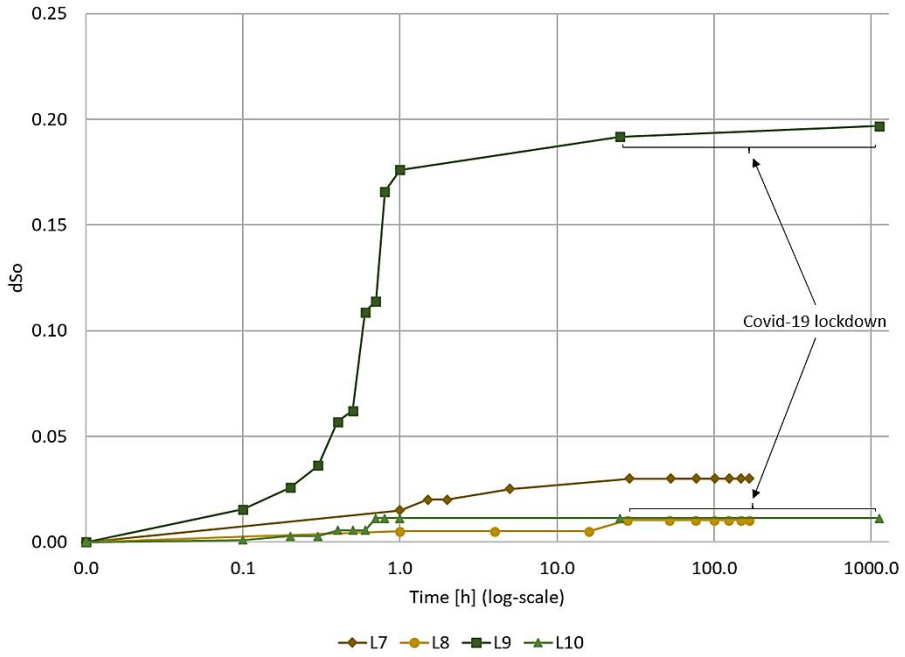

Figure A.5 – Increase in oil saturation (dS_O) as a function of time during one cycle of spontaneous displacement where oil displaces water in L7, L8, L9 and L10.

B Filtration of produced effluents after dissolution and XRD-analysis of filtered particles

The effluents produced during dissolution were filtered to separate the assumed calcite particles produced from the brine from experiment L2 and L3. The filtered particles were analyzed with an XRD-analysis to determine what mineral that was produced. The XRD-analysis was performed by an engineer at Department of Geoscience, UoB. The filtration procedure is exhibited in figure B.1. A 0.45µm Supor filter was placed between a top and bottom glass container. The attachment of the containers was sealed by a clamp. The effluents were filled in the top container and just half of the container was filled; therefore, the filtration was needed to be performed several times and the filter was changed during each time. In addition, a vacuum tubing was attached to the bottom container and in the other end attached to a sink. Turning the sink on and letting the water pour, created a vacuum and the effluents from the top container were produced through the filter and down to the bottom container. The produced fluid in the bottom container was observed to be substantial clearer than the effluent fluid which had a white milky color. The color indicates that the effluent contains assumed calcite particles in different sizes. After filtration, the filter was dried, and the calcite particles was collected in a petri dish.

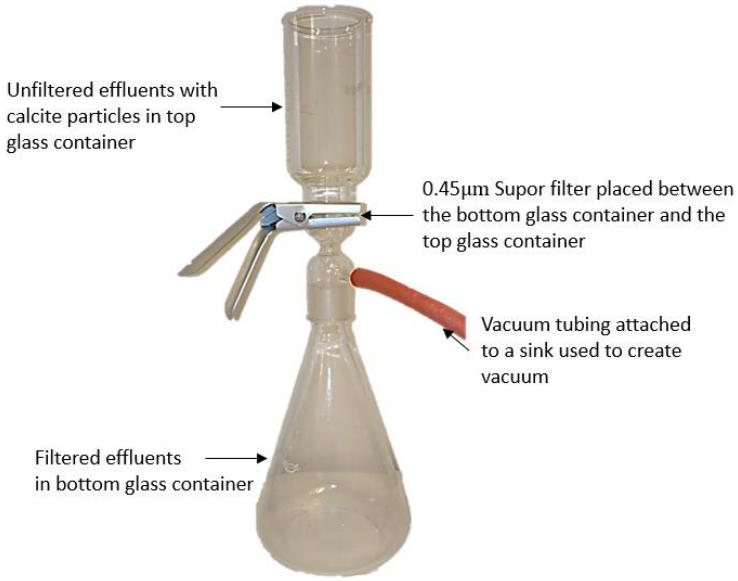

Figure B.1 – Filtration setup.

An attempt on measuring the amount of particles was the initial idea, but calcite precipitation in tubing's, inline pH-electrode container, and bottle/cylinders leaves a considerable uncertainty. Therefore, the measured values were not considered. However, the dried calcite particles from the filtration (see figure B.2 for a selection of filters with calcite minerals) was chemically evaluated by XRD-analysis (X-ray diffraction analysis).

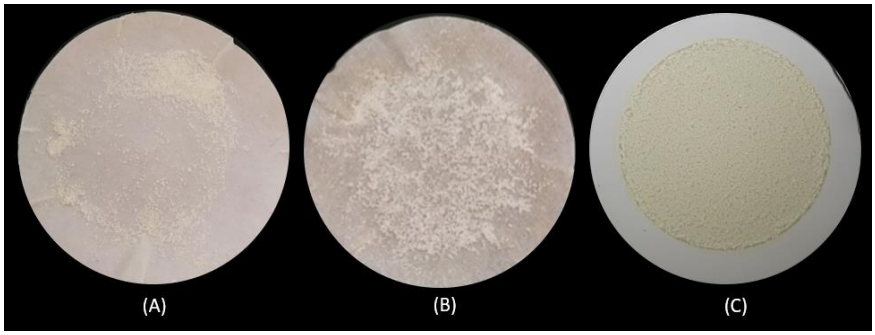

Figure B.2 – Filtered calcite from produced effluents during dissolution experiments. (A) Calcite from produced effluents in experiment L1 during Q=40ml/h (wet filter), (B) calcite from produced effluents in experiment L1 during Q=80ml/h (wet filter), and (C) calcite from a small volume of effluents produced from experiment L2 (dry filter).

An X-ray diffraction is an analytical method for deciding the crystallographic structure of a material, in addition, different crystal structures and phase transition can be determined. The main principle of the method is that an X-ray beam shot was sent towards the dried particles, and the structure of the particles decides how the X-ray is reflected. Known as Braggs equation:

$$n\lambda = 2d \sin\theta \tag{B.1}$$

A detector collects the reflected X-rays and shows how much reflection the different planes of the lattice structure of the particles give, and the angle (θ) is measured and the lattice distance (d) is calculated with known wavelength (λ). An XRD-diagram as shown in figure B.3 (for L2), and B.4 (for L3) exhibits the reflection angle (2θ) and its intensity (I) (counts). One and each mineral has its own decided structure and lattice distance, and the relative intensity of the reflection will always be the same. The identification of a mineral can be compared to fingerprints. An XRD-analysis is therefore used to identify minerals in samples, and as for fingerprints, a preexisting database that contains minerals with known lattice distance and relative intensity to match the minerals in the sample. Dried particles were placed on a glass plate before it was placed in a D8 ADVANCE ECO x-ray diffraction scanner at Department of Geoscience, UoB. The diffraction pattern was canned from 3-90°2θ, which is the x-axis in the diffraction diagram. In figure B.3, for particles from L2, and B.4 for particles from L3, showed good match of calcite ($CaCO_3$) when the analysis was compared to the database. Calcite has a peculiar fingerprint/characteristic with a large peak around 29.6°2θ, followed by three small peaks at 90°, 39.5°, and 43°2θ.

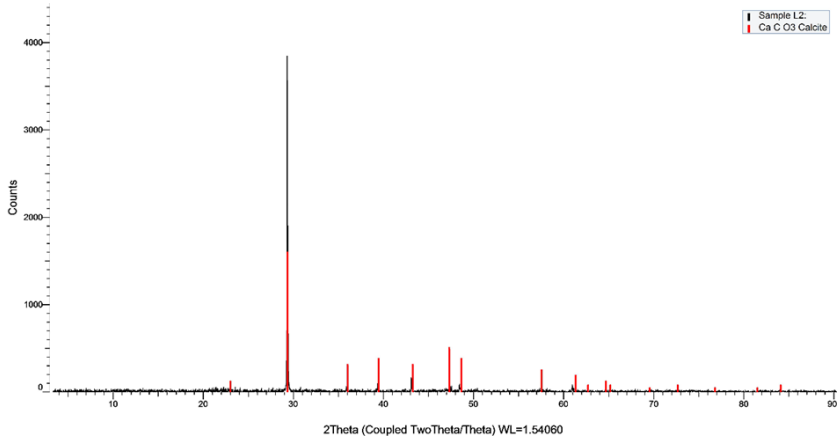

Figure B.3 – XRD-analysis of filtered particles from effluents produced during dissolution in core sample L2.

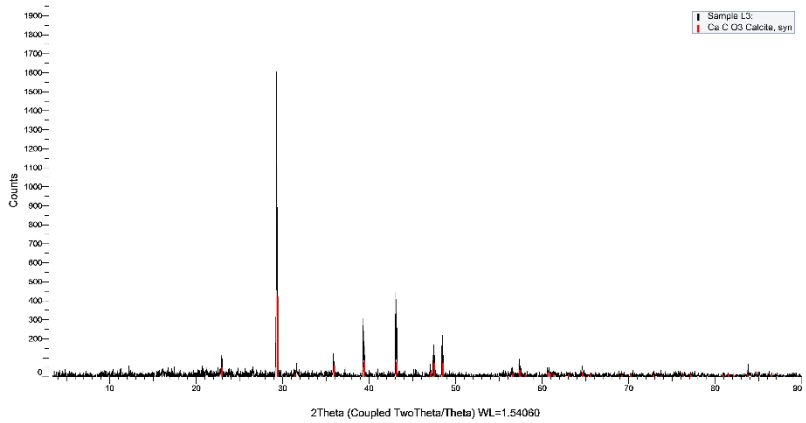

Figure B.4 – XRD-analysis of filtered particles from effluents produced during dissolution in core sample L3.

Figure B.5 shows both core samples (L2 and L3) plot in the same diffraction diagram with the reference fingerprint, shown as green columns. In addition, produced particles from a similar experiment (L4) performed by another master student at the reservoir physics group at UoB. Figure B.6 shows all three samples plotted above each other, towards a standard diffraction pattern for calcite (bottom), for demonstrating the fingerprint of calcite. The most important characteristics for calcite are marked as grey areas – which clearly shows that the samples contained 100% calcite.

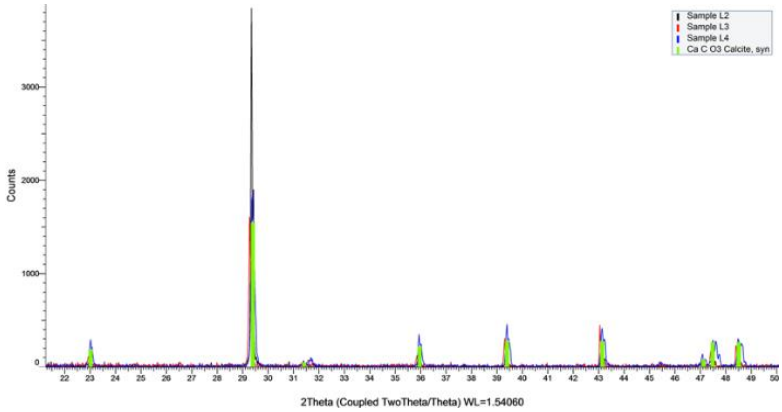

Figure B.5 – Compared diffraction diagram of three samples containing filtered particles from effluents produced during dissolution. In addition, the fingerprint of calcite (green).

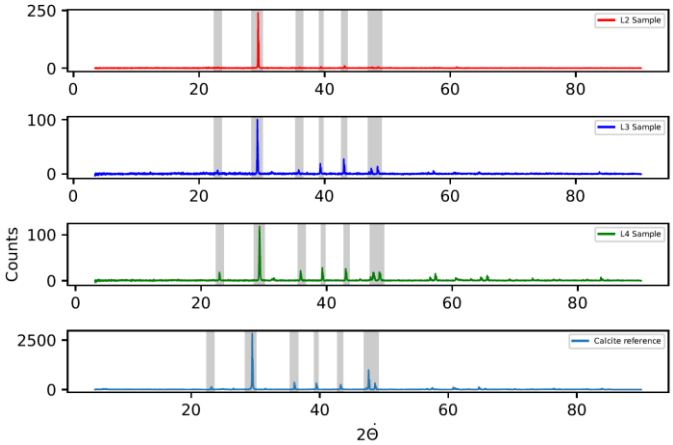

Figure B.6 – Diffraction diagram of all three core samples, respectively. In addition, a calcite reference/fingerprint (bottom and grey areas).

C Micro-CT images of homogenous Rørdal chalk core samples

Figure C.1 shows an axial cross section from three Rørdal chalk core samples obtained by micro-CT images. In C13 areas with high CT-number (white area) was observed and may indicate impurities like quartz. Quartz has a lower density (2.65g/ml) than calcite (2.71g/ml), but quartz has greater hardness (7) and acts like a unit because it hardly has any porosity. Calcite contains more porosity and causes therefore less attenuation of X-rays than quartz and have therefore a smaller CT-number. C15 has a vertically stripe with higher porosity that is present through almost the whole core sample. This stripe can cause a local geomechanically weakening and may trigger a fracture if the core sample is put to sufficient stress. In C14 a fossil is shown in the CT-image. Fossils like coccoliths are common in chalk outcrops deposited in Cretaceous. Visually, one can see that chalk core samples are of a highly homogenous character with pores typically smaller than the voxel size (29.2µm). Therefore, it is challenging to quantify the pore size distribution by image analysis.

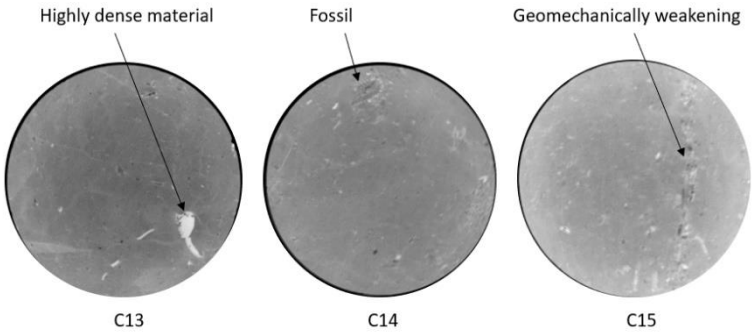

Figure C.1 – Cross sections from micro-CT images for core sample C13, C14 and C15 confirms highly homogenous core samples. Note that the core sample diameter is ~38mm in all three core samples.

D Setup for dissolution experiment by co-injection of CO_2 during high pressure PET-scan

A setup shown in figure D.1 was initially planned to be used for dissolution experiments during PET-scanning at in-situ conditions. Where co-injection of brine and CO_2 injection at room temperature and 90bars was planned to be performed whilst dynamical PET-images were conducted. The purpose was to visualize and quantify dissolution patterns as a function of time (PV injected) with data from PET-images. Due to the Covid-19 situation the availability of the small animal PET/CT lab at Haukeland University Hospital was limited, and therefore the planned experiment was not performed. But the setup was mounted correctly, pressure tested and tested for leakages. The pressure test was successful, and the setup is therefore ready for possibly future work. The procedure would be approximate the same as the procedure described in section 3.4.

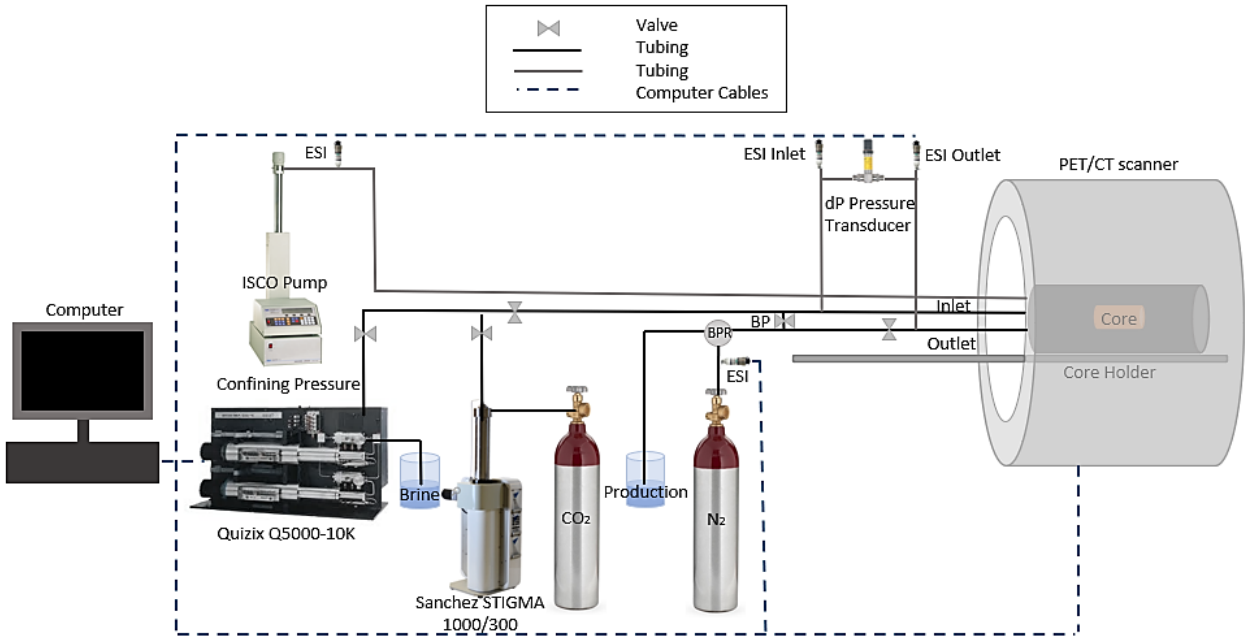

Figure D.1 – Experimental setup used for high pressure PET/CT-imaging by injection co-injection of CO_2 and F^{18}-brine.

E Plots from streamtube analysis

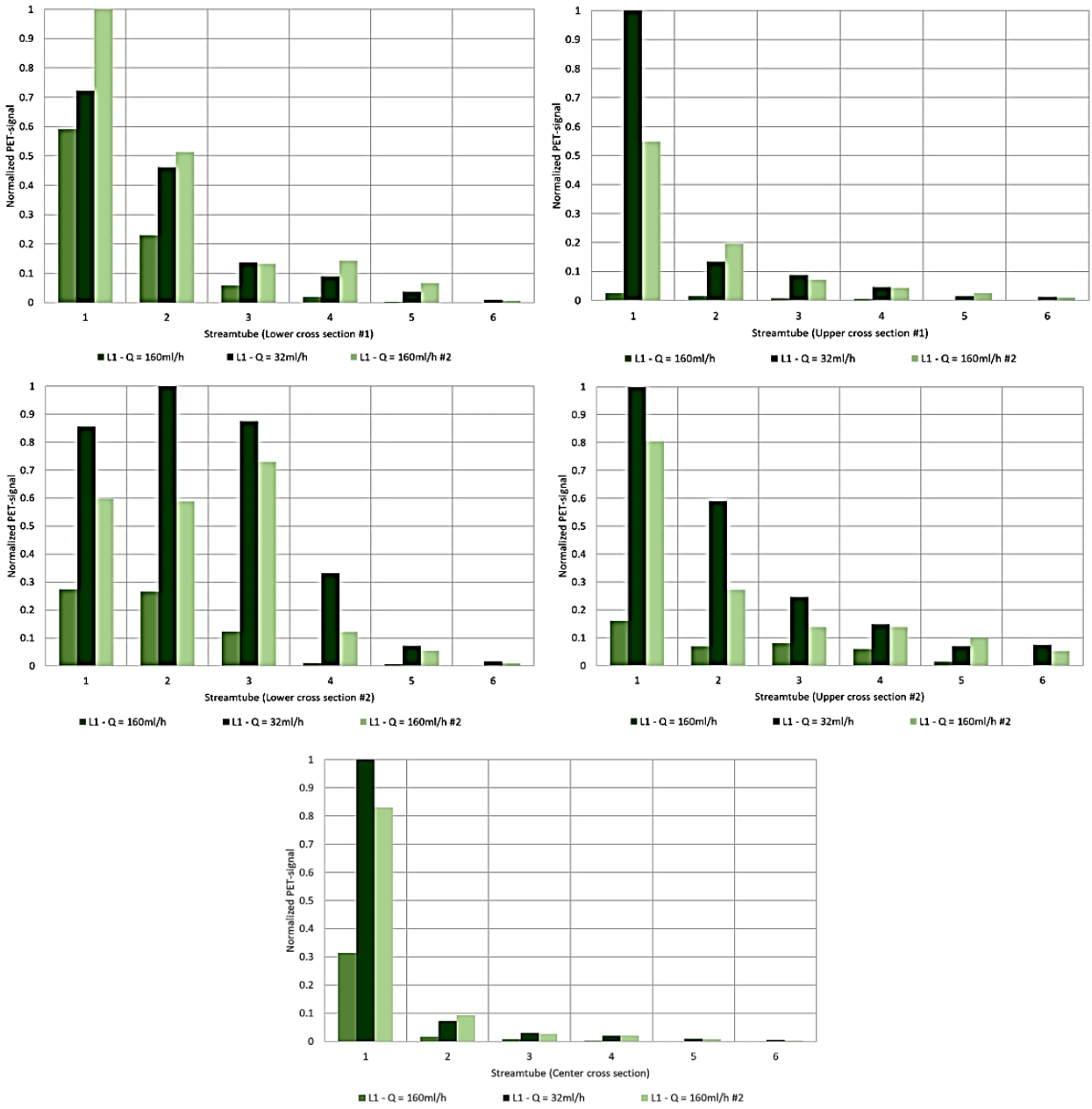

Figure E.1 – Streamtube analysis for each cross section in L1.

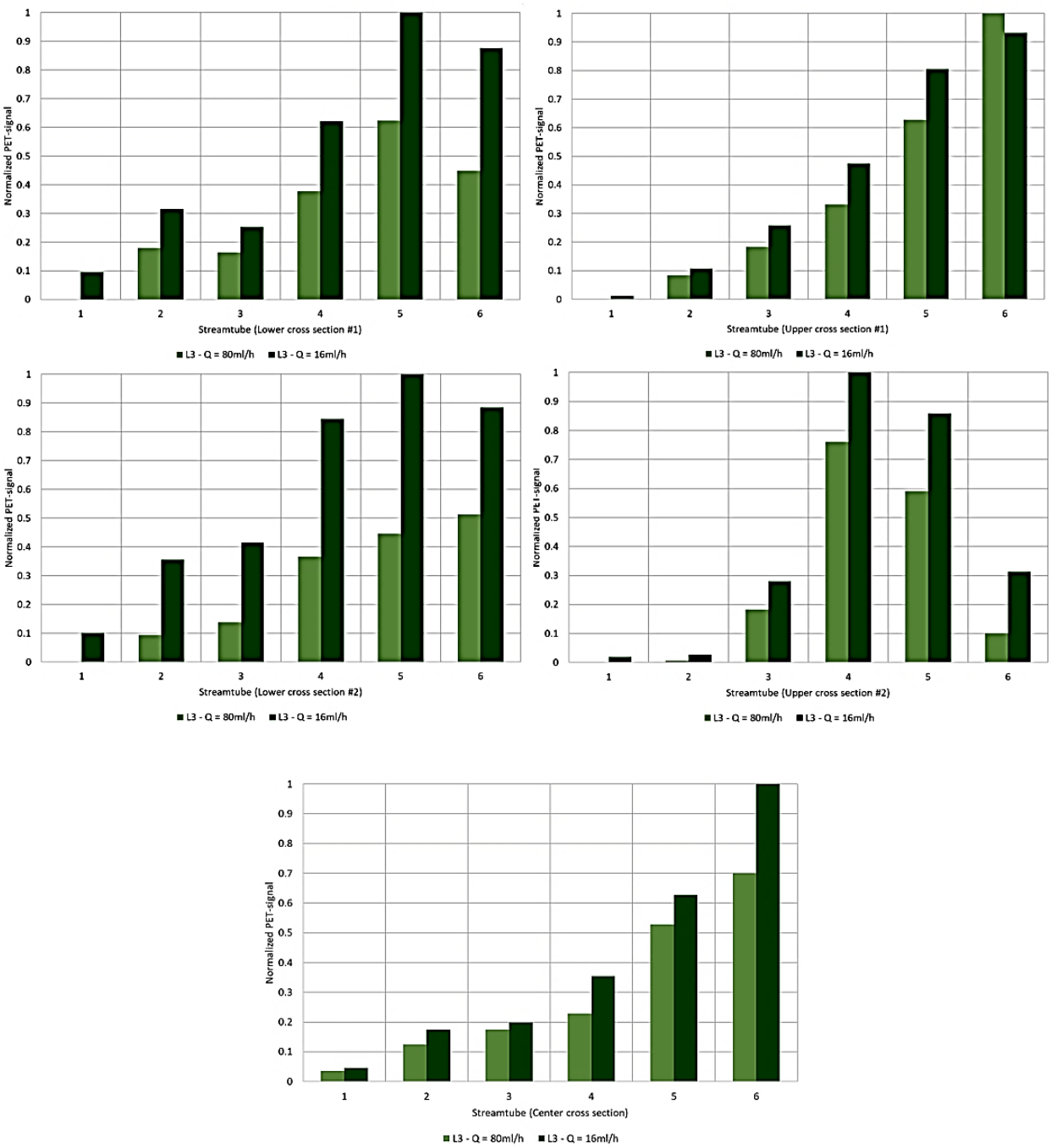

Figure E.2 – Streamtube analysis for each cross section in L3.

F Differential pressure of injection by FDG-brine during PET-scan

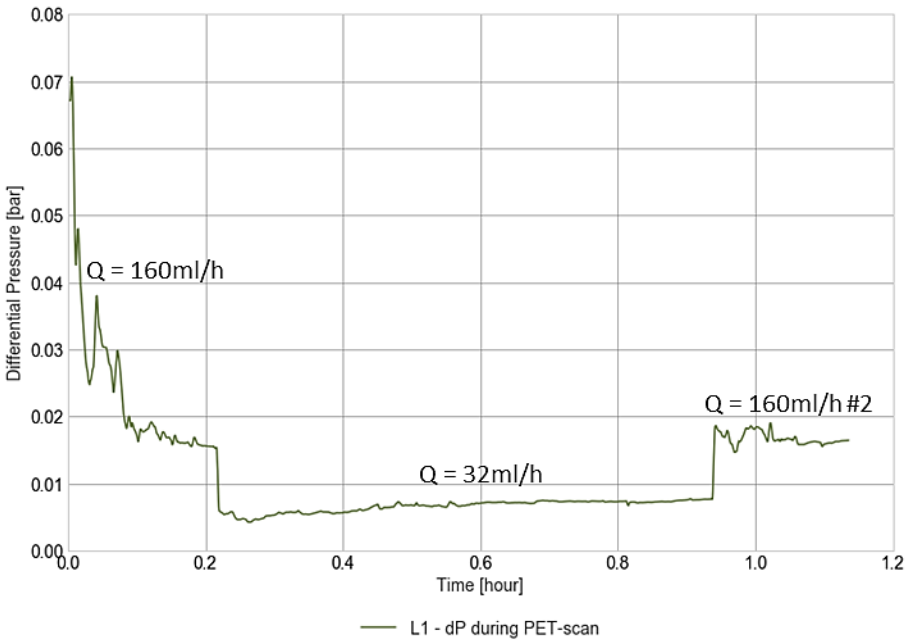

Figure F.1 – Differential pressure during PET-scanning for L1, where traceable brine was injected. A differential pressure transducer was used.

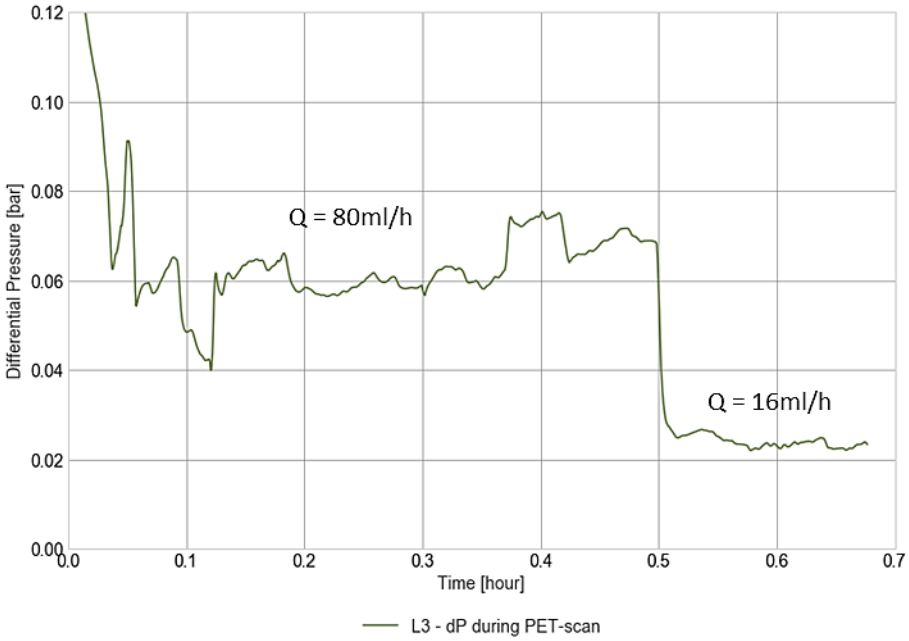

Figure F.2 – Differential pressure during PET-scan for L3, where traceable brine was injected. Note that the pressure was measured by a ESI pressure transducer with a higher uncertainty for L3.

G Uncertainties

The uncertainty in experimental calculations and measurements is affected by primarily two sources: The quantitative source, which implies uncertainties in equipment that was used while performing an experiment (e.g., uncertainties in scale, pump flow rate etc.), and the qualitative source which implies uncertainties in the performance of an experiment (e.g., the method used for measuring the porosity).

The total uncertainty of a measured value depends on the instrumental uncertainties, which can be found in table G.1. The calculated uncertainties in this thesis are based on the following equations from Erdal (1997):

The results of a measurement should be reported by a mean value and a measure of the uncertainty. The mean value ($\bar{k}$) of a set of data points $k_1, k_2, k_3, \dots, k_N$ was calculated as:

$$\bar{k} = \frac{1}{N}\sum_{i=1}^{N} k_i \tag{G.1}$$

The uncertainty of a mean value can be estimated from *standard deviation* which quantifies the amount of variation between individual variable of a data set. The estimate, S, for standard deviation was calculated as:

$$S = \sqrt{\frac{1}{N-1}\sum_{i=1}^{N}\left(k_i - \bar{k}\right)^2} \tag{G.2}$$

where N is the number of measurements k.

If a value R is calculated by using addition and/or subtraction, the uncertainty can be calculated by the *addition and subtraction method.* Several independent variables $x, y, z, \dots, i,$ are added or subtracted to calculate a value R, where the uncertainty in R (S_R), was calculated based on the estimated standard deviation of each variable ($S_x, S_y, S_z, \dots, S_i$):

$$S_R = \sqrt{(S_x)^2 + \left(S_y\right)^2 + (S_z)^2 + \cdots + (S_i)^2} \tag{G.3}$$

If the value R was calculated as the product or quotient of a set of variables $x, y, z, \dots, i$, (e.g., permeability measurements) the uncertainty of R can be found by using the *multiplication and division method*. $x, y, z, \dots, i$ are variables with an estimated standard deviation $S_x, S_y, S_z, \dots, S_i$, and the uncertainty S_R was calculated as:

$$S_R = R\sqrt{\left(\frac{S_x}{x}\right)^2 + \left(\frac{S_y}{y}\right)^2 + \left(\frac{S_z}{z}\right)^2 + \cdots + \left(\frac{S_i}{i}\right)^2} \tag{G.4}$$

Table G.1 – Instrumental uncertainties for apparatus used during experimental procedures.

INSTRUMENT	PARAMETER	UNCERTAINTY (±)	UNIT
SCALE	Mass	0.01	g
CALIPER	Length	0.01	cm
IMBIBITION CELL	Volume	0.05	ml
ESI PRESSURE TRANSDUCER	Pressure	0.10% of full scale	bar
APLIENS DIFFERENTIAL PRESSURE TRANSDUCER	Pressure	0.075% of full scale	bar
QX 5000 PUMP	Rate	0.2% of rate	ml/h
QX 6000 PUMP	Rate	0.2% of rate	ml/h
QX PUMP	Rate	0.1% of rate	ml/h
ISCO PUMP	Rate	0.5% of setpoint	ml/h
	Pressure	0.5% of full scale	bar
ATI Q45P PH – GAUGE	pH	0.01 and 0.007 stability over 24 hours	pH

References

Abdallah, W., Buckley, J. S., Carnegie, A., Edwards, J., Herold, B., Fordham, E., . . . Signer, C. (1986). Fundamentals of wettability. *Technology, 38*(1125-1144), 268.

Agada, S., Geiger, S., & Doster, F. (2016). Wettability, hysteresis and fracture--matrix interaction during CO.sub.2 EOR and storage in fractured carbonate reservoirs. *International Journal of Greenhouse Gas Control, 46*, 57. doi:10.1016/j.ijggc.2015.12.035

Al-Khulaifi, Y., Lin, Q., Blunt, M. J., & Bijeljic, B. (2017). Reaction Rates in Chemically Heterogeneous Rock: Coupled Impact of Structure and Flow Properties Studied by X-ray Microtomography. *Environ. Sci. Technol, 51*(7), 4108-4116. doi:10.1021/acs.est.6b06224

Anderson, W. G. (1986). Wettability Literature Survey- Part 1: Rock/Oil/Brine Interactions and the Effects of Core Handling on Wettability. *Journal of Petroleum Technology, 38*(10), 1125-1144. doi:10.2118/13932-PA

Anderson, W. G. (1987). Wettability Literature Survey-Part 6: The Effects of Wettability on Waterflooding. *Journal of Petroleum Technology, 39*(12), 1605-1622. doi:10.2118/16471-PA

Anderson, W. I. (1998). *Iowa'S Geological Past : Three Billion Years Of Change*. Iowa City, UNITED STATES: University of Iowa Press.

Bachu, S. (2008). CO 2 storage in geological media: Role, means, status and barriers to deployment. *Progress in Energy and Combustion Science, 34*(2), 254-273. doi:10.1016/j.pecs.2007.10.001

Bachu, S., Bonijoly, D., Bradshaw, J., Burruss, R., Holloway, S., Christensen, N. P., & Mathiassen, O. M. (2007). CO 2 storage capacity estimation: Methodology and gaps. *International Journal of Greenhouse Gas Control, 1*(4), 430-443. doi:10.1016/S1750-5836(07)00086-2

Bachu, S., Gunter, W., & Perkins, E. (1994). AQUIFER DISPOSAL OF CO2 - HYDRODYNAMIC AND MINERAL TRAPPING. *Energy Conv. Manag., 35*(4), 269-279.

Baines, S. J., & Worden, R. H. (2004). Geological storage of carbon dioxide. *Geological Society, London, Special Publications, 233*(1), 1-6. doi:10.1144/GSL.SP.2004.233.01.01

Bear, J. (1988). *Dynamics of fluids in porous media*. New York: Dover.

Benson S., C. P., Anderson H., Bachu S., Nimir B.H.,Basu B., ... Whittaker S. (2013). *IPCC Special Report; Carbon Dioxide Capture and Storage. Chapter 5: Underground geological storage*. Retrieved from https://www.ipcc.ch/

Benson, S. M., & Cole, D. R. (2008). CO2 Sequestration in Deep Sedimentary Formations. *Elements, 4*(5), 325-331. doi:10.2113/gselements.4.5.325

Brattekås, B., Eide, Ø., Johansen Sigbjørn, A., Vasshus Snorre, S., Polden Andreas, G., & Fernø Martin, A. (2020). Foam Flow and Mobility Control in Natural Fracture Networks. *Transport in Porous Media, 131*(1), 157-174. doi:10.1007/s11242-019-01249-3

Brattekås, B., Gauteplass, J., Brekke, N., Fernø, M. A., & Ersland, G. (2020). Unlocking multimodal PET-MR synergies for geoscience. *Advances in Water Resources, 142*, 103641. doi:10.1016/j.advwatres.2020.103641

Brattekås, B., Steinsbø, M., Graue, A., Fernø, M. A., Espedal, H., & Seright, R. S. (2017). New Insight Into Wormhole Formation in Polymer Gel During Water Chase Floods With Positron Emission Tomography. *22*(1), 032-040. doi:10.2118/180051-PA

Burchette, T. P. (2012). Carbonate rocks and petroleum reservoirs, a geological perspective from the industry. *Geological Society Special Publications, 370*(1), 17-37. doi:10.1144/SP370.14

Chaojie, C., Sina, H., Harald, M., & Philipp, B. (2020). Measuring hydraulic fracture apertures: a comparison of methods. *Solid earth (Göttingen), 11*(6), 2411-2423. doi:10.5194/se-11-2411-2020

Cherry, S., & Chatziioannou, A. (2004). Small Animal PET Systems. In (pp. 213-228).

CO2CRC. (2020). Figure: Overview of Geological Storage Options. Retrieved from http://www.co2crc.com.au/co2crc-appoints-distinguished-scientists/

Cote, H., & Thimus, J. F. (1999). *Ultrasonic Velocity And Attenuation During Brazilian Test*. Paper presented at the 9th ISRM Congress, Paris, France. https://doi.org/

Craig, F. F. (1971). *The reservoir engineering aspects of waterflooding* (Vol. vol. 3). New York: Henry L. Doherty Memorial Fund of AIME.

Czernichowski-Lauriol, I., Rochelle, C., Gaus, I., Azaroual, M., Pearce, J., & Durst, P. (2006). *Geochemical interactions between co2, pore-waters and reservoir rocks* (Vol. 65). Dordrecht: Dordrecht: Springer Netherlands.

Dodds, W. S., Stutzman, L. F., & Sollami, B. J. (1956). Carbon Dioxide Solubility in Water. *Industrial & Engineering Chemistry Chemical & Engineering Data Series, 1*(1), 92-95. doi:10.1021/i460001a018

Erdal, A. (1997). *Elementær innføring i sannsynlighetsregning og problemløsninger ved analyse av måleresultater* ([Rev. utg.]. ed.). Bergen: Alma mater.

Ferno, M. A., Torsvik, M., Haugland, S., & Graue, A. (2010). Dynamic Laboratory Wettability Alteration. *Energy Fuels, 24*(7), 3950-3958. doi:10.1021/ef1001716

Fernø, M. A., Eide, Ø., Steinsbø, M., Langlo, S. A. W., Christophersen, A., Skibenes, A., . . . Graue, A. (2015). Mobility control during CO2 EOR in fractured carbonates using foam: Laboratory evaluation and numerical simulations. *Journal of Petroleum Science and Engineering, 135*, 442-451. doi:10.1016/j.petrol.2015.10.005

Fernø, M. A., Haugen, Å., Wickramathilaka, S., Howard, J., Graue, A., Mason, G., & Morrow, N. R. (2013). Magnetic resonance imaging of the development of fronts during spontaneous imbibition. *Journal of Petroleum Science and Engineering, 101*, 1-11. doi:10.1016/j.petrol.2012.11.012

Fernø, M. A., Torsvik, M., Haugland, S., & Graue, A. (2010). Dynamic Laboratory Wettability Alteration. *Energy Fuels, 24*(7), 3950-3958. doi:10.1021/ef1001716

Golfier, F., Zarcone, C., Bazin, B., Lenormand, R., Lasseux, D., & Quintard, M. (2002). On the ability of a Darcy-scale model to capture wormhole formation during the dissolution of a porous medium. *J. Fluid Mech, 457*, 213-254. doi:10.1017/S0022112002007735

Graue, A., Aspenes, E., Bogno, T., Moe, R. W., & Ramsdal, J. (2002). Alteration of wettability and wettability heterogeneity. *J. Pet. Sci. Eng., 33*(1-3), 3-17.

Graue, A., Viksund, B. G., Eilertsen, T., & Moe, R. (1999). Systematic wettability alteration by aging sandstone and carbonate rock in crude oil. *Journal of Petroleum Science and Engineering, 24*(2-4), 85-97. doi:10.1016/S0920-4105(99)00033-9

Haugen, Å., Fernø, M. A., Mason, G., & Morrow, N. R. (2015). The Effect of Viscosity on Relative Permeabilities Derived from Spontaneous Imbibition Tests. *Transport in Porous Media, 106*(2), 383-404. doi:10.1007/s11242-014-0406-4

Heindel, T. J. (2011). A Review of X-Ray Flow Visualization With Applications to Multiphase Flows. In: Digital Repository @ Iowa State University.

IEA. (2017). *Energy technology perspectives 2017 : catalysing energy technology transformations*. Retrieved from https://www.iea.org/

IPCC. (2015). *Climate Change 2014: Synthesis Report on Climate Cange 2014*. Retrieved from https://www.ipcc.ch/

Islam, A. W., & Carlson, E. S. (2012). Viscosity Models and Effects of Dissolved CO2. *Energy Fuels, 26*(8), 5330-5336. doi:10.1021/ef3006228

Jenkins, R. J. (1966). Accuracy Of Porosity Determinations. *The Log Analyst, 7*(02), 18. Retrieved from https://doi.org/

Jeong, H., & Srinivasan, S. (2017). Fast selection of geologic models honoring CO2 plume monitoring data using Hausdorff distance and scaled connectivity analysis. *International Journal of Greenhouse Gas Control, 59*, 40-57. doi:10.1016/j.ijggc.2017.02.005

Johannesen, E. B. (2008). *NMR characterization of wettability and how it impacts oil recovery in chalk.* University of Bergen, Department of Physics and Technology, Bergen.

Konzuk, J. S., & Kueper, B. H. (2004). Evaluation of cubic law based models describing single-phase flow through a rough-walled fracture: EVALUATION OF CUBIC LAW BASED MODELS. *Water Resources Research, 40*(2). doi:10.1029/2003WR002356

Kulenkampff, J., Gründig, M., Richter, M., & Enzmann, F. (2008). Evaluation of positron-emission-tomography for visualisation of migration processes in geomaterials. *Physics and chemistry of the earth. Parts A/B/C, 33*(14), 937-942. doi:10.1016/j.pce.2008.05.005

Kulenkampff, J., Gründig, M., Zakhnini, A., & Lippmann-Pipke, J. (2016). Geoscientific process monitoring with positron emission tomography (GeoPET). *Solid Earth Discussions*, 1-33. doi:10.5194/se-2016-35

Lemmon, E., McLinden, M., & Friend, D. (2012). Thermophysical Properties of Fluid Systems in NIST Chemistry WebBook, NIST Standard Reference Database Number 69, Eds. PJ Linstrom and WG Mallard, National Institute of Standards and Technology, Gaithersburg MD, 20899. In.

Lemmon, E., McLinden, M., & Friend, D. (2020). *"Thermophysical Properties of Fluid Systems" in NIST Chemistry WebBook, NIST Standard Reference Database Number 69, Eds. P.J. Linstrom and W.G. Mallard, National Institute of Standards and Technology, Gaithersburg MD, 20899*.

Luhmann, A. J., Kong, X.-Z., Tutolo, B. M., Garapati, N., Bagley, B. C., Saar, M. O., & Seyfried, W. E. (2014). Experimental dissolution of dolomite by CO2-charged brine at 100°C and 150bar: Evolution of porosity, permeability, and reactive surface area. *Chemical Geology, 380*, 145-160. doi:10.1016/j.chemgeo.2014.05.001

Luquot, L., & Gouze, P. (2009). Experimental determination of porosity and permeability changes induced by injection of CO 2 into carbonate rocks. *Chemical Geology, 265*(1-2), 148-159. doi:10.1016/j.chemgeo.2009.03.028

Mavko, G., & Nur, A. (1997). The effect of a percolation threshold in the Kozeny-Carman relation. *Geophysics, 62*(5), 1480-1482. doi:10.1190/1.1444251

Mees, F., Swennen, R., Geet, M. V., & Jacobs, P. (2003). Applications of X-ray computed tomography in the geosciences. *Geological Society, London, Special Publications, 215*(1), 1-6. doi:10.1144/GSL.SP.2003.215.01.01

Menke, H. P., Bijeljic, B., Andrew, M. G., & Blunt, M. J. (2015). Dynamic Three-Dimensional Pore-Scale Imaging of Reaction in a Carbonate at Reservoir Conditions. *Environ. Sci. Technol, 49*(7), 4407-4414. doi:10.1021/es505789f

Metz, B., Davidson, O. R., De Coninck, H., Loos, M., Meyer, L., Intergovernmental Panel on Climate Change. Working, G., III, . . . Canadian Electronic, L. (2013). *IPCC special report on carbon dioxide capture and storageCarbon dioxide capture and storage*.

Moore, C. H., & Wade, W. J. (2013). *The Nature and Classification of Carbonate Porosity* (Vol. 67): Elsevier Science & Technology.

Morrow, N. R., & Buckley, J. (2006). Wettability and Oil Recovery by Imbibition and Viscous Displacement from Fractured and Heterogeneous Carbonates: Final Report. In E. United States. Department Of (Ed.): University of Wyoming.

Noiriel, C., & Daval, D. (2017). Pore-Scale Geochemical Reactivity Associated with CO Storage: New Frontiers at the Fluid-Solid Interface. *Accounts of chemical research, 50*(4), 759. doi:10.1021/acs.accounts.7b00019

Onozaki, K. (2009). Population Is a Critical Factor for Global Carbon Dioxide Increase. *Journal of Health Science, 55*(1), 125-127. doi:10.1248/jhs.55.125

Ott, H., & Oedai, S. (2015). Wormhole formation and compact dissolution in single- and two-phase CO2-brine injections. *Geophysical research letters, 42*(7), 2270-2276. doi:10.1002/2015GL063582

Pape, H., Clauser, C., & Iffland, J. (1999). Permeability prediction based on fractal pore-space geometry. *Geophysics, 64*(5), 1447-1460. doi:10.1190/1.1444649

Perkins, T. K., & Johnston, O. C. (1963). A Review of Diffusion and Dispersion in Porous Media. *Society of Petroleum Engineers journal, 3*(1), 70-84. doi:10.2118/480-PA

Reeves, S. (2003). Enhanced CBM recovery, coalbed CO2 sequestration assessed. *Oil & Gas Journal, 101*(27), 49.

Ruidiaz, E., Winter, A., & Trevisan, O. (2017). Oil recovery and wettability alteration in carbonates due to carbonate water injection. *Journal of Petroleum Exploration and Production Technology, 8*. doi:10.1007/s13202-017-0345-z

Salathiel, R. A. (1973). Oil Recovery by Surface Film Drainage In Mixed-Wettability Rocks. *Journal of Petroleum Technology, 25*(10), 1216-1224. doi:10.2118/4104-PA

Sandnes, M. F. (2020). Wetting Stability of Aged Limestone in the presence of HPAM polymer. In: The University of Bergen.

Sjöberg, E. L., & Rickard, D. T. (1984). Temperature dependence of calcite dissolution kinetics between 1 and 62°C at pH 2.7 to 8.4 in aqueous solutions. *Geochimica et cosmochimica acta, 48*(3), 485-493. doi:10.1016/0016-7037(84)90276-X

Skjelsvik, E. B. (2018). Synergy of Nanoparticles and Surfactants for CO2 Foam Enhanced Oil Recovery and CO2 Storage in Carbonates. In: The University of Bergen.

Smith, M. M., Hao, Y., & Carroll, S. A. (2017). Development and calibration of a reactive transport model for carbonate reservoir porosity and permeability changes based on CO2 core-flood experiments. *International Journal of Greenhouse Gas Control, 57*(C). doi:10.1016/j.ijggc.2016.12.004

Smith, M. M., Sholokhova, Y., Hao, Y., & Carroll, S. A. (2013). CO2-induced dissolution of low permeability carbonates. Part I: Characterization and experiments. *Advances in Water Resources, 62*, 370-387. doi:10.1016/j.advwatres.2013.09.008

Snippe, J., Berg, S., Ganga, K., Brussee, N., & Gdanski, R. (2020). Experimental and numerical investigation of wormholing during CO2 storage and water alternating gas injection. *International Journal of Greenhouse Gas Control, 94*. doi:10.1016/j.ijggc.2019.102901

Snippe, J., Gdanski, R., & Ott, H. (2017). Multiphase Modelling of Wormhole Formation in Carbonates by the Injection of CO2. In (Vol. 114, pp. 2972-2984): Elsevier Ltd.

Snow, D. T. (1969). Anisotropie Permeability of Fractured Media. *Water Resources Research, 5*(6), 1273-1289. doi:10.1029/WR005i006p01273

Snæbjörnsdóttir, S. Ó., Sigfússon, B., Marieni, C., Goldberg, D., Gislason, S. R., & Oelkers, E. H. (2020). Carbon dioxide storage through mineral carbonation. *Nature Reviews Earth & Environment, 1*(2), 90-102. doi:10.1038/s43017-019-0011-8

Steel, L., Mackay, E., & Maroto-Valer, M. M. (2018). Experimental investigation of CO2-brine-calcite interactions under reservoir conditions. *Fuel Processing Technology, 169*, 122-131. doi:10.1016/j.fuproc.2017.09.028

Stefan Bachu, D. S., Kelly (Kailai) Thambimuthu, Paul Freund (2013). *IPCC Special Report; Carbon Dioxide Capture and Storage. Annex 1: Properties of CO2 and carbon-based fuels*. Retrieved from

Stumm, W., & Morgan, J. J. (1995). *Aquatic Chemistry: Chemical Equilibria and Rates in Natural Waters*. Somerset: Somerset: John Wiley & Sons, Incorporated.

Tipura, L. (2008). Wettability characterization by NMR T_2 measuments in Edwards Limestone. In. Bergen: L. Tipura.

Toublanc, A., Renaud, S., Sylte, J. E., Clausen, C. K., Eiben, T., & Nadland, G. (2005). Ekofisk Field fracture permeability evaluation and implementation in the flow model. *Petroleum Geoscience, 11*(4), 321-330. doi:10.1144/1354-079304-622

United Nations, U. (2015). PARIS AGREEMENT. Retrieved from http://unfccc.int/files/essential_background/convention/application/pdf/english_paris_agreement.pdf

Wang, H., Bernabé, Y., Mok, U., & Evans, B. (2016). Localized reactive flow in carbonate rocks: Core-flood experiments and network simulations. *Journal of geophysical research. Solid earth, 121*(11), 7965-7983. doi:10.1002/2016JB013304

Wilson, B., Mordensky, S., Verba, C., & Colwell, F. (2016). *An evaluation of subsurface microbial activity conditional to subsurface temperature, porosity, and permeability at North American carbon sequestration sites*.

Witherspoon, P. A., Wang, J. S. Y., Iwai, K., & Gale, J. E. (1980). Validity of Cubic Law for fluid flow in a deformable rock fracture. *Water Resources Research, 16*(6), 1016-1024. doi:10.1029/WR016i006p01016

Yang, Y., Li, Y., Yao, J., Iglauer, S., Luquot, L., Zhang, K., . . . Wang, Z. (2020). Dynamic Pore-Scale Dissolution by CO2-Saturated Brine in Carbonates: Impact of Homogeneous Versus Fractured Versus Vuggy Pore Structure. *Water Resources Research, 56*(4), n/a. doi:10.1029/2019WR026112

Zahasky, C., & Benson, S. M. (2018). Micro-positron emission tomography for measuring sub-core scale single and multiphase transport parameters in porous media. *Advances in Water Resources, 115*, 1-16. doi:10.1016/j.advwatres.2018.03.002